Characterization of Damage Mechanisms and Behavior in Two-Dimensionally Braided Composites Subjected to Static and Fatigue Loading
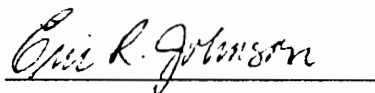
by

Scott T. Burr

Dissertation submitted to the Faculty of the Virginia Polytechnic Institute and State

University in partial fulfillment of the requirements for the degree of
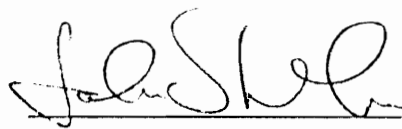
DOCTOR OF PHILOSOPHY

IN

ENGINEERING MECHANICS

APPROVED:

Don H. Morris

Don H. Morris, Chair

Eric R. Johnson

Eric R. Johnson

John J. Lesko

John J. Lesko

O. Hayden Griffin

O. Hayden Griffin

Saad A. Ragab

Saad A. Ragab

May 20, 1996

Blacksburg, Virginia

Keywords: Textile Composites, Testing, Failure, Fatigue, Damage, Modeling

C.2

Characterization of Damage Mechanisms and Behavior in Two-Dimensionally Braided Composites Subjected to Static and Fatigue Loading

by

Scott T. Burr

Dissertation submitted to the Faculty of the Virginia Polytechnic Institute and State

University in partial fulfillment of the requirements for the degree of

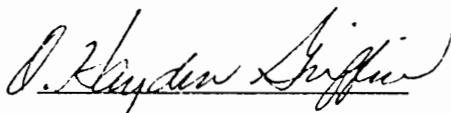DOCTOR OF PHILOSOPHY

IN

ENGINEERING MECHANICS
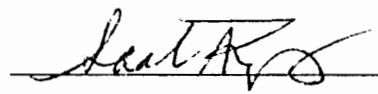
APPROVED:

_____

Don H. Morris, Chair

_____   _____

Eric R. Johnson   John J. Lesko

_____   _____

O. Hayden Griffin   Saad A. Ragab

May 20, 1996

Blacksburg, Virginia

Keywords: Textile Composites, Testing, Failure, Fatigue, Damage, Modeling

CHARACTERIZATION OF DAMAGE MECHANISMS AND BEHAVIOR IN TWO-DIMENSIONALLY BRAIDED COMPOSITES SUBJECTED TO STATIC AND FATIGUE LOADING

by

Scott T. Burr

Don H. Morris, Chairman

Department of Engineering Science and Mechanics

(Abstract)

In the present research project, four braided composite architectures consisting of graphite fibers in an epoxy matrix were tested under static and fatigue loading conditions to determine damage mechanism types and progressions. The braided architectures consisted of straight axial fiber bundles, which were surrounded by braider fiber bundles oriented at $\pm\alpha$ ° with respect to the axial fiber bundles. Static tension and compression testing was completed first to determine material strengths and basic damage modes for each of the architectures. Under static tension loading, cracking in the braider fiber bundles occurred first, and was followed by splitting in curved regions of the axial fiber bundles. Matrix cracking and kink band formation were found to occur under static compression loading.

A data acquisition system was developed which continuously monitored tangent modules and hysteresis energy information for fatigue specimens. Both notched and

unnotched specimens for each architecture were tested under tension-tension and compression-compression fatigue. Under tension-tension fatigue loading, cracking in the braider fiber bundles was found to occur first in all architectures, followed by disbonding of the axial fiber bundles from their surrounding constituents. This behavior dominated the responses of the architectures containing large axial fiber bundles. In one architecture, varying rates of dynamic stiffness as a function of cycle number were attributed to the stacking sequence of the individual layers in the braided architecture. Compression-compression fatigue response was dominated by the formation of kink bands in all architectures.

A shear-lag modeling approach which accounted for stiffness loss as a function of cycle number was developed and fit to tension-tension fatigue data for the architecture with the most consistent material response. Reasonable results were found, even though the model did not account for fiber bundle curvatures.

Acknowledgments

Table of Contents

List of Figures

List of Tables

1. Introduction

Textile composite materials are becoming more popular due to the ability of the manufacturers to braid net shape preforms. By braiding net shape preforms, the manufacturer can produce composite parts which are economically competitive with those made from traditional materials, while at the same time improving performance. This increased popularity brings about the need to accurately measure and predict the material response due to various loading conditions. The following work describes an experimental and analytical program which characterized damage mechanisms and behavior in two-dimensional triaxial-braided composites subjected to static and fatigue loading.

1.1 Material Systems

Four different two-dimensional triaxial-braided architectures were manufactured using an identical braiding process. This process is characterized by axial fiber bundles which run along straight lines as shown in Figure 1.1. The braid is termed triaxial due to its having straight fiber bundles oriented in the longitudinal direction, along with braiding
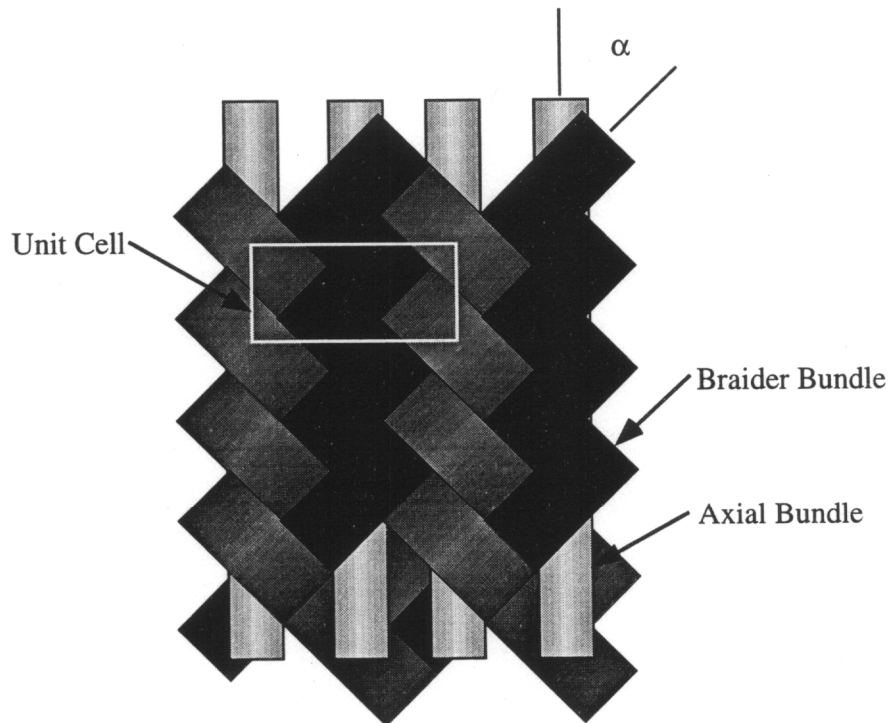
Figure 1.1 - Two-Dimensional Braid Schematic

Architecture	Axial Bundle Size	Braider Bundle Size
LSS	6K	15K
LLS	36K	15K
SLL	30K	6K
LLL	75K	15K
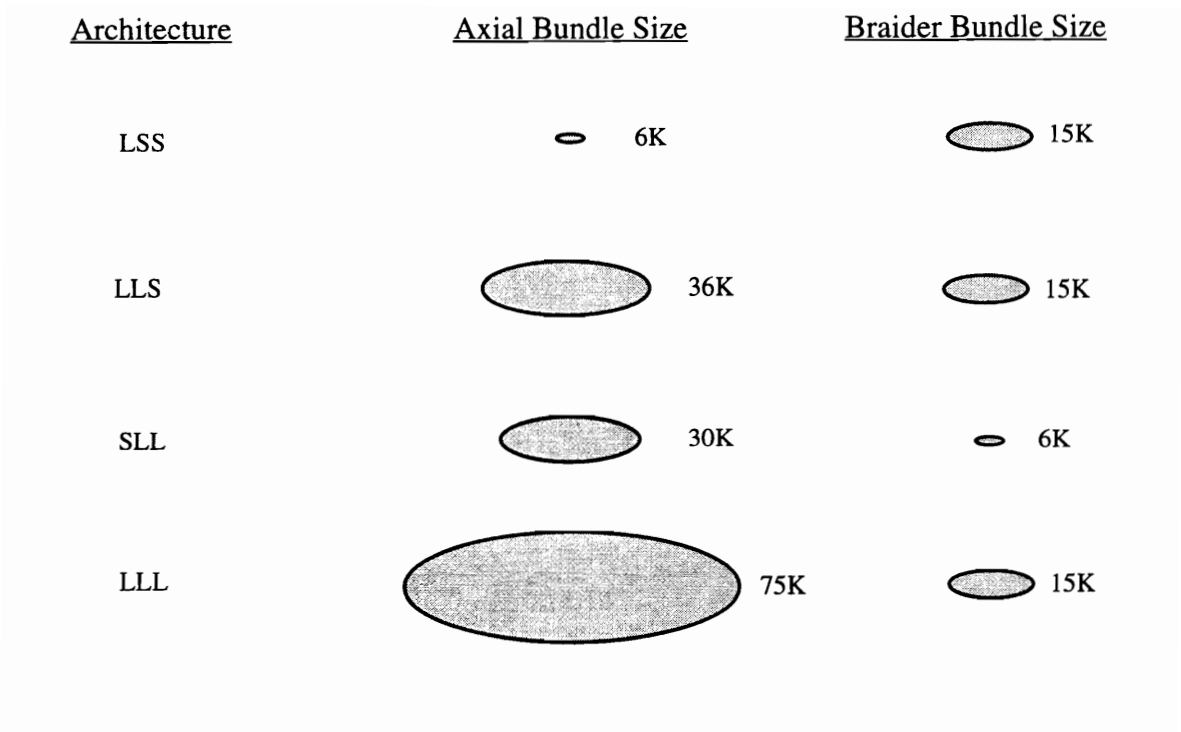
Figure 1.2 - Relative Bundle Sizes for Two-Dimensional Braids

fiber bundles oriented at $\pm\alpha$ degrees from the longitudinal axis. The braider fiber bundles

oriented at $+\alpha$ run over two and under two braider fiber bundles oriented at $-\alpha$. By varying

the fiber bundle size and braid angle, four different architectures were manufactured.

Table 1.1 lists the specifications of each of the architectures in this study, while Figure 1.2

shows the sizes of the bundles relative to each other. Two braid angles were used, which

were 45° and 70°. Braider fiber bundles ranged in size from six thousand fibers (6K) to

fifteen thousand fibers (15K), while axial fiber bundles ranged from 6K to 75K.

Percentage of total areal weight of the preform for axial fibers ranged from 12% to 46%.

Table 1.1 : Architecture Parameters

Architecture		Axial Fiber Bundle Size	Braider Fiber Bundle Size	No. of Layers of Braid / Thickness (in)	Braid Angle	Unit Cell Size (inches)
Shorthand	Longhand					
LSS	$[0_{6K}/\pm45_{15K}]_{12\%\ axial}$	6K	15K	5 / 0.105	45°	0.46 x 0.24
LLS	$[0_{36K}/\pm45_{15K}]_{46\%\ axial}$	36K	15K	3 / 0.108	45°	0.42 x 0.18
SLL	$[0_{30K}/\pm70_{6K}]_{46\%\ axial}$	30K	6K	4 / 0.109	70°	0.48 x 0.10
LLL	$[0_{75K}/\pm70_{15K}]_{46\%\ axial}$	75K	15K	3 / 0.115	70°	0.88 x 0.16

The architectures of the four material systems were chosen such that two comparisons could be made: 1) The effect of axial fiber bundle size could be evaluated by comparing the response of the LSS and LLS architectures, as the only difference was the LLS architecture had an axial fiber bundle size six times larger than that of the LSS architecture, and 2) The effect of scaling the architecture could be evaluated by comparing the SLL and the LLL architectures, as the SLL architecture was exactly 2.5 times smaller than the LLL architecture, with the same braid angle.

Two sets of notation were used to describe the individual material systems. The first is a shorthand notation consisting of three letters. The second is a commonly used longhand notation which completely describes the construction of the braid as shown in Figure 1.3. The first number inside the brackets designates the angle for the axial fiber bundles with respect to the longitudinal axis, which for the two-dimensional braids in this program is always zero. Its subscript designates the size of the axial fiber bundle in thousands of

$$[0_{6K}/\pm45_{15K}]_{12\%\text{ axial}}$$

Axial Bundle Orientation
Braider Bundle Orientation
Percent Axial Bundles
Braider Bundle Size
Axial Bundle Size
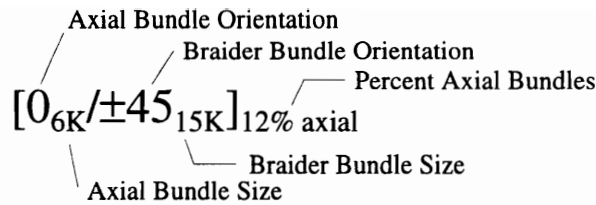
Figure 1.3 - Longhand Nomenclature for the Description of Two-Dimensionally Braided Composites

fibers. The second number in the brackets designates the angles of the braider fiber bundles with respect to the longitudinal axis. Its subscript designates the size of the braider fiber bundle in thousands of fibers. The final subscript designates the percent of the total areal weight of the preform that is occupied by the axial fiber bundles.

1.2 Experimental Testing Program

Two 12 inch by 24 inch plaques of each architecture were provided by the NASA Langley Research Center. These plaques were cut into specimens for each type of test, as listed in Table 1.2. First, static and tension and compression testing sequences were completed to determine strengths and basic characteristics of each architecture. Stress-strain behavior and damage mechanisms were studied and documented. This provided basic information needed for the fatigue testing sequences. For the fatigue sequence, a first group of specimens was tested to failure to determine peak stress level versus life relationships for both tension-tension and compression-compression fatigue loading. From this information, stress levels were chosen at which further specimens were tested

and stopped at specific times in their respective lives. These specimens were then x-rayed, sectioned, and photographed for documentation of damage mechanism types and initiation levels.

Table 1.2 : Test Matrix per Architecture for the Experimental Program

Test Type *	Number of Specimens	Specimen Size (inches) *	Test Conditions
Static Tension (straight sided)	5	1.0 x 7.75 (4.0 gage length)	0.01 in/min stroke controlled
Static Compression (IITRI)	5	1.0 x 5.5 (0.5 gage length)	0.01 in/min stroke controlled
Unnotched Tension-Tension Fatigue	4 3 3	1.0 x 7.75 (4.0 gage length)	5 Hz, alt. stress lvl.,to failure 5 Hz @ low stress level 5 Hz @ high stress level
Notched Tension-Tension Fatigue	3 3	1.0 x 7.75 (4.0 gage length)	5 Hz @ low stress level 5 Hz @ high stress level
Unnotched Compression-Compression Fatigue	10 6	1.0 x 4.7 (1.2 gage length)	5 Hz, alt. stress lvl.,to failure 5 Hz @ single stress level
Notched Compression-Compression Fatigue	6	1.0 x 4.7 (1.2 gage length)	5 Hz @ single stress level
* - LLL architecture had one less specimen per test type and 1.5 inch gage width			

Strain and load signals were continuously monitored by a data acquisition system developed for this research project. Continuous monitoring added the capability of analyzing each load cycle the specimen was subjected to, and calculating and displaying in real time, parameters of interest from the individual cycle. Along with the stress-strain information, all specimens were monitored throughout the test by a stereo microscope and video recording unit.

1.3 Modeling Techniques

Modeling of the material responses from the braided architectures was completed in two steps. In the first step, the static parameters measured in the static testing sequence were compared to those calculated using a classical lamination theory model. Elastic moduli and strength values were calculated and compared to the experimental results, as well as stresses in the laminated approximation of the braided materials. In the second step, the fatigue behaviors were modeled. For the tension-tension fatigue testing sequence, damage mechanisms which were determined to be major factors in the response of the braided materials were modeled. The classical lamination theory model developed for the static response was used as the base for a shear-lag modeling approach. The shear-lag model was used in conjunction with a power law assumption to yield a peak applied stress level versus cycle number relationship. The compression-compression fatigue response was found to be dominated by kink band formation. The factors leading up to the formation of kink bands are not well understood, and limited modeling efforts have been completed using idealized laminated material systems. The current papers are reviewed, and their application with respect to the braided architecture systems presented.

2. Literature Review

The present chapter is an extensive literature review covering experimental

characterization and modeling of textile composites. Because the work done in the area of

textile composites is somewhat limited, related research in the area of laminated

composites is also reviewed. First a general review of textile composites is presented

followed by general failure mechanisms in fatigue. A review of the literature in the area of

stiffness monitoring as a non destructive evaluation tool is presented to validate the

proposed experimental approach. Finally, the effects of fiber curvature in composites are

presented to establish background information on the effects these curvatures can cause in

the braided architectures.

2.1 Introduction to Textile Composites

Chou and Ko [1] edited a comprehensive work which discusses all types of textile

composites from fabrication processes to general mechanical and thermomechanical

behavior. Ko et al. [2] assembled a complete description of braiding types and geometries.

All types of braids and braiding processes were presented, along with a glossary of braiding nomenclature and braiding units. Familiarity with textile nomenclature is very helpful in understanding construction and comparisons between different types of textile composites. Construction of composite materials using advanced braiding and weaving processes have been in use for many years. Woven composites have long been used in fiberglass boat hulls because of their ability to assume the shape of the hull preform. Temple [3] reported that in 1971, the Rolls Royce Company began to research three-dimensional woven composites after having delamination difficulty with laminated composites. He concludes, however, that a significant problem that exists with textile processes is that damage to the fiber is nearly impossible to avoid. Florentine [4] introduced a weave type called the "Magnaweave Process". With this weaving process, three-dimensional preforms such as I-beams, H-beams, and stiffened panels can be woven directly. With the advent of computer controlled machinery, these weaving processes can produce much more complex parts [5-7]. Head [8] points out, however, that the cost of the equipment required to perform these weaving and braiding processes is high. Large pieces of machinery are required to produce small parts. Brookstein [9] introduced an improved braiding process which allowed fibers to interlock individual layers of two-dimensional braids, thus improving their shearing characteristics. The process is claimed to be more efficient and less cumbersome than conventional three-dimensional braiding processes, while still maintaining the original braiding capabilities. Many new braiding processes are in place at the present time, but specifics of the processes are considered proprietary by the

owners of the technology.

Application of textile composite technology is presented by several authors [5,6,10-14], ranging from sporting equipment to proposed space station components. It was reported that parts produced from textile composites exhibited greater resistance to thermally induced microcracking, enhanced damage tolerance, reduced weight, increased parts consolidation, and reduced production time and cost.

2.2 Experimental Testing of Textile Composites

Textile composites were initially studied because of their ability to sustain damage and still retain a large percentage of their initial elastic properties. Much of the early experimental work completed was in studying post impact properties. This work brought about the need to characterize the overall behavior of the textile systems, including documentation of stress-strain behavior and damage mechanisms. This section first presents work done in the area of impact and static mechanical testing of textile composites, for both tension and compression loading. Research in the area of fatigue testing of textile composites is then presented.

2.2.1 Damage Tolerance and Static Testing of Textile Composites

Ko [15] was one of the first researchers to publish in the area of mechanical testing of textile composites. Initial results published were from a wide variety of testing. In this

reference, results from static tension, flexural, and impact testing of three-dimensional braids were reported, as well as flexural testing of braided I-beams. It was concluded that Poisson's ratio and transverse properties could be controlled through proper selection of bundle size and braiding parameters. This result, coupled with the ability of the three-dimensional braids to sustain damage and constrain it to a small area, showed that textile composites could fill the need for net shape parts with high levels of damage tolerance. In a subsequent paper, Ko and Hartman [16] compared the impact behavior of three-dimensional braids, XYZ orthogonal weaves, and two-dimensional weaves. Three-dimensional braids have fiber bundles which are braided along all components of three-dimensional space, curving as need be to fit around adjacent fiber bundles. XYZ orthogonal weaves have fiber bundles oriented along the x, y, and z axis respectively. These fiber bundles are straight, and do not form around adjacent fiber bundles. Two-dimensional weaves contain fiber bundles oriented along the x and y axis. These fiber bundles usually follow some type of sinusoidal path in order to accommodate fiber bundles running along the opposing axis. It was found that no one energy parameter could characterize the impact behavior of these material systems. However, if impact damage area is quantified, the three-dimensional braid limited the damage to the smallest area, followed by the XYZ weave, and finally the two-dimensional weave. The authors concluded that higher levels of interlacing of bundles in textile composites lead to higher levels of damage tolerance. Li et al. [17] compared the two-step and four-step braiding processes with respect to impact behavior. It was found that the processing conditions

affected the damage tolerance as much as the braiding process itself. Packing the fiber

bundles in a denser fashion resulted in a smaller damage area. With respect to strength,

higher percentages of fibers oriented in the loading direction resulted in higher

compression strengths, but reduced damage tolerance. This is a result of damage

propagating along the paths of fiber bundles. The straighter the fiber bundle path, the less

energy required to travel a given distance along it. In a related paper, Li et al. [18] studied

damage tolerance from the standpoint of the unit cell size. The unit cell is defined here as

the smallest structural repeating unit of the architecture, and is mainly a function of the

bundle size and pitch length. Pitch length defines the height of the unit cell. It was found

that as the unit cell became smaller, i.e. smaller fiber bundles and/or shorter pitch lengths,

the damage tolerance increased. Hua et al. [19] studied open hole tension, open hole

compression, and impact properties of a three-dimensional braid impregnated with a

thermoplastic matrix. Composite systems were manufactured by commingling PEEK

fibers with graphite fibers. As compared to equivalent laminated composite systems, the

three-dimensional braids were found to have higher compression after impact strengths.

Fiber bundles oriented at angles perpendicular to the direction of crack propagation served

as crack arrestors, thus yielding smaller damage areas than those found in the equivalent

laminate. Simonds et al. [20] studied the effects of impact loading on the compression

strength of a three-dimensional braid. It was found that specimens which had been

subjected to an impact event of 5.4 J had no change in compression strength. Crane et al.

[21, 22] studied tension, compression, flexural, shear, and impact properties of three three-

dimensionally braided structures. Specimens with braided edges were compared to specimens with cut edges for each architecture. Specimens with braided edges were found to have a 45-60% increase in tensile properties and a 40% increase in flexural properties over specimens with cut edges. Impact testing also showed that the damage area was significantly smaller than that of a similar laminate.

Compression behavior of three different three-dimensional braids were studied in [23]. Carbon, S-2 glass, and Kevlar fibers were braided in similar fashions in order to study the effect of fiber material properties on compression behavior. It was found that compressive modulus was dominated by constituent material properties, while compressive strength was sensitive to the percentage of fibers oriented in the loading direction. The braids constructed from carbon and glass fibers failed by debonding and fiber microbuckling, while the Kevlar composites failed by fiber kinking and splitting.

Masters et al. [24] studied three different two-dimensional triaxial braids, very similar to those used in the present study. Static tension testing was completed on each of the architectures to determine moduli and strength values. While the moduli were found to be fairly constant with respect to small changes in architectural parameters, strength was found to vary significantly. No conclusion was reached which could describe this phenomenon. The same four architectures used in the present study were also studied by Naik, Ifju and Masters [25]. Moire interferometry was used to investigate strain variations on the faces of each architecture. Based on this testing, it was determined that larger fiber

bundles sizes led to higher normal strains, and cracking occurred much earlier under transverse loading conditions. Overall, composite properties were found to be more dependent on braid angle than on axial fiber bundle content.

Minguet, Fedro, and Gunther [26] carried out a test method determination program for several different types of textile composites. Test methods for virtually all types of static testing were studied. The main issue in the static tension work was to determine if specimen size had an effect on strength. No correlation between specimen size and strength was found for the two-dimensional braids identical to those used in this study. For open hole testing, a width/diameter ratio of six was determined to be a good rule of thumb for all the reported textiles. The Modified IITRII test fixture generally produced higher mean static compression strengths than other types of fixtures, while for shear testing, the Short Beam Shear fixture produced the highest mean strengths. In a related work, Minguet and Gunther [27] completed a comparison between two-dimensionally braided composites and equivalent graphite/epoxy tape laminates. Static tension, static compression, shear, and bolt bearing tests were completed for each material. Results indicated that while the longitudinal modulus of both composites were approximately the same, the transverse moduli of the braids was significantly lower than the tape laminates. The unnotched longitudinal strength of the tape laminates was higher, while the notched longitudinal strength of the braids was higher. Under compression loading, the braids were weaker in both notched and unnotched configurations. Shear strengths of the braids

were also lower than the equivalent tape laminates.

Notched testing of textile composites is a more complex issue than notched testing of conventional laminated composites. Typically, laminated composites contain a hole or notch which is sized in proportion to the specimen width. The hole or notch sections the various lamina residing at constant angles and depths regardless of position on the overall plate. Therefore, hole position in a laminated architecture is ideally of no significance. In a textile, however, the size of the hole or notch with respect to the specimen width, where the hole is drilled with respect to the fiber architecture, the coarseness of the fiber architecture, and whether or not the hole was woven into the specimen or cut are all very important factors. The latter is the only factor to be published in the literature. Chang et al. [28] found specimens with woven-in holes to have tension strength increases as much as 38% as compared to specimens with cut holes. Arendts and Drechsler [29] studied the effects of working holes into laminates and textiles. This is done by working a pin through the preform of the material, and displacing fiber bundles without cutting them. However, the experimental results showed no improvement in tension properties from worked in holes compared to cut holes. Li et al. [30] studied the effects of three different kinds of holes in a three-dimensional braid: 1) cut, 2) worked in, and 3) braided. Specimens were subjected to tensile and compressive bearing tests. Equivalent specimen strengths were found for each of the hole types. The authors pointed out, however, that the braided-in hole required less machining after consolidation. Fujita et al. [31] studied the effects of

machined holes versus braided holes in flat braided bars with both cut and uncut edges. The specimens with uncut edges and braided holes showed a significant improvement in tensile strength as compared to the cut hole specimens. In the specimens with cut edges, no such improvement was found.

2.2.2 Fatigue Testing of Textile Composites

There is a limited amount of information available regarding the fatigue behavior of textile composites. The earliest published work in this area was in 1985. The following section covers the available literature on the fatigue response of various forms of textile composites.

In order to determine degradation mechanisms in woven composite, Kobayashi and Ohtani [32] used the dark field and Kohler illumination techniques to study cracking processes. Glass fibers were used in the fabric which allowed these techniques to be applicable. The authors were able to show that there is a linear dependence between the number of fiber breaks and increase in delamination area between the individual woven layers as the cycle number increased. Further, the strength and stiffness of the specimens were found to decrease with increasing cycles. The stiffness decreased in a linear fashion, while the residual strength was found to decrease nonlinearly, showing a lesser cycle dependent sensitivity. Shulte et al. [33] investigated two woven composite systems consisting of carbon and aramid fibers respectively. A third material system was also

investigated which consisted of a 50/50 blend of the two types of fibers. These textile systems were compared to an equivalent laminated composite. It was determined through fatigue testing that the laminated composite displayed superior fatigue response as compared to the textile composites. Carbon fibers proved to have better fatigue characteristics than the aramid fibers, both in the same resin system. Failure mechanisms were cracks in the transverse bundles, and delaminations at the cross over points of the longitudinal and transverse fiber bundles. Gause et al. [34, 35] were the first to publish research on fatigue properties of braided composites. Two braided composite systems were compared to an equivalent laminate. The braids each had the same overall fiber volume fraction and were termed type I and type II. The type I braid had all fibers oriented at ±20° to the loading axis, while the type II braid had 50% of its fibers held straight, and the other 50% braided around and at an angle of ±20° to the fibers held straight. Both braid types were found to exhibit very similar behavior under tension-tension and tension-compression fatigue loading. Under compression-compression fatigue testing, type II braids had longer lives than type I braids. In all three types of fatigue loading, the equivalent laminate had longer lifetimes than the braided composites. Comparable peak loading amplitudes were determined by keeping the ratio of the static strength divided by the peak load constant. Specimens were also monitored with a thermocouple during testing to monitor temperature increases. At test frequencies of 5 Hz, no significant heating was found. Simonds et al. [20] studied the effects of reversed loading fatigue on three dimensional braids. Static tension and compression properties were first measured

from both impacted and unimpacted specimens. Further specimens were then subjected to

fully reversed fatigue loading. It was found that fatigue lives and failure modes were the

same for both impacted and unimpacted specimens. Stiffness monitoring indicated that the

only difference between impacted and unimpacted specimens was changes in rates of

stiffness loss in the last 30% of life. This was attributed to localized failure processes in

individual specimens. Chou et al. [36] tested several different types of textile composites

in fatigue, consisting of both carbon and E-glass fibers. The effects of hysteresis heating

were studied by varying stress levels at a constant frequency of 30 Hz, and monitoring the

temperature of the specimen surface with thermocouples. It was found that stress levels

above 100 MPa produced significant hysteresis heating effects. Below this stress level,

hysteresis effects were minimal. Specimens made from carbon fibers were found to have

longer fatigue lives and smaller damage propagation rates as compared to those made

from E-glass fibers. Billaut and McGarry [37] constructed laminates with plain weave

fabric by orienting the 0/90 plain weave layers to create $[0/\pm45/90]_s$ and $[0/90]_{2s}$

"laminates", impregnated with a PEEK thermoplastic matrix. All specimens contained a

12.7 mm diameter hole. Both layups showed very different damage responses with respect

to static and fatigue loading. In static loading, very little damage, with no fiber breakage

occurred until ultimate failure. In fully reversed fatigue, large damage zones and fiber

breakage was found around the hole, well before ultimate failure. This was attributed to a

decrease in the resistance to splitting and debonding as the number of cycles increased.

Damage was first found in the form of debonding of the fiber bundles, followed by

microbuckling of the surface bundles. Fatigue damage zone sizes were also determined

beyond which residual strength began to decrease.

Cox et al. [38] studied the effects of a full range of test types on several different

interlocking weaves. These architectures are termed interlocking due to fiber bundles

which run through the thickness of the weave, locking the layers together. These

interlocking fiber bundles can run orthogonally, or at specified angles in the material. Of

particular interest in this study is the comparison of monotonic and fatigue damage

mechanism types and orders. In static compression, cracking in the matrix was found to

trigger failure in stuffers, which are the primary load carrying fiber bundles in this woven

composite. In compression-compression fatigue, increased cyclic loading weakened the

resin in the stuffers, thus reducing load transfer between adjacent fiber bundles, and

lowering the critical load for the formation of kink bands in the stuffers. Under tension-

tension and tension-compression fatigue, matrix cracking formed and increased in density

with an increasing number of cycles. Final failure was found to be rupture of the load

bearing fiber bundles. Correlation was also found between areas of misalignment and

rupture.

2.2.3 Modeling of Textile Composites

Several different methodologies have been applied to modeling textile composites,

ranging from classical lamination theory approximations to finite element analyses of the

textile microstructure. This section reviews work published in the area of strength and stiffness modeling of textile composites.

Halpin et al. [39] were the first to apply the principles used for laminated composites to textile composites. Equivalent laminates were assumed for different textile composites, and values calculated were compared to those measured. The method was found to produce acceptable results for two and three-dimensional weaves. Other researchers [21, 24, 35] also used classical lamination approximations for braided composites, and determined it to be an acceptable tool for elastic properties. Chou, Ma, and Yang [40-42] applied stiffness reduction adjustments to the in-plane stiffnesses within the context of classical lamination theory, again applying this method to textile composites. Good agreement was found between experimentally determined and calculated values of elastic moduli and thermal coefficients. Dadkhah et al. [43] also used stiffness reduction techniques to turn undulating fiber paths into equivalent lamina. Ko [44] adjusted fiber bundle properties to account for differences in direction within unit cells of three-dimensional braids. The model produced equations which use the cosine of the adjustment angle to reduce stiffness and strength values. Strength and stiffness predictions were found to have differences of up to 20% with experimentally determined values.

Raju et al. [45] compiled a description of current models used for textile composites. Models were divided into three groups: 1) elementary models, 2) laminate theory models, and 3) numerical models. Elementary models are generally very simple approximations to

determine static properties, such as netting analyses. Numerical models generally refer to finite element modeling techniques. This reference contains a description of a model developed by Foye which discretizes the unit cell into subcells, which are then modeled as inhomogeneous hexahedral finite elements. This technique is termed the "Fabric Analysis Method" by the author. Knowledge of the unit cell structure of a given textile composite, along with constituent material properties, allows the analyst to study a wide variety of textile composites. In a two part work, Fujita et al. [46] studied differences in cut versus braided edges in two-dimensionally braided composites. Finite element analysis was used to study the differences between the two cases. "Part Models" were constructed which involved dividing the specimen into three parts: left and right edges, and a center section. Beam elements were used to model the matrix and fiber bundles separately in straight sections. Damage progression was modeled by removing elements representing matrix when they reached a stress level at or exceeding their failure level. When elements representing fiber bundles reached a stress state equal to or greater than their failure stress level, global failure was assumed and the calculation stopped. Failure stress predictions were within 13% of the measured values for the modeled composite. In an extension of this research [31], the authors used the same technique to model cut versus braided holes in the same architecture. Calculated strength values were again within 13% of the measured values for each type of hole configuration. Masters et al. [24] modeled two-dimensional triaxially braided composites using classical lamination theory both uncorrected and corrected for fiber bundle undulations, a diagonal brick model, and finite

elements. Very close agreement was found between all three types of analyses for elastic constants, however the predicted values more closely matched the measured values as the complexity of the analysis increased. Pastore [47] presented an introduction to the modeling aspects of textile composites, as well as a methodology for different aspects of modeling. Methodologies for elastic properties, deformation and strength, and reliability for both material systems and structures were presented. Naik [48] developed a computer code which predicts elastic moduli and strength for textile composites named TEXCAD. This program starts with geometric information on the unit cell of the textile composite. Fiber bundles are assumed to have lenticular cross-sections, as this most closely represents shapes found in actual micrographs. Fiber bundles are discretized into individual slices, and material properties, spatial orientation, and volume fractions are assigned to each slice. The solution is obtained using a iso-strain assumption within the unit cell of the textile architecture. Predictions from this code were presented in [25]. Predicted values for elastic constants were in excellent agreement with measured values. Cox et al. [38] formulated a numerical model termed the "Binary Model". This model consists of as assemblage of tow elements in an effective medium. This assemblage was solved using a commercial finite element solution package. The model was refined further to simulate fatigue loading cases. Element strengths decayed as a function of the number of load cycles, and were considered to fail when the load the element carried equaled its strength at that point in life.

Fatigue modeling of textile composites is still in early stages of development. The previous reference has an analytical formulation, but no rigorous experimental correlation. Most fatigue modeling done to this point has consisted of empirically determining rates for analytically formulated stiffness/damage relations. Chou et al. [36] followed a formulation by Beaumont which assumed a stiffness versus damage relationship for the particular material of interest, and a rate law which the material follows. The rate parameters were then determined empirically. The research by Beaumont is reviewed in the following section. Dadkhah et al. [49] assumed that the critical shear stress for shear flow in the matrix decays as a power of the local axial shear stress. A fatigue law relating the number of cycles to the applied stress and misalignment angle of fiber bundles was assumed. The rates for this law were then empirically determined through a curve fitting scheme.

2.3 Fatigue of Laminated Composites

In order for a review on fatigue testing and modeling of textile composites to be complete, work done in the same area on laminated composites must also be reviewed. The following section presents a brief overview of related work in the areas of damage study and modeling of laminated composites.

Reifsnider and Williams [50] were the first to measure and characterize the heat generated during cyclic loading of Boron/Epoxy and Boron/Aluminium laminated

composites. Tests were run at frequencies ranging from 1/2 to 45 Hz on specimens containing a flaw in the form of a center notch. All frequency ranges showed an initial period of heat generation. At frequencies below 15 Hz, a steady temperature state was reached, while frequencies of 30 and 45 Hz showed a secondary period of heat generation which continued to increase. This secondary period was also accompanied by a progressive reduction in stiffness, and an increase in hysteresis.

Reifsnider and Jamison [51] presented some of the earliest research on correlating material response to individual damage mechanisms under fatigue loading. Specific mechanisms were found which were associated with fatigue damage, however, it was noted that no mechanics based rate relationship was able to be determined. The authors point out that this is not only specific to composite materials, but to all engineering materials. Rates are only able to be determined empirically, not from mechanics based formulations. The main point of the research was to point out that internal stress redistributions resulting from fatigue loading are of the type and magnitude to validate changes in measured residual strengths. Reifsnider, Shulte, and Duke [52] studied long term fatigue behavior under both tension-tension and compression-compression fatigue. For tension-tension loading, long-term behavior was divided into three regions: 1) an initial region where cracking in the off-axis plies occurred (characteristic damage state), 2) a region in which these cracks couple and grow, and 3) a rapidly occurring region where fracture of the 0° fibers caused global laminate failure. Cracking in the off-axis plies was

also found in static loading. Termed the characteristic damage state (CDS), this behavior was found to fully develop in both static and fatigue loading. Therefore, the residual strength of long-life specimens did not significantly drop until region three had been reached. In compression-compression fatigue loading, damage development was found to be dominated by delaminations at regions of high interlaminar shear stress along the edges of the specimen. This allowed delamination and finally buckling and fracture of the outer layers of the composite. They found that tension-compression fatigue loading produced a "worst case" condition, as the two types of damage work together to produce a severe loading case. Jamison et al. [53] extended the work presented in reference [52] by studying several different laminated composites subjected to tension-tension fatigue loading. Harrison and Bader [54] also reported cracking in the off-axis plys as the first damage mechanism caused by tension loading. Strain levels at which this type of cracking occurred were found to be lower under fatigue loading than under static loading. At the preset load level used, crack densities in the off-axis plys reached a constant value after approximately 10^3 cycles. After this point, the cracks were found to couple and propagate.

Ramani and Williams [55] studied the effect of notches in $[0/\pm\theta]_{3s}$ and $[0/\pm\theta/0]_{2s}$ laminates ($\theta = 30°$ and $45°$) subject to static and fatigue loading. These types of laminates are of interest to the present work because their laminate stacking sequence is one commonly used to model triaxially braided architectures. Under static tension and compression loading both laminates showed a significant notch sensitivity, while under

tension-tension fatigue, no notch sensitivity was found. Damage in a specimen with a circular center hole was contained within vertical lines running parallel to the loading axis, bounded by the edges of the hole.

Research in the area of compression-compression fatigue is sparse at best. Most works done in the area only brush the surface and define the area as future work. Black and Stinchcomb [56] presented the most complete body of work in the area of compression-compression fatigue of notched laminates. Notched specimens were tested in an unsupported grip configuration utilizing the hydraulic wedge grips of a standard servohydraulic test frame. Damage was monitored using stiffness loss information, x-ray radiography, and ultrasonic C-scans. Damage in the laminates was determined to be matrix cracking and delaminations, both of which occurred early in the cyclic loading history. The Poisson secant modulus was reported to be more sensitive to damage than was the longitudinal secant modulus.

Damage modeling of composite materials subject to various types of fatigue loading is a very complex issue. There is no model in existence that can predict fatigue characteristics of a given composite system based solely on an analytical development. Models rely on various experimentally determined parameters to complete their predictions of the material behavior. Damage modeling originates from two bases: 1) continuum modeling, and 2) microscopic modeling. Continuum modeling of composite materials becomes very complex and much of the time requires experimentally

determined parameters which are extremely difficult and expensive to determine.

Microscopic modeling usually involves broader, mechanics of materials based

assumptions, however the required experimental data is usually of a form which can be

easily measured. Highsmith, Stinchcomb, and Reifsnider [57] presented a framework in

which fatigue modeling of composite materials can be completed. The idea of subcritical

and critical elements was introduced where subcritical elements effect the manner in

which local stress redistribution and geometric changes take place as damage occurs, and

critical elements control the state and overall failure of the material. This philosophy was

expanded by Reifsnider in [58]. The idea that the damage mechanisms which control

failure must first be determined experimentally is put forward. This allows the

determination of a characteristic damage state along with subcritical and critical elements.

Once this data has been gathered, the modeling of the material system can be completed,

relating the damage state of the material to its residual properties. A similar methodology

has been developed by Beaumont [59] approaching the problem from a slightly different

angle. A coupling of the continuum approach and the microscopic approach is presented

in a framework termed "model informed empiricism", which provides an avenue for

"predictive design". The goal of the modeling is to provide the designer a usable tool to

aid in the design process. Relationships between damage types and residual stiffness and

strength are formulated, simplified where necessary, and empirically matched to

experimental data to produce a simple equation relating damage and life of the material

system of interest. This work was extended by Spearing and Beaumont [60-61] and

Kedward and Beaumont [62], applying it to several different types of composite materials and testing configurations.

2.4 Stiffness Loss Monitoring of Composite Materials

Nondestructive evaluation (NDE) of composite test specimens has received considerable attention from researchers. Nondestructive techniques which can be used in-situ have proven to be very valuable tools in the study of damage mechanics in composite materials, allowing the researcher to correlate specific damage mechanisms to characteristic responses of the chosen technique. This section reviews research in the area of stiffness monitoring as a nondestructive measurement tool for the study of composite materials.

O'Brien and Reifsnider [63] used stiffness monitoring along with reduced stiffness analyses to study stiffness loss versus strength relationships in laminated composites subject to fatigue loading. It was determined that there was a definite correlation between static stiffness changes and matrix damage in the form of matrix cracking and debonding. Although the data were reported as preliminary by the authors, an emphasis was given on the need for further work in the area. O'Brien [64] then specifically studied the use of stiffness change as a nondestructive tool in damage study. Stiffness change was used to predict failure in fatigue tests. The author concluded that stiffness measurement both statically and in real time is a very useful tool in the study of damage mechanisms for a

wide variety of test types and material systems. Camponeschi and Stinchcomb [65] compared stiffness loss information with C-scans and edge replications for graphite/epoxy specimens subject to tension-tension fatigue loading. This coupled stiffness loss and damage mechanism information allowed the authors to more decisively conclude on various aspects of material behavior at specific points in the loading history. O'Brien and Reifsnider [66] applied continuous monitoring of stiffness in the study of boron/epoxy laminates subject to fatigue loading. Different types of fatigue failure criterion based on stiffness loss were studied. Sims and Bascombe [67] continuously monitored glass fiber/ epoxy composites, analyzing dynamic moduli and hysteresis information throughout the test. It was concluded that the additional information was extremely valuable in reduction of the fatigue data, especially when a limited number of specimens were tested. Continuous monitoring of stiffness in graphite/PEEK composites was completed by Picasso and Priolo [68]. Comparisons of the shapes of stiffness loss curves with graphite/ epoxy were made based on the continuous monitoring of the test specimens.

2.5 Fiber Waviness Effects in Laminated Composites

The effects of fiber waviness are of great concern in textile composites due to the extreme fluctuations in fiber bundle orientations. Of particular concern in the present research is the sinusoidal fluctuations of axial fiber bundles along their length. Ideally, the two-dimensional triaxial braids have perfectly straight axial fiber bundles. In reality however, the individual braided layers are compacted during the manufacturing process,

thus introducing the sinusoidal variations into the axial bundles. Adams and Hyer [69] present an excellent literature review on the effects of fiber and layer waviness up to 1992. The basis and progression of fiber and laminate waviness modeling is reviewed. Research on the effects of layer waviness is also presented. It was generally reported that the higher the degree of fiber or lamina waviness, the more severe the reduction of compression strength and modulus. Recently, Chan and Wang [70] studied the effect of fiber waviness on the structural response of laminates. It was found that the more pronounced the fiber waviness, the greater the decrease in stiffness, particularly if the waviness occurs in a primary load carrying ply. Increased waviness also decreased the natural frequency of the laminate.

3. Static Tension Testing

Static tension testing was completed in order that damage types and sequences could be established and understood as a precursor to tension-tension fatigue testing. This chapter presents experimental results from static tension testing of the four braided architectures initially presented.

3.1 Test Specimen Fabrication

Individual specimens were cut from the main plaque using a water cooled diamond blade saw. All specimens had a total length of 7.75 inches as shown in Figure 3.1. The specimen width was 1.0 inches for all except the LLL architecture which had a specimen width of 1.5 inches. Edges which were to be monitored with optical microscopy during testing were polished using 0.05 micron alumina paste on a micropolish cloth. Strain gages were applied on the gage section by first lightly wet sanding the face of the specimen where the gage would be located. The surface was then cleaned with acetone, and the strain gage was aligned with the specimen using cellophane tape. Finally, the gage was mounted to the surface using M-Bond 200® cyanoacrylate glue.
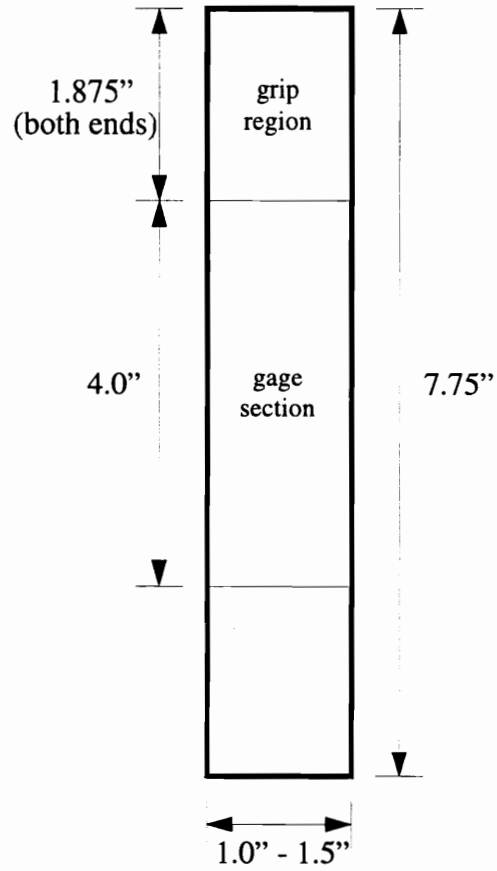
Figure 3.1 - Specimen Dimensions for Static Tension Testing

3.2 Experimental Program

The testing program consisted of five tensile specimens from each architecture, with the exception of the LLL architecture which consisted of four specimens. The first two specimens (one for the LLL architecture) were tested at a constant crosshead rate of 0.025 in/min on a 20 kip Instron screw driven load frame. During the test, the free edge was monitored with a Wild stereo microscope equipped with a 35mm camera. Strain was monitored with a 1" MTS extensometer and recorded simultaneously with the load cell output at a rate of one sample per second. A third specimen from each architecture was then tested in the same fashion, with the exception of the Wild stereo microscope being equipped with a video camera and recording unit. The strength numbers obtained from these specimens were averaged to determine estimates of the static strength of each architecture. The final two specimens were then tested at the NASA Langley Research Center utilizing in-situ x-ray capabilities. Static tensile tests were run at a constant crosshead rate of 0.025 in/min on a 20 kip MTS servohydraulic load frame. Longitudinal strain was monitored by a 0.5 inch by 0.5 inch strain gage (EA-06-500AF-120) and recorded simultaneously with the load cell output at a rate of one sample per second. Specimens were tested to a predetermined strain level, the load was lowered to approximately 100 pounds, and the specimen was then dyed and x-rayed. Dye was allowed to remain on all faces of the specimen for five minutes between each iteration. Once the iteration was completed, the specimen was tested to the next strain level. The

first specimen was tested to approximately 60% of the ultimate failure strain, while the second specimen was tested to approximately 80% of the ultimate failure strain.

All specimens that were tested to ultimate failure were dyed and x-rayed in a cabinet x-ray unit to determine internal characteristics of the failure. Edges and faces of these specimens were also studied and photographed with the Wild stereo microscope. Specimens subjected to the in-situ x-ray monitoring were sectioned as shown in Figure 3.2. The specimen was first cut in two halves along a line parallel to the axial bundles. The interior edge of one half was dyed and that half x-rayed in order to examine possible edge effects. The second half was sectioned at several locations in order to yield micrographs at the external edge, internal edge, perpendicular to axial bundles, and parallel to the braider bundles.

3.3   Discussion of Results

3.3.1 $[0_{6K}/\pm45_{15K}]_{12\% \, axial}$ (LSS) Architecture

The LSS architecture was characterized by an axial bundle size less than half its braider bundle size. This was a much smaller axial bundle size compared to the other three architectures, where the axial/braider bundle ratio was two or more. This architecture consisted of five individual layers of braided mat. Measured material properties are listed in Table 3.1.

Braid Angle

Inside Edge

Outside Edge

Horizontal

Split Specimen Along Axial Bundles
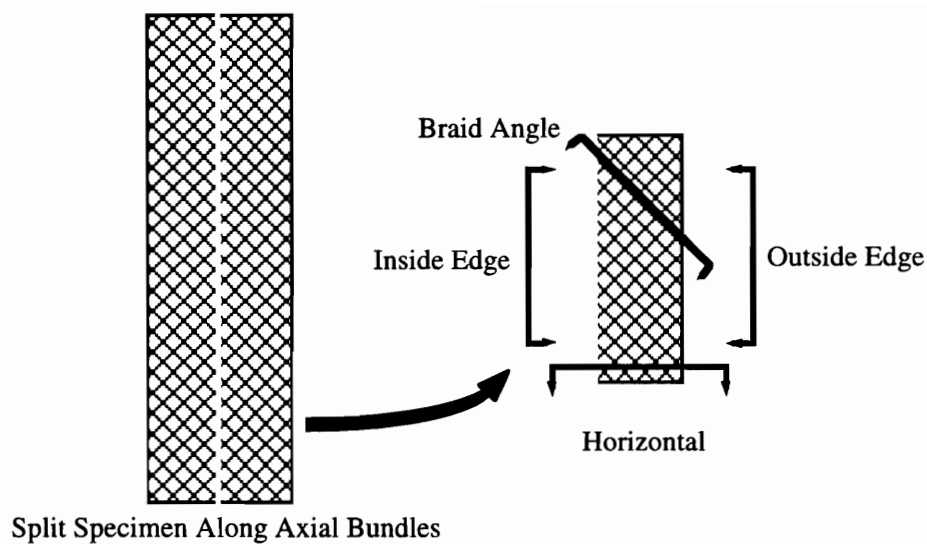
Figure 3.2 - Sectioning Schematic for Static Tension Specimens from the X-Ray Sequence

Table 3.1 : Measured Tensile Properties for the LSS Architecture

Specimen #	Elastic Modulus (Msi)	Ultimate Strength (ksi)	Ultimate Strain (%)
1	5.29	53.4	1.26
2	5.01	53.6	1.28
3	5.23	54.0	1.19
avg. ± std. dev.	5.18±0.15	53.7±0.3	1.24±0.05

Stress versus strain curves for the three LSS specimens tested to failure are shown in Figure 3.3. The overall response of the three specimens was very consistent. This architecture exhibited the most nonlinear stress-strain response, lowest longitudinal modulus, lowest strength, and highest strain to failure of the four architectures tested. This was due to the high percentage of braider bundles oriented at ±45° to the loading axis. Because the architecture contained only 12% axial bundles, the overall behavior was dominated by the characteristics of the braider bundles. With 88% of the total composite being oriented at ±45° to the loading axis, the test simulated an off-axis shear test. This produced a nonlinear stress-strain response due in large part to the high shear strains in the ±45° braider bundles, and a lower longitudinal modulus as compared to the other three architectures.

The main form of damage found in static tension specimens from the LSS architecture was splitting in the braider fiber bundles. Audible popping sounds began
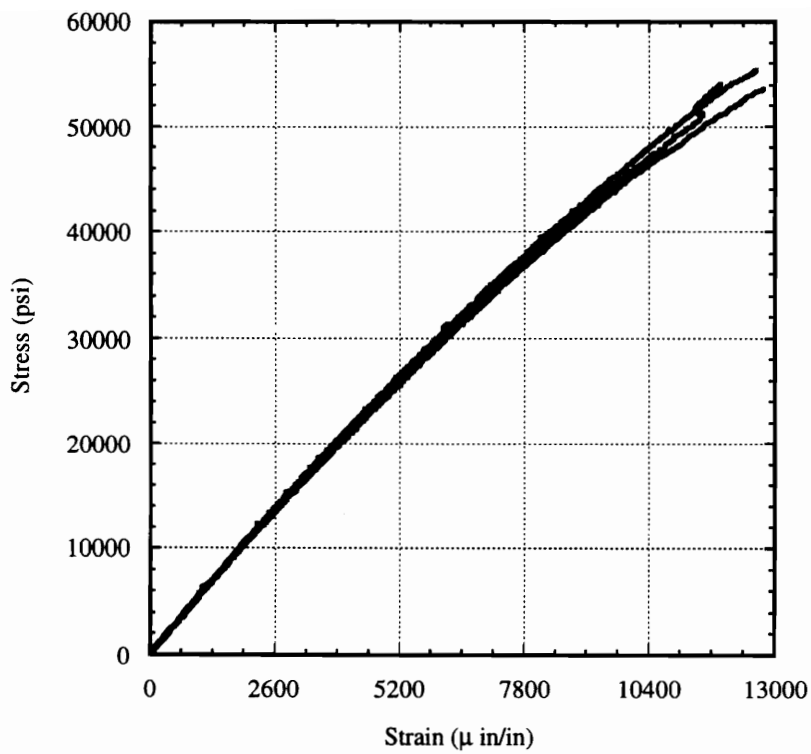
Figure 3.3 - Stress vs. Strain Response for Three LSS Architecture Specimens Tested to Ultimate Failure

between 0.3% and 0.4% strain which corresponded with levels at which cracks in the braider bundles were first seen through the microscope focused on the edges of the specimen. Splits in the braider fiber bundles continued to form as the test progressed up to the ultimate failure point of the respective specimen. Disbonding of the axial fiber bundles from their surrounding constituents was observed on the free edge of the specimen at load levels very near failure. This disbonding was also accompanied by splits running along the longitudinal axis of the axial fiber bundles. The final failure mechanism was rupture of the axial fiber bundles.

3.3.2 $[0_{36K}/\pm45_{15K}]_{46\% \ axial}$ (LLS) Architecture

The LLS architecture had an axial fiber bundle size over two times the size of the braider fiber bundles. The architecture consisted of three individual layers of braided mat. The axial fiber bundles were six times larger than those in the LSS architecture, while the braider fiber bundle size was constant between the two architectures. Therefore, an evaluation of the effect of axial fiber bundle size on the braided architecture was completed by comparing the results from the LSS architecture to those from the LLS architecture. Measured material properties for the LLS architecture are listed in Table 3.2.

Table 3.2 : Measured Tensile Properties for the LLS Architecture

Specimen #	Elastic Modulus (Msi)	Ultimate Strength (ksi)	Ultimate Strain (%)
1	10.6	80.3	0.77
2	12.3	96.4	0.78
3	9.6	103.8	1.19
avg. ± std. dev.	10.8±1.4	93.5±12.0	0.91±0.24

Stress versus strain curves for the three specimens tested to failure from the LLS architecture are shown in Figure 3.4. The response was mostly linear until the latter stages of the test, indicating the dominance of the large axial bundles. Unlike the other three architectures which produced popping noises consistently from very early on in the test, the LLS architecture produced very little audible noise until the specimen was near ultimate failure. Splitting of the braider fiber bundles occurred at approximately 90% of the ultimate failure strain. Splitting in the axial fiber bundles was also found near ultimate failure, as shown in Figure 3.5. A curved region of an axial fiber bundle, shown in the micrograph spanning the picture from left to right, was found to contain splits along the longitudinal direction of the axial fiber bundle, which occurred at approximately 80% of the ultimate failure strain. No damage was found in the x-ray specimens even up to 80% of the ultimate failure strain. The final failure mechanism was rupture of the axial fiber bundles.
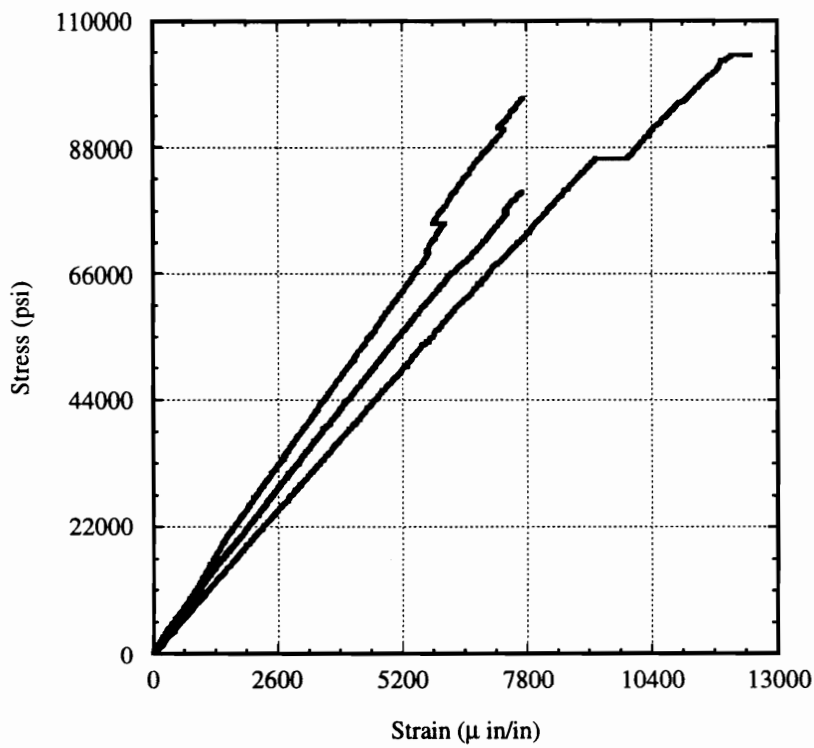
Figure 3.4 - Stress vs. Strain Response for Three LLS Architecture Specimens Tested to Ultimate Failure

3.3.3 $[0_{30K}/\pm70_{6K}]_{46\% \, axial}$ (SLL) Architecture

The SLL architecture was characterized by a very small braider bundle size, which yielded an axial bundle/braider bundle size ratio of five. The architecture consisted of four individual layers of braided mat. This architecture was used to study the effects of scaling, as the braider and axial fiber bundles were each six times smaller than the corresponding bundles in the LLL architecture. Measured material properties are listed in Table 3.3.
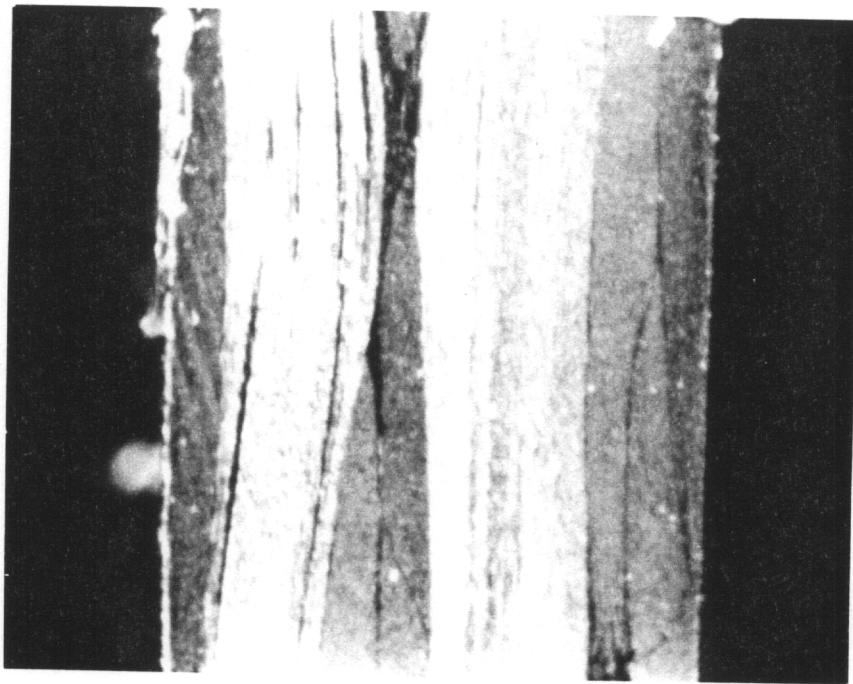
Figure 3.5 - Splitting in a Curved Region of an Axial Fiber Bundle in the LLS Architecture

Table 3.3 : Measured Tensile Properties for the SLL Architecture

Specimen #	Elastic Modulus (Msi)	Ultimate Strength (ksi)	Ultimate Strain (%)
1	10.36	121.9	1.23
2	9.55	117.8	1.33
3	9.26	127.4	1.43
avg. ± std. dev.	9.72±0.6	122.4±4.8	1.33±0.1

Stress versus strain graphs for the three specimens tested to failure from the SLL architecture are shown in Figure 3.6. All specimens had very linear responses until near the ultimate failure point. Audible popping noise began between 0.3% and 0.4% strain, and continued until ultimate failure. This noise was associated with splits in the braider fiber bundles seen on the free edges of the specimens through the stereo microscope. The in-situ x-ray testing sequence detected a additional damage mechanism type for one of the two specimens tested. A radiograph from a damaged specimen which contained splits in the braider fiber bundles much like that found in the LSS and LLS architectures is shown in Figure 3.7 (SLL-1). A radiograph at a comparable strain level from the second specimen tested is also shown in the figure, which showed splits running along the length of the axial bundles (SLL-2). The splits in the braider fiber bundles are represented by dark lines running at angles of ±70° to the vertical direction, while splits in the axial fiber
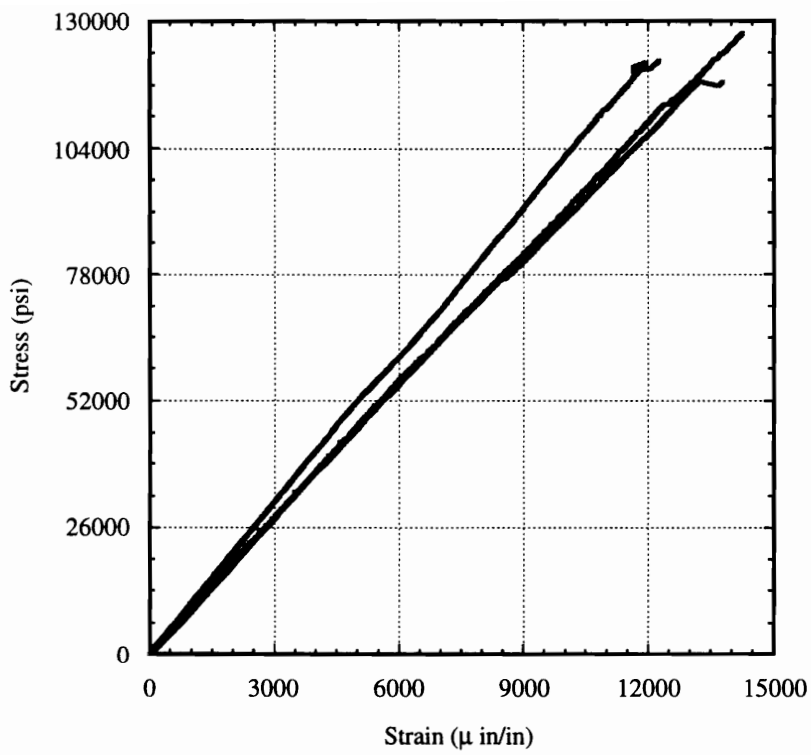
Figure 3.6 - Stress vs. Strain Response for Three SLL Architecture Specimens Tested to Ultimate Failure

bundles are represented by dark lines running vertically in the radiograph. The difference between the two specimens was in the stacking sequence of the individual braided layers of the architectures, as shown in Figure 3.8. The first specimen (SLL-1) contained layers that were oriented such that the axial fiber bundles for each respective layer were on top of each other in the thickness direction. The second specimen (SLL-2) contained layers which were nested. "Nesting" refers to a stacking sequence in which the axial fiber bundles from one layer reside between the axial fiber bundles of the layers above and below the respective layer, as shown in the figure. The "nested" specimen developed splits in both the braider and axial fiber bundles, while the "stacked" specimen developed splits
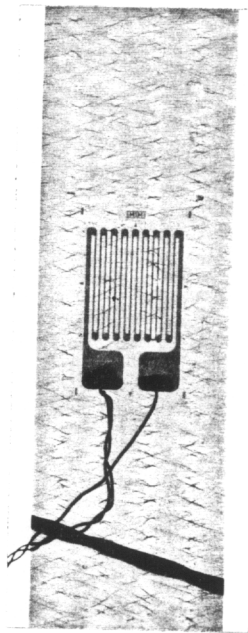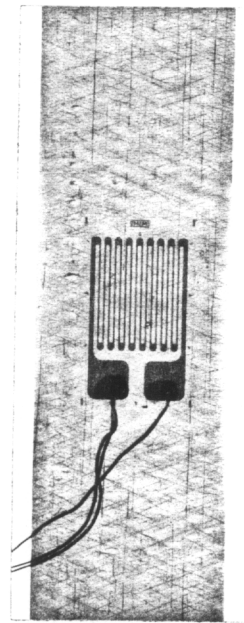
SLL-1   SLL-2

Figure 3.7 - Radiographs from Two SLL Architecture Specimens with Different Stacking Sequences (both at ~0.6% strain)

Braider Bundles

Axial Bundles
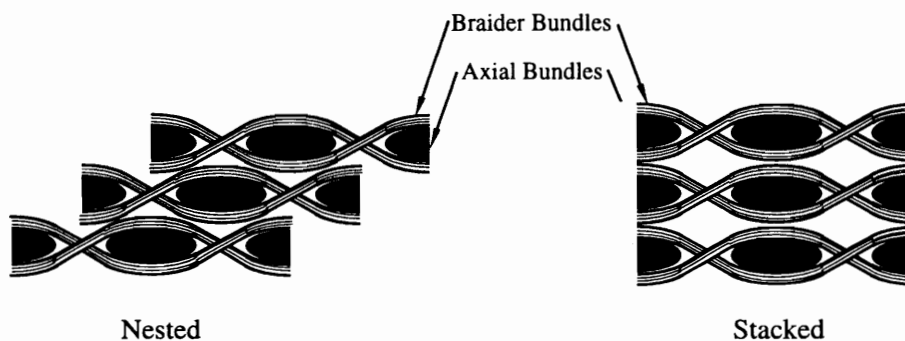
Nested

Stacked

Figure 3.8 - Nested and Stacked Configurations in 2-D Triaxially Braided Composite Structures

in the braider fiber bundles only.

Another response unique to the SLL architecture was the behavior along the free edge of the specimen. In several specimens, the layer on one of the faces split open along the free edge as indicated by the dark region on the left edge in Figure 3.9. The fracture was, however, arrested by the next axial fiber bundle inward in its respective layer. In many cases, the split ran along the entire gage length of the specimen. Although this appears as a very large damage region on the radiograph, it was actually a very minor damage sequence, occurring at approximately 50% of the failure strain. No significant stress-strain response differences were attributed to this damage mechanism. The final failure mechanism was rupture of the axial fiber bundles.

3.3.4 $[0_{75K}/\pm70_{15K}]_{46\% \ axial}$ (LLL) Architecture

The LLL architecture was the coarsest of the four architectures, with an axial bundle size over twice that of any of the other architectures. Because the axial fiber bundles were larger, the preform contained resin pockets with dimensions on the order of several millimeters. These pockets were typically located between the axial bundles of a single layer. Measured material properties for the LLL architecture are listed in Table 3.4.
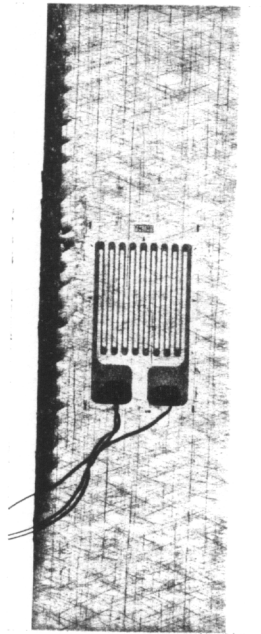
Figure 3.9 - Micrograph of a Static Tension Specimen from the SLL Architecture Showing Damage at the Free Edge of the Specimen

Table 3.4 : Measured Tensile Properties for the LLL Architecture

Specimen #	Elastic Modulus (Msi)	Ultimate Strength (ksi)	Ultimate Strain (%)
1	9.11	72.3	1.06
2	8.45	69.0	0.81
avg. ± std. dev.	8.78±0.47	70.7±2.3	0.93±0.18

The stress versus strain response for the two specimens tested to failure from the LLL architecture is shown in Figure 3.10. Each specimen displayed a nearly linear response until shortly before ultimate failure, when large fluctuations in the strain readings occurred which corresponded with loud popping noises. The initial damage mode was splitting in the braider fiber bundles and cracking in the resin rich pockets. The cracks in the resin rich pockets were oriented in the same directions as those in the braider bundles. A radiograph of a specimen containing this type of damage is shown in Figure 3.11. The cracks and splits are represented by thin dark lines running at an angle of ±70° to the longitudinal axis of the specimen. Audible popping noises began between 0.3 % and 0.4% strain, and continued until shortly before ultimate failure of the specimen.

Splitting in a curved region of an axial fiber bundle along its length is shown in Figure 3.12. This damage mechanism was also found in the LLS architecture. The strain
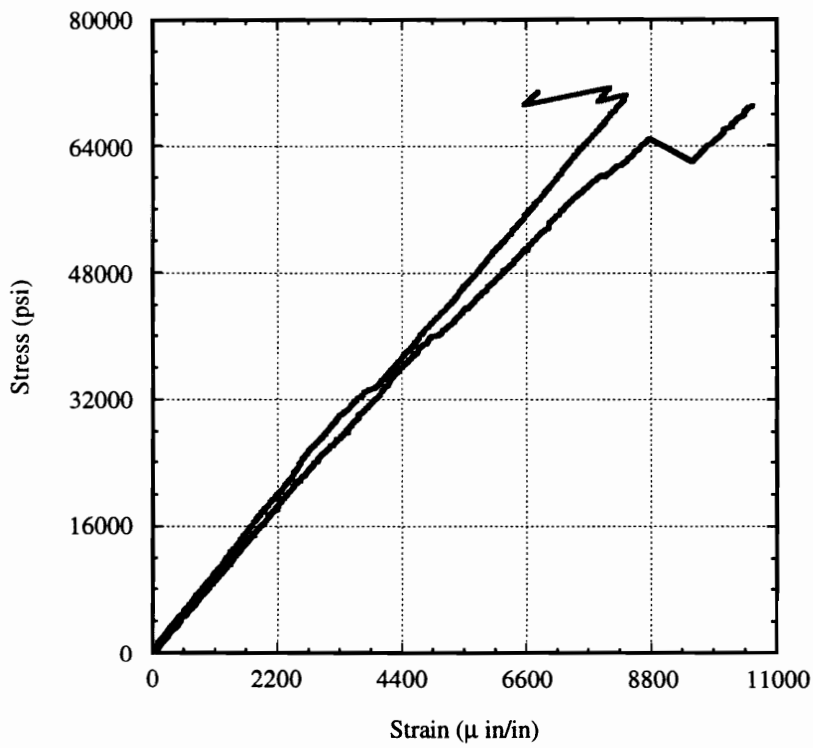
Figure 3.10 - Stress vs. Strain Response for Two LLL Architecture Specimens Tested to Ultimate Failure
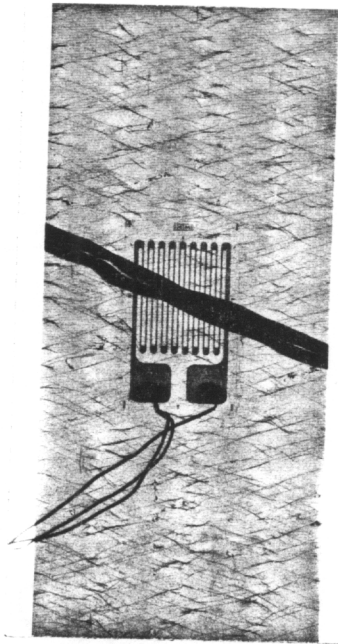
Figure 3.11 - Radiograph of a Static Tension Specimen from the LLL Architecture
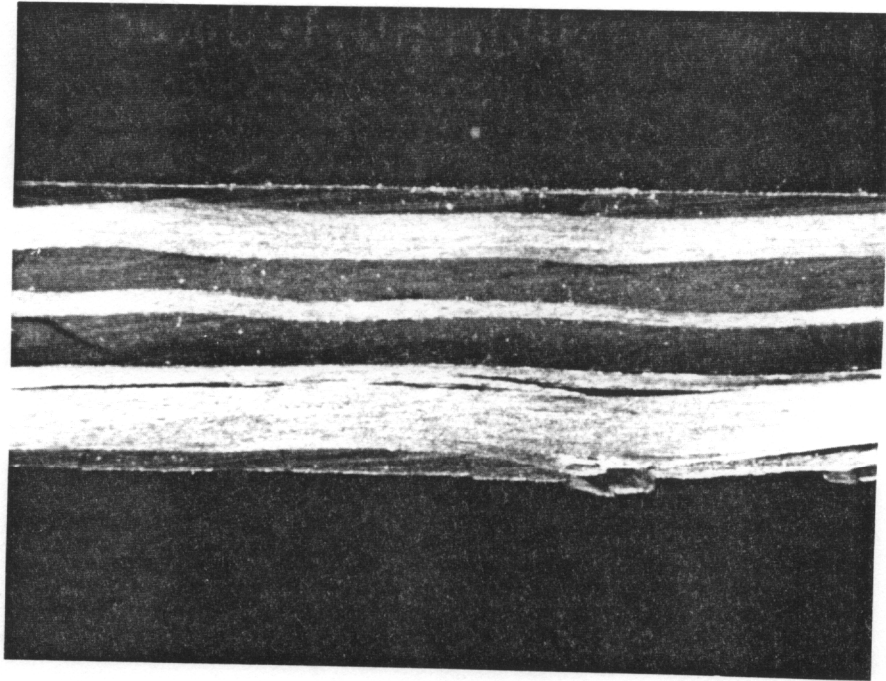
Figure 3.12 - Splitting in a Curved Region of an Axial Fiber Bundle in a Static
Tension Specimen from the LLL Architecture

level at which the split occurred was not known, as the damage mechanism was found already formed while scanning the edge of the specimen with the microscope during the test. The final failure mode was rupture of the axial fiber bundles.

3.4 Overall Conclusions

3.4.1 Effect of Axial Bundle Size (LSS vs. LLS)

The larger axial bundles in the LLS architecture yielded a higher strength and lower strain to failure as compared to the LSS architecture, which contained smaller axial fiber bundles. The LSS architecture was dominated by the 45° braider fiber bundles, which caused the material to behave much like an off-axis shear test, and yielded a higher strain to failure.

Splitting in curved regions of the axial fiber bundles along their length was found to occur in the LLS architecture. The splits were localized and did not extend into the adjacent straight regions of the axial fiber bundle.

The first damage mechanism to occur in both architectures was splitting of braider fiber bundles along their length. The final failure mechanism was rupture of the axial fiber bundles.

3.4.2 Effect of Architecture Scaling (SLL vs. LLL)

The SLL architecture had a higher ultimate strength, tensile modulus, and strain to failure than the larger scale LLL architecture. No specific damage mechanisms were found which contributed to this difference.

Splitting in the axial fiber bundles along their length was found in one SLL architecture specimen. The specimen was found to have a nested layer stacking sequence as compared to a specimen containing a stacked sequence in which splitting in the axial fiber bundles was not found.

Splitting in a curved region of an axial fiber bundle was found in the LLL architecture. The splits were localized and did not extend into the adjacent straight regions of the axial fiber bundle.

The first damage mechanism to occur in both architectures was splitting of the braider fiber bundles along their length. The final failure mechanism was rupture of the axial fiber bundles.

4. Static Compression Testing

Static compression testing was completed in order that damage types and sequences could be established and understood as a precursor to compression-compression fatigue testing. This chapter presents experimental results from static compression testing of the four braided architectures initially presented.

4.1 Test Configuration Selection

Several different types of test fixtures are available for compression testing of composite materials. Selection of a specific test fixture requires knowledge of the type of composite that will be tested, as well as the desired method of compression loading. Compression loads can be introduced through either shear loading, end loading, or a combination of the two. Berg and Adams [72] found that the IITRI compression fixture produced the highest ultimate strengths and lowest scatter in moduli as compared to the Celanese and end-loaded side-supported fixtures. In a related work, Adams and Odom [73] studied the effects of steel and glass-fabric tabs. The glass-fabric was found to be a

good tabbing material, as it required less fabrication than the steel while still yielding comparable results. Because of this research, the IITRI compression fixture described in [74] was chosen for use in the present study. It provided the best test configuration while accommodating larger specimen sizes needed for the braided architectures. Glass-fabric tabs were used for all specimens in the present research.

4.2 Test Specimen Fabrication

Specimen fabrication was initiated by cutting a 5.5 inch by 5.5 inch plaque from the main braided composite panel with a water cooled diamond blade saw. Surfaces of the plaque were dried and cleaned with acetone to remove any residual films. One-sixteenth inch thick glass-fabric tabs were then placed on one side of the plaque using ScotchWeld™ DP-460 epoxy adhesive. The epoxy was applied to the region where the tabs were to be bonded. Small copper wires (0.009 inch dia.) were then placed in evenly spaced intervals in the epoxy as shown in Figure 4.1. The tabs were then placed on each end of the same side of the plaque divided by a 0.5 inch wide by 5.5 inch long teflon spacer. The bottom edges of the spacer were chamfered to produce a 45° slope from the edge of the tab to the surface of the plaque, while the 0.5 inch width produced the desired gage length. Even pressure was then applied to the tabs and teflon spacer, and excess epoxy was forced out around the outside edges of the plaque. The tabs eventually came to rest on the embedded wires producing an even epoxy layer approximately 0.009 inch thick, which was the recommended thickness for maximum shear strength from the

Top View

0.009" dia. wires
(between tab and plaque)

5.5" x 5.5" plaque

tab

epoxy (45° chamfer)

plaque

Edge View
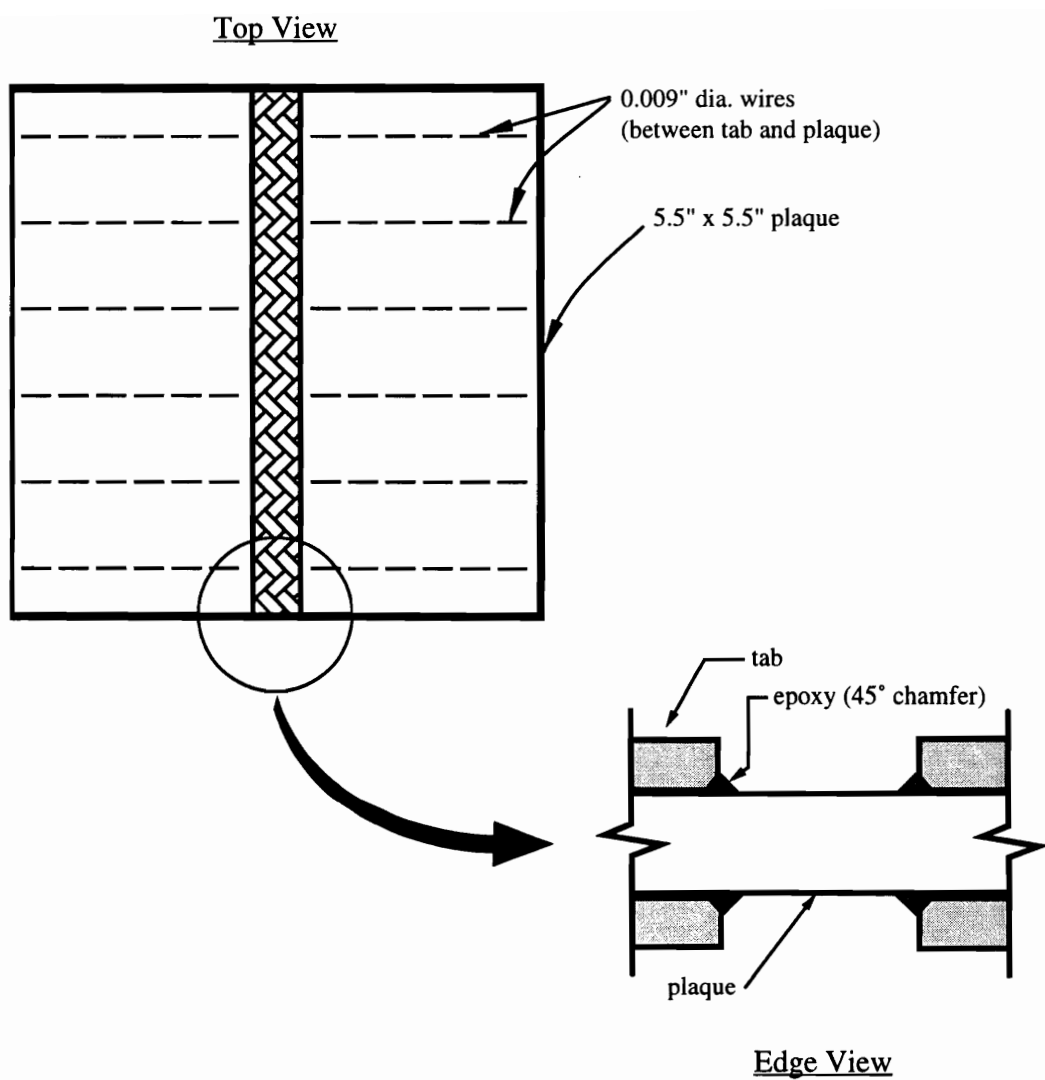
Figure 4.1 - Compression Specimen Fabrication Details
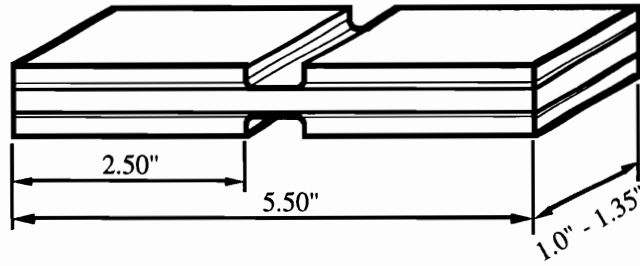
Figure 4.2 - Dimensions for IITRI Compression Specimens

manufacturer. Once the tabs were bonded to the first side, the outer surfaces of the tabs

were machined so that they were parallel to the opposite surface of the plaque.The second

side of the plaque was then tabbed in the same manner as the first side. Once the tabs were

securely bonded onto the second side, the outer surface of the tabs was machined such that

it was parallel to and the same thickness as the outer surface of the tabs on the opposite

side of the plaque . This prevented asymmetric loading effects produced by an uneven

specimen geometry. All specimens had a gage length of 0.5 inches as shown in Figure 4.2.

The gage width was 1.0 inches for all except the LLL architecture which had a gage width

of 1.35 inches due to its larger unit cell width.

4.3 Experimental Program

The compression testing program consisted of two groups of straight sided specimens from each architecture. The first three coupons from each architecture were tested to failure to determine material properties and general stress-strain responses. The final two coupons (one for the LLL architecture) were tested to load levels as close to ultimate failure as possible without global failure of the coupon, then sectioned and studied to determine damage types and failure mechanisms. The edges of all specimens were monitored during the test with a stereo microscope. Strain was monitored on the front and back faces of the specimens using 0.25 inch by 0.25 inch strain gages (PA-06-250 GK-120). These strain gages were chosen because the soldering tabs were placed on the sides of the gage section instead of below it, which allowed a larger gage to be placed on the 0.5 inch gage length of the coupons. All tests were run under stroke control at a rate of 0.01 inch/minute on a 20 kip screw-driven load frame. The upper half of the IITRI fixture was threaded onto the main post of the load frame, while the lower half rested on the bottom platen of the load frame.

4.4 Discussion of Results

4.4.1 $[0_{6K}/\pm45_{15K}]_{12\% \, axial}$ (LSS) Architecture

Stress-strain curves for the three specimens from the LSS architecture tested to ultimate failure are shown in Figure 4.3, with results listed in Table 4.1.

Table 4.1 : Measured Compression Properties for the LSS Architecture

Specimen #	Elastic Modulus (Msi)	Ultimate Strength (ksi)	Ultimate Strain (%)
1	4.63	51.8	1.48
2	4.72	56.2	1.81
3	4.6	45.5	1.40
avg. ± std. dev.	4.70±0.15	51.7±5.4	1.56±0.22
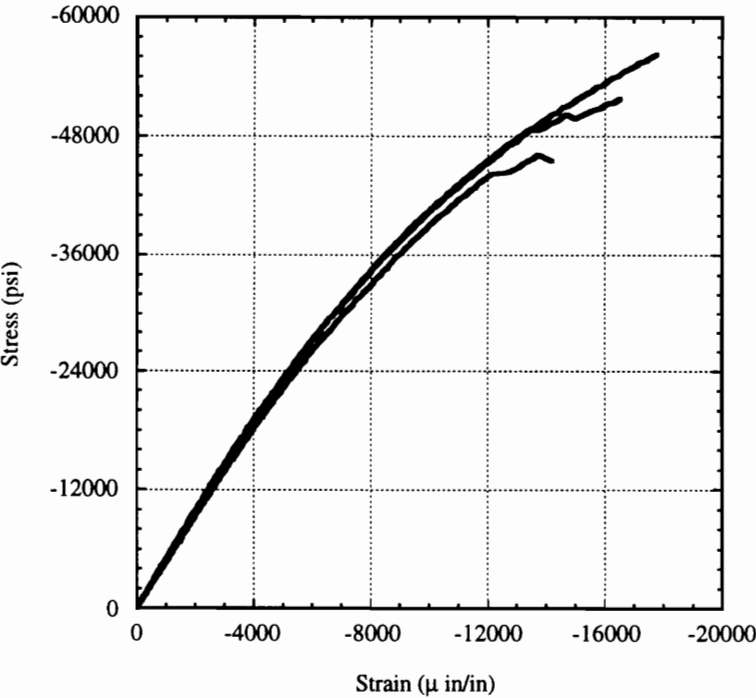
Figure 4.3 - Compression Stress-Strain Response from Three LSS Architecture Specimens Tested to Ultimate Failure

This architecture exhibited the most nonlinear stress-strain response, lowest longitudinal modulus, lowest strength, and highest strain to failure of the four architectures tested. This is due to the high percentage of braider bundles oriented at ±45° to the loading axis. Because this architecture contains only 12% axial bundles, the overall behavior was dominated by the characteristics of the braider bundles. With 88% of the total composite being oriented at ±45° to the loading axis, the test simulated an off-axis shear test, thus producing a nonlinear stress-strain response, high strain to failure, and lower longitudinal modulus. The 75% reduction in axial bundle content as compared to the other three architectures also significantly reduces the elastic properties in the axial direction of the LSS architecture.

Sectioning of the two specimens tested to load levels just prior to ultimate failure showed cracking in resin rich areas to be the initial failure mode, as is seen in Figure 4.4. These cracks are oriented at angles of approximately 45° to the loading axis, which runs along a horizontal line in the micrograph. No damage in the axial bundles was found in the specimens tested to pre-ultimate failure load levels. Scanning electron microscopy of the post-failure specimens revealed two modes of failure in the axial bundles. The first mode involves splitting of the axial fiber bundle along its length as shown in Figure 4.5. The axial bundle is not severed. The second mode involves shearing of the axial bundle on a plane following the longitudinal axis of a braider bundle as seen in Figure 4.6. No evidence of kink band formation was found in the post-failure specimens.
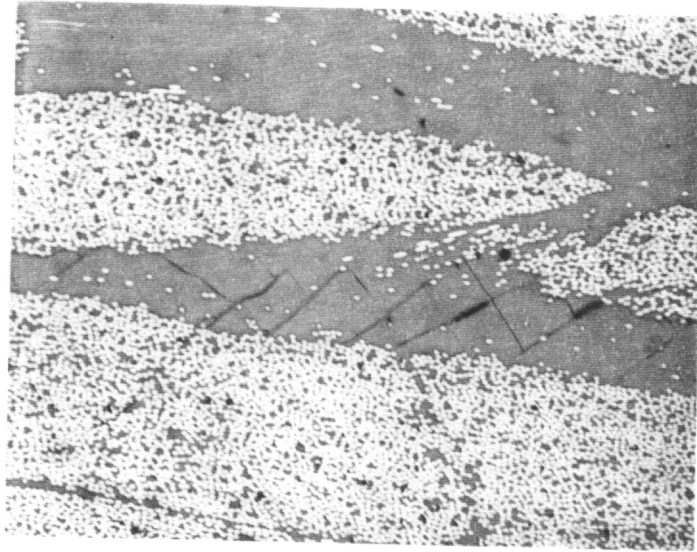
Figure 4.4 - Pre-Ultimate Failure Matrix Cracking in LSS Architecture Subject to Static Compression Loading
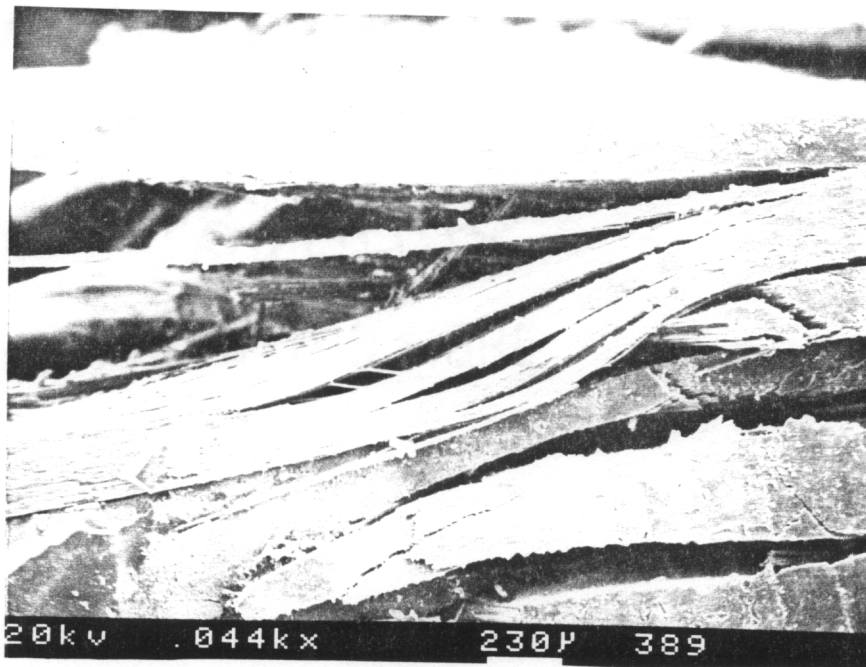
Figure 4.5 - Splitting in the Axial Fiber Bundle of a Post-Failure Specimen from the LSS Architecture
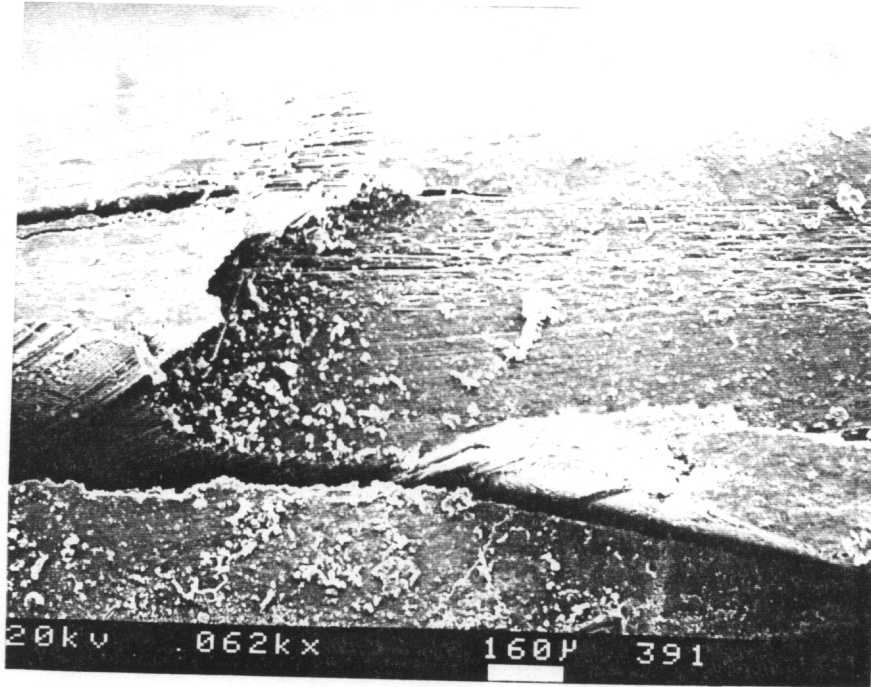
Figure 4.6 - Shearing of an Axial Fiber Bundle in a Post-Failure Specimen from the LSS Architecture

4.4.2 $[0_{36K}/\pm45_{15K}]_{46\% \; axial}$ (LLS) Architecture

Stress-strain curves for the three specimens from the LLS architecture tested to ultimate failure are shown in Figure 4.7 with results listed in Table 4.2. This architecture exhibited a mostly linear stress-strain response along with the highest longitudinal modulus, the highest strength, and the second highest strain to failure of the four architectures tested. The increase of axial bundle size yielded a higher longitudinal modulus, higher ultimate strength, and lower strain to failure as compared to the LSS architecture.

Table 4.2 : Measured Compression Properties for the LLS Architecture

Specimen #	Elastic Modulus (Msi)	Ultimate Strength (ksi)	Ultimate Strain (%)
1	9.82	89.7	1.04
2	10.12	92.5	1.06
3	10.33	87.7	0.98
avg. ± std. dev.	10.1±0.30	90.0±2.4	1.03±0.04
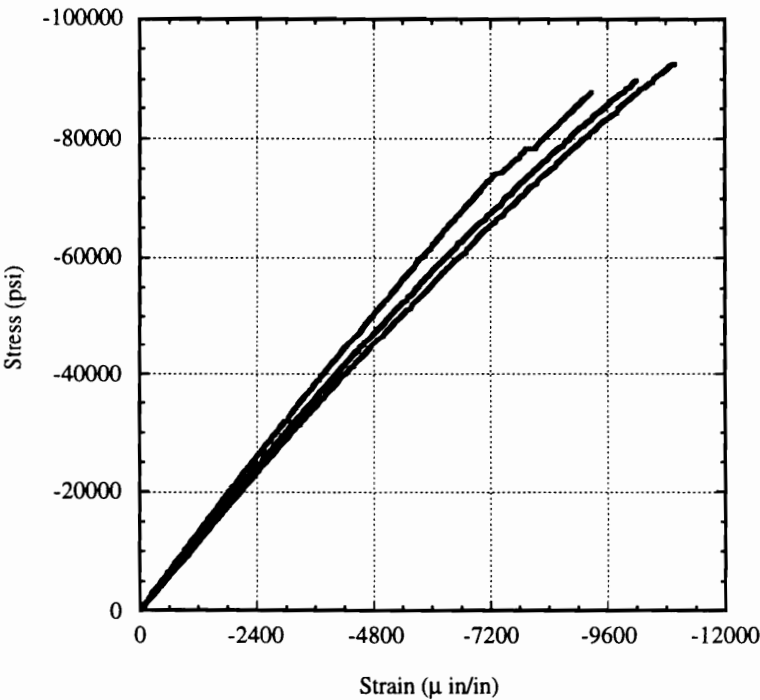
Figure 4.7 - Compression Stress-Strain Response from Three LLS Architecture Specimens Tested to Ultimate Failure
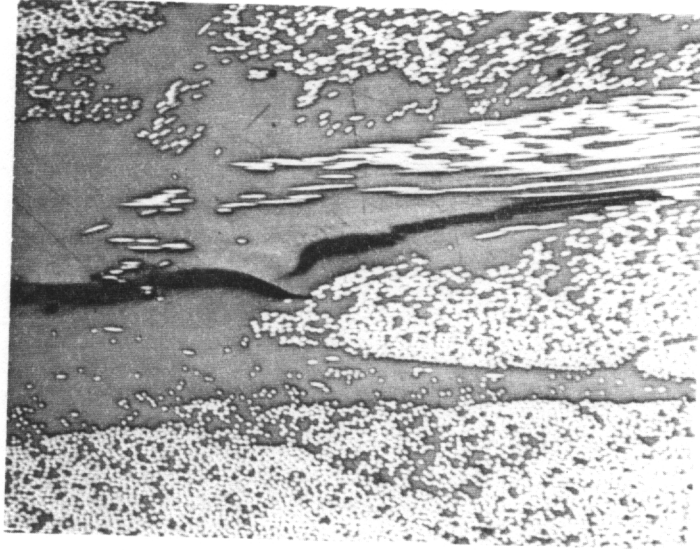
Figure 4.8 - Pre-Ultimate Failure Matrix Cracking in the LLS Architecture Subject to Static Compression Loading

Sectioning of the two specimens tested to load levels just prior to ultimate failure showed cracking in resin rich areas to be the initial failure mode, as seen in Figure 4.8. This matrix cracking is different than the matrix cracking found in the LSS architecture in that it does not occur at angles of ±45° to the loading axis, which is along a horizontal line in the micrograph. The cracks are larger, and appear to be opened more than the cracks found in the LSS architecture. Study of the post-failure specimens showed evidence of kink band formation and splitting in the axial fiber bundles, as seen in Figure 4.9. Remains of a kink band are loosely attached to the end of an axial fiber bundle. The fiber bundle also contains a crack which extends into the bundle along its length. These damage mechanisms were found in several locations in the failed specimens.
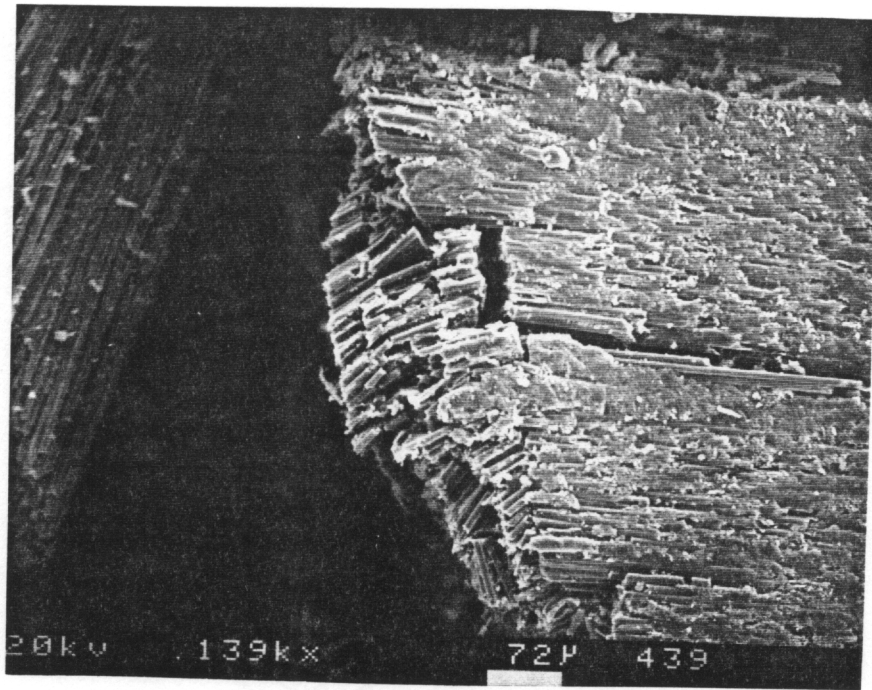
Figure 4.9 - Post Failure Kink Band Remains and Splitting of an Axial Fiber Bundle in the LLS Architecture (edge view)

4.4.3 $[0_{30K}/\pm70_{6K}]_{46\% \, axial}$ (SLL) Architecture

Stress-strain curves for the three specimens from the SLL architecture tested to failure are shown in Figure 4.10, with results listed in Table 4.3. The stress-strain response from this architecture was nearly linear, showing only a slight decrease in longitudinal stiffness with increasing applied stress. The SLL architecture had the second highest strength and longitudinal modulus, and the third highest strain to failure of the four architectures tested. As compared to the LLS architecture which had the same overall percentage of axial fiber bundles, the change in braider bundle angle from 45° to 70° yielded reduced longitudinal modulus, strength, and strain to failure.

Table 4.3 : Measured Compression Properties for the SLL Architecture

Specimen #	Elastic Modulus (Msi)	Ultimate Strength (ksi)	Ultimate Strain (%)
1	9.0	79.8	0.96
2	8.95	71.2	0.82
3	9.02	67.6	0.81
avg. ± std. dev.	9.0±0.04	72.9±6.3	0.86±0.08
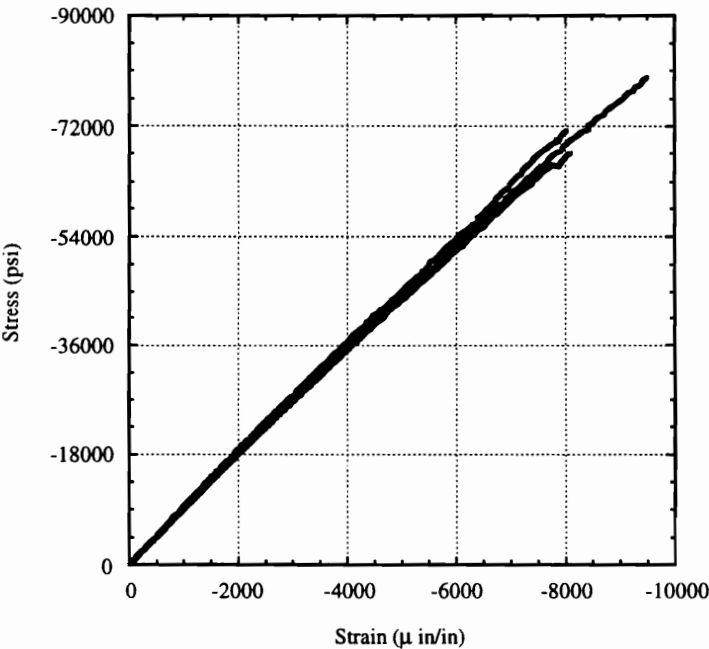
Figure 4.10 - Compression Stress-Strain Response from Three SLL Architecture Specimens Tested to Ultimate Failure
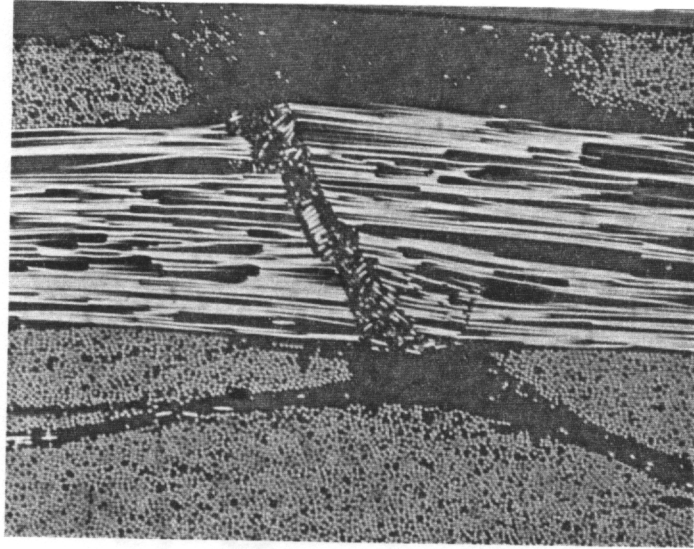
Figure 4.11 - Kink Band Formation in an Axial Fiber Bundle in the SLL Architecture
Prior to Ultimate Failure (edge view)

Sectioning of the two specimens tested to levels just prior to ultimate failure revealed the formation of kink bands in axial fiber bundles, as shown in Figure 4.11. No cracking in the resin rich areas was found to exist. Study of the post-failure specimens also showed remains of kink band formation as seen in Figure 4.12. Splitting of the axial bundle along its length was also found in any bundles which contained remains of kink bands.

4.4.4 $[0_{75K}/\pm70_{15K}]_{46\% \, axial}$ (LLL) Architecture

Stress-strain curves for the three specimens from the LLL architecture tested to ultimate failure are shown in Figure 4.13 with results listed in Table 4.4.
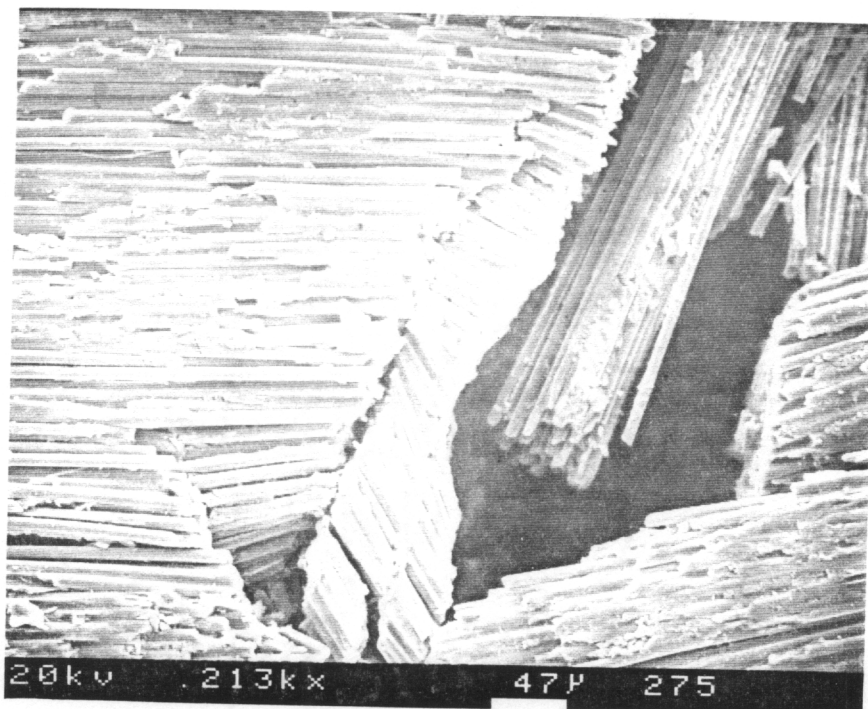
Figure 4.12 - Post Failure Kink Band Remains in an Axial Fiber Bundle in the SLL Architecture (edge view)
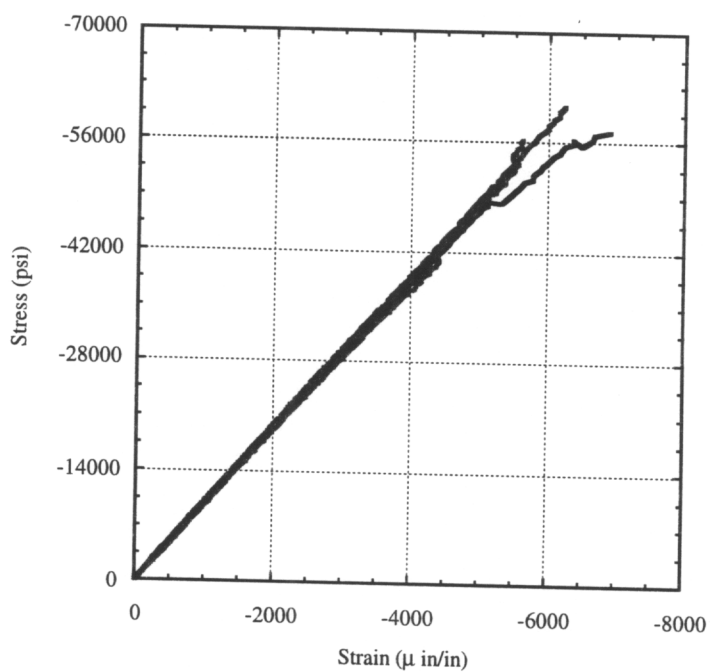
Figure 4.13 - Compression Stress-Strain Response from Three LLL Architecture Specimens Tested to Ultimate Failure

Table 4.4 : Measured Compression Properties for the LLL Architecture

Specimen #	Elastic Modulus (Msi)	Ultimate Strength (ksi)	Ultimate Strain (%)
1	9.17	61.6	0.69
2	9.45	71.9	0.93
3	8.86	57.3	0.68
avg. ± std. dev.	9.16±0.30	63.6±7.5	0.77±0.14

This architecture behaved in much the same manner as the SLL architecture, with slightly lower average values for strength, longitudinal modulus, and strain to failure. The standard deviations for each of the measurements are large enough, however, that related measurements from the two architectures can not be distinguished from a statistical standpoint. This is due to the fact that the LLL architecture is an exact scale-up of the SLL architecture, with the axial bundles being five times larger than the braider bundles in both architectures.

Study of the specimen tested to a load level just prior to failure revealed no detectable damage, as shown in Figure 4.14. Two axial fiber bundles span the micrograph horizontally. Dark lines in the regions surrounding the axial fiber bundles represent boundaries between individual braider fiber bundles. Study of the post-failure specimens showed the characteristic kink band formation and axial bundle splitting as was found in both the LLS and SLL architectures (Figure 4.15).
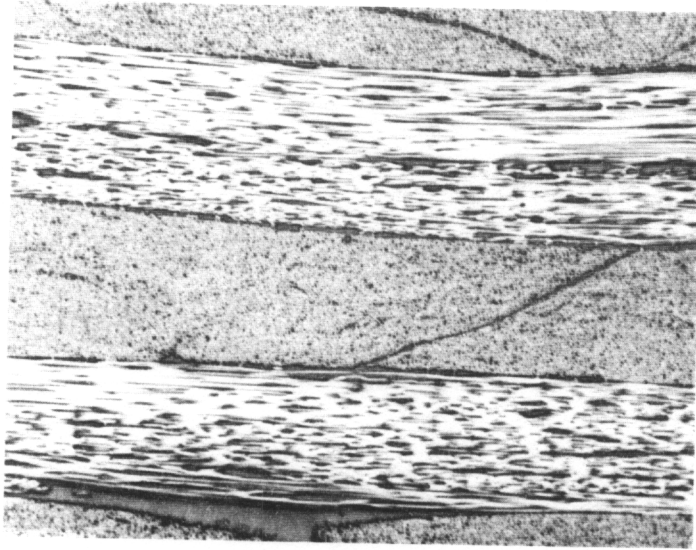
Figure 4.14 - Pre-Ultimate Failure Micrograph of LLL Architecture (edge view)
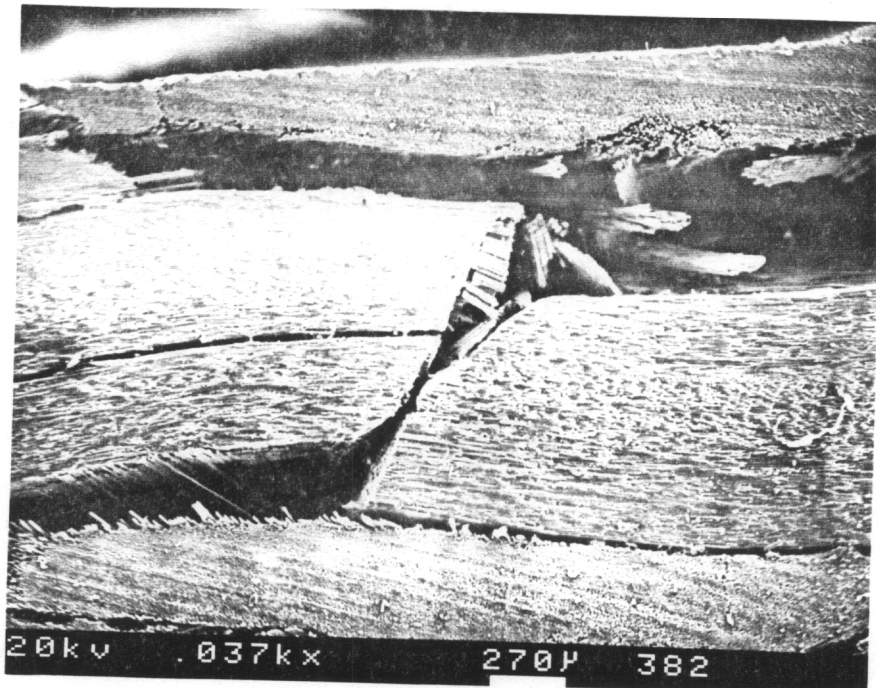
Figure 4.15 - Post Failure Kink Band Remains in an Axial Fiber Bundle in the LLL Architecture (edge view)

4.5 Overall Conclusions

4.5.1 Effect of Axial Bundle Size (LSS vs. LLS)

Increasing the axial bundle size by a factor of six produced several noticeable effects. The LLS had significantly higher ultimate strength and longitudinal modulus, while the smaller LSS architecture had a much larger strain to failure. These are all effects that would be expected by increasing the percentage of 0° plys in a $(0/\pm45)_s$ laminate while keeping the thickness constant.

Both architectures had matrix cracking in resin rich areas as initial failure modes. Based on post-failure analysis, final failure modes differed. The smaller axial bundles of the LSS architecture appear to have been sheared off by the braider bundles and displaced laterally. The larger bundles of the LLS architecture showed remains of kink band formation in post-failure analysis.

It is postulated that the final failure mode in the LSS architecture is shearing of the axial bundles along the centerlines of braider bundles, while in the LLS architecture, kink band formation immediately prior to ultimate failure is the final failure mode.

4.5.2 Effect of Architecture Scaling (SLL vs. LLL)

The effect of scaling the architecture was insignificant under static compression loading. While average measured values for ultimate strength, strain to failure, and

longitudinal modulus were slightly lower for the LLL architecture as compared to the SLL architecture, standard deviations for comparable measurements were large enough to invalidate any distinction between the response of the two architectures.

Damage mechanisms were comparable in both architectures. Although kink band formation was not found in the pre-ultimate failure specimen from the LLL architecture, post-failure analysis proved they were in existence.

It is postulated that the final failure mechanism immediately before ultimate failure in the LLL architecture is kink band formation in the axial bundles, as was the case in the SLL architecture. The close proximity of kink band formation and ultimate failure makes it very difficult to stop the test before ultimate failure occurs.

5. Tension Fatigue Testing

Tension-tension fatigue testing was completed on three of the four architectures presented in this study. A first group of specimens was tested to failure to determine the characteristic fatigue response of each architecture. A second and third group of specimens were tested to predetermined damage states at low and high stress levels in order to destructively evaluate damage types and mechanisms. This chapter presents the experimental results from the tension-tension fatigue testing program.

5.1 Test Specimen Fabrication

Individual specimens were cut from the main panel using a water cooled diamond blade saw to the dimensions shown in Figure 5.16. All specimens had a 4.0 inch gage length, with 1.875 inches in each of the hydraulic grips of the load frame. Specimens were 1.0 inch wide for each architecture, with the exception of the LLL architecture which had a gage width of 1.5 inches to accommodate the larger unit cell size. If the edge of the specimen was not smooth enough for microscopic viewing after the saw cut had been
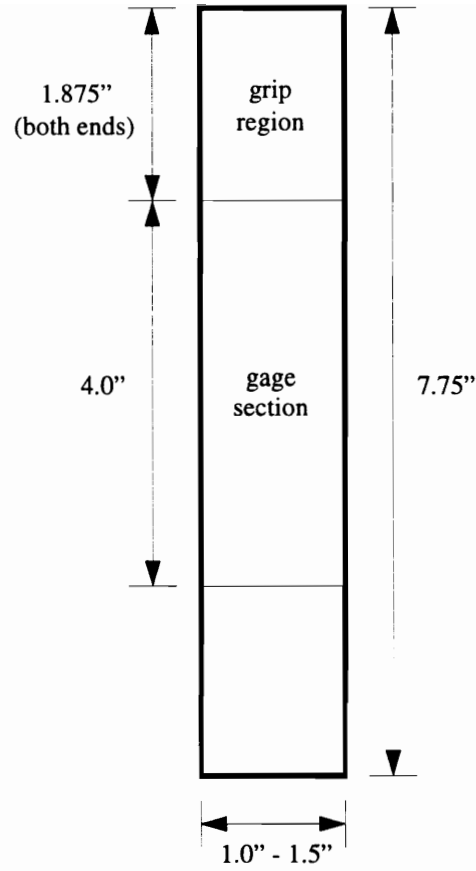
Figure 5.16 - Tension-Tension Fatigue Specimen Dimensions

completed, the edge was polished using a micropolish cloth impregnated with 0.05 micron alumina paste. This was done on a motorized polishing wheel in order to keep the polished edge flat. Aluminum extensometer tabs were adhered to the face of the specimen using silicone glue. The tabs were placed such that the center of the extensometer gage length would rest at the geometric center of the gage section face when the feet of the extensometer were placed in the aluminum tabs. Circular notches were drilled in selected specimens at the NASA Langley Research Center using an ultrasonic drill.

5.2 Experimental Program

Four specimens from each architecture were tested to failure at different stress levels to determine an approximate S-N response. From this data, two stress levels which would produce a specimen life of approximately 25,000 cycles and 90,000 cycles were determined. This corresponded to test durations of approximately 1.3 hours and 5 hours respectively. Six specimens from each architecture were tested at the lower stress level, and six were tested at the higher stress level. Of the six specimens, three were notched and three were unnotched. Notched tension-tension fatigue specimens were tested at the same net stress levels as were the unnotched specimens. All notched specimens contained a circular hole located at the geometric center of the gage area. The hole diameter was 0.25 times the gage width of the specimen. The peak applied load for the notched specimens was determined by multiplying the peak applied stress level for the unnotched specimens by the reduced cross-sectional area at the center of the notched gage section, perpendicular

to the direction of loading. This consistency of peak applied net-section stress provided the capability of evaluating the response of each architecture subjected to a stress concentration. Each group of three specimens at each loading condition was tested to specific levels defined by either a predetermined stiffness loss or cycle number, each of which was less than ultimate failure. The goal was to test the three specimens in each group to an initial, intermediate, and advanced state of damage. Tested specimens were impregnated with a zinc-iodide solution and x-rayed. From the x-ray information, damaged areas in the gage section were identified, and the sections were cut such that the damaged areas would be exposed in the sample. The cut sections were then cast in epoxy resin and polished for microscopic viewing and study. All specimen samples were cut using a water-cooled diamond blade saw.

All tests were completed on a servo-hydraulic test frame at a rate of 5 Hz, and a minimum/maximum stress ratio of 0.1. Tests were run under load control using a haversine input signal. Strain was monitored with a 1.0 inch extensometer mounted on the face of the specimen. The feet of the extensometer were placed on grooved aluminium pads which were 0.25 inches wide by 0.125 inches tall. Each leg of the extensometer was held in place by attaching a rubber band to one side of the extensometer foot, wrapping the band around the back side of the specimen, and attaching it to the opposite side of the extensometer foot.

5.3 Discussion of Results

5.3.1 $[0_{6K}/\pm45_{15K}]_{12\% \, axial}$ (LSS) Architecture

Unnotched - The peak stress versus life plot for the four specimens tested to failure from the LSS architecture is shown in Figure 5.17, along with straight-line log-linear fit of the data points. This data set was used to determine high and low stress levels for the second phase of testing, which were 35.4 ksi and 32.8 ksi respectively. Due to the limited number of data points, only the two values of peak applied stress were extracted from this information. No other conclusions were inferred.

Two parameters are frequently discussed in this chapter with respect to results from fatigue testing. The dynamic tangent modulus is defined as the the modulus calculated via a linear regression on the upslope of the fatigue loading cycle. The "dynamic" qualifier is used to denote that the modulus is calculated from a dynamic fatigue loading cycle, *not* from a quasi-static loading cycle. The hysteresis energy is defined as the area inside the stress-strain curve of an individual loading cycle. Measurement of both parameters is described in Appendix A.

No differences in dynamic tangent modulus and hysteresis energy versus cycle number information were found when comparing specimens tested at the low stress level to those tested at the high stress level for the LSS architecture. Also, no differences were

Figure 5.17 - Peak Stress vs. Life Plot for Four Tension-Tension Fatigue Specimens
from the LSS Architecture

found in the type and order of occurrence of damage mechanisms. Therefore, the following section presents a characteristic initial damage state, and a characteristic progressed damage state for the unnotched specimens from the LSS architecture.

A characteristic micrograph and corresponding dynamic tangent modulus and hysteresis energy information versus cycle number graph for a specimen containing an initial state of damage is shown in Figure 5.18. Hysteresis energy values from the first cycle were typically two to three times greater than subsequent cycles. This was attributed to cracking in the resin rich pockets and splitting in the braider bundles, a large portion of which took place on the first loading cycle. Cracks in the resin rich pockets and splits in the braider fiber bundles can be seen in the micrograph of Figure 5.18. Cracks are represented by thin dark lines oriented vertically in the micrograph. As the test progressed, large damage events which produced audible noise showed up as spikes in the hysteresis energy graph. These events caused an instantaneous fluctuation in the extensometer significant enough to produce large spikes in the hysteresis energy information. By monitoring the edge of the specimen with a stereo microscope during the test, correlations were made between these spikes in the hysteresis energy information and observed damage mechanisms. Cracks in the resin rich pockets and splits in the braider bundles both caused spikes in the hysteresis energy information. It should be noted however, that not all damage events were detected by the extensometer. Some damage events which occurred at locations in the gage section away from the extensometer did not release

Figure 5.18 - Micrograph and Corresponding Dynamic Tangent Modulus and Hysteresis Energy Information vs. Cycle Number for an Unnotched Specimen from the LSS Architecture Containing an Initial Damage State

enough energy to disturb the extensometer, and were thus undetected by the extensometer. This holds true for all specimens reported in this chapter.

A micrograph from a specimen containing a progressed state of damage is shown in Figure 5.19, along with the corresponding dynamic tangent modulus and hysteresis energy versus cycle number information. In the progressed damage state, cracks in the resin rich areas and splits in the braider fiber bundles were found, along with disbonding of the axial fiber bundles from their surrounding constituents. One large energy event was detected near the end of the test. The dynamic tangent modulus decreased as the number of test cycles increased.

Overall, cracks in the resin rich areas and splitting in the braider bundles occurred first, followed by disbonding of the axial bundles from their surrounding constituents. As the number of test cycles increased, the dynamic tangent modulus decreased. Hysteresis energy events were detected by the extensometer, however, some audible damage events were not detected due to their occurrence well away from the location of the extensometer.

Notched - The following section presents the test results of notched specimens from the LSS architecture. Levels of initial and progressed damage will not be presented, as the notched specimens behaved in a different manner than the unnotched specimens. Two of the six specimens tested displayed characteristics consistent with those found for the unnotched specimens, and happened to be the first two specimens tested from the group.

Figure 5.19 - Micrograph and Corresponding Dynamic Tangent Modulus and
Hysteresis Energy Information vs. Cycle Number for an Unnotched Specimen from
the LSS Architecture Containing a Progressed Damage State

The four following specimens degraded at extremely high rates as compared to the first two, and thus all contained very progressed levels of damage. This behavior was associated with stacking patterns, as described in the following section. Because of this behavior, the order of initial and progressed damage states presented in the unnotched specimen description will not be presented. Discussion will be focussed on dynamic tangent modulus versus cycle number information, along with the internal architecture of the individual specimens.

Normalized dynamic tangent modulus versus cycle number information for the three specimens tested at the low stress level are shown in Figure 5.20. The dynamic tangent modulus value of each test was normalized by its initial value to make a consistent comparison between the three specimens. The label of each test is placed on the graph at the location where the respective test was stopped. The first two specimens tested (1 and 2) displayed very consistent results. The rate of dynamic stiffness decrease for the two specimens were nearly identical. As the number of test cycles increased, the overall dynamic stiffness decreased. The third specimen tested exhibited a much higher rate of dynamic stiffness loss. The test was stopped just prior to ultimate failure of the specimen. Again, as the number of test cycles increased, the dynamic stiffness decreased, but at a much higher rate than in specimens 1 and 2. Characterization of the architectural microstructure of each specimen is also shown in Figure 5.20. The view shown is of a cross-section taken through the center of the notch, perpendicular to the line of loading.
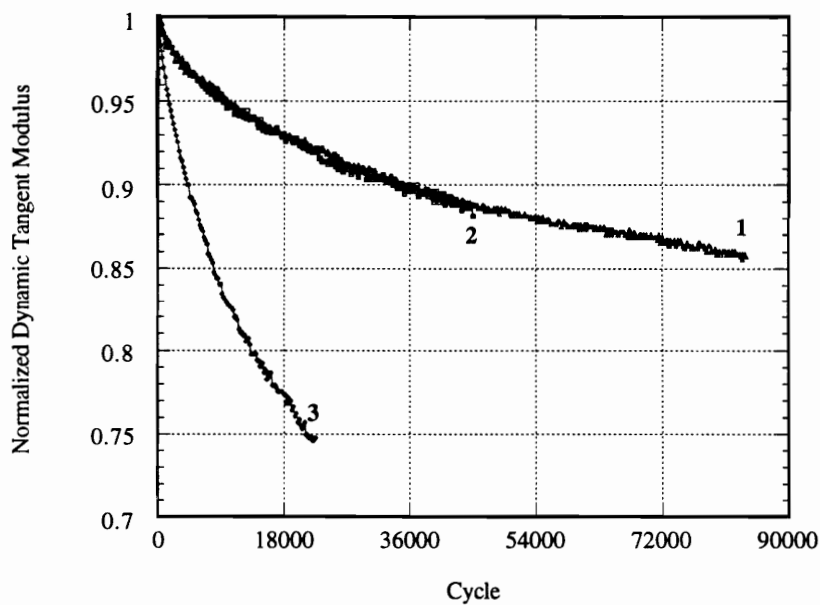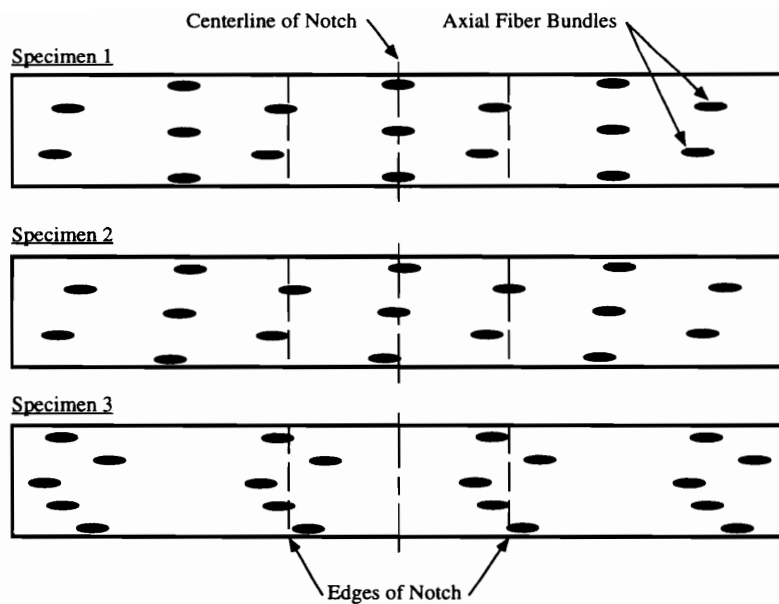
Figure 5.20 - Normalized Dynamic Tangent Modulus Information for Three Notched Specimens from the LSS Architecture Tested at the Low Stress Level, along with Axial Fiber Bundle Locations in the Specimen Cross-Section

The ellipses are cross sections of the axial fiber bundles, which extend into the page along the line of loading. The vertical line in the center of each schematic corresponds to the center of the notch, while the dashed lines represent the edges of the notch. As can be seen in the figure, specimens one and two contain a stacking sequence where by the axial bundles in one layer lie between the axial bundles of the layers above and below the respective layer. This is termed a "nested" configuration. It is also important to note that the horizontal spacing of the axial fiber bundles in the LSS architecture was 0.5 inches, as was the diameter of the notch. In specimens one and two, two of the five individual layers had axial fiber bundles along either side of the notch, and three of the layers had axial fiber bundles which terminated at the top and bottom of the notch. In specimen three, a much different stacking sequence was found. The axial fiber bundles were more closely stacked in the through-thickness direction. All five layers had axial fiber bundles near the edge of the notch. This "stacked" axial fiber bundle configuration and concentration of axial fiber bundles near the edge of the notch corresponded to a high rate of dynamic stiffness loss as compared to the specimens containing a "nested" sequence, in which only two of the five individual layers had axial fiber bundles adjacent to the edge of the notch.

Normalized dynamic tangent modulus versus cycle number information for the three specimens tested at the high net section stress level are shown in Figure 5.21, along with the corresponding internal architectural schematic for each specimen. Three different rates of dynamic stiffness loss were found. The lowest rate of stiffness loss was found in
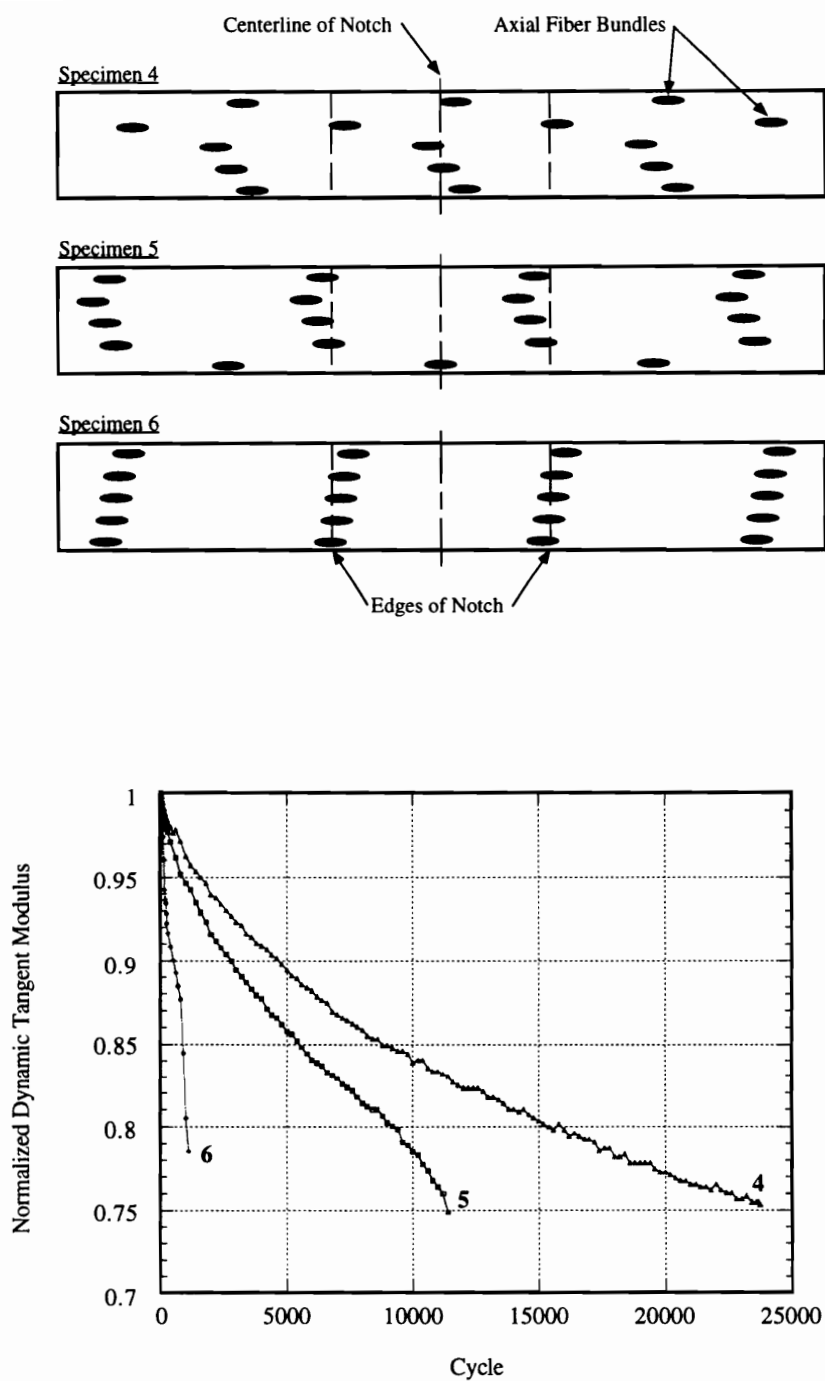
Figure 5.21 - Normalized Dynamic Tangent Modulus Information for Three Notched Specimens from the LSS Architecture Tested at the High Stress Level, along with Axial Fiber Bundle Locations in the Specimen Cross-Section

specimen four. One layer had axial fiber bundles adjacent to the edge of the notch, while the other four layers had axial fiber bundles which terminated at the top and bottom of the notch. Axial fiber bundles from four of the five layers were roughly aligned along a vertical line through the thickness of the specimen. Specimen five had a similar stacking sequence to specimen four, with the main difference of four of the five layers having axial fiber bundles adjacent to the edge of the notch. This specimen had a much higher rate of dynamic stiffness loss as compared to specimen four. The most severe case was seen in specimen six. All five layers had axial fiber bundles in a "stacked" configuration adjacent to the edge of the notch. The rate of the dynamic stiffness loss for specimen six was much greater than any of the other specimens. The test was stopped immediately prior to ultimate failure. In all three specimens, the dynamic stiffness decreased as the number of test cycles increased. Also, as the number of axial fiber bundles increased adjacent to the edge of the notch, the rate of dynamic stiffness increased.

Stacking patterns of the five layers in the LSS architecture were found to vary significantly in the six notched specimens. When the axial fiber bundles were aligned in a "nested" sequence with two of the five layers having axial fiber bundles adjacent to the edge of the notch, the rates of stiffness loss were much lower as compared to a specimen tested at the same load level with all five layers having axial fiber bundles near the edge of the notch. This was true for both the high and low net section stress levels. Because of the limited number of specimens tested, and the random nature of the specimen architectures,

only an indication of behavioral changes could be inferred. The effect of the "stacked" versus the "nested" axial bundles could not be separated from the effect of placing the bundles adjacent to the edge of the notch. It can be inferred from the six specimens, however, that the combination of stacking the axial fiber adjacent to the edge of the notch presents an extreme case with respect to increased rates of dynamic stiffness loss.

Hysteresis energy information for the notched specimens differed from the unnotched specimens. A characteristic dynamic tangent modulus and hysteresis energy versus cycle number graph displaying this behavior is shown in Figure 5.22. For the notched specimens, hysteresis energy values for the first cycle were typically three to four times greater than those for subsequent cycles. Also, the large hysteresis energy events with magnitudes of 15% or greater found in the unnotched specimens were *not* found in the notched specimens. In the notched tests, as the specimen reached advanced levels of damage, the mean value of the hysteresis energy would increase to levels two to three times that of the initial regions of the test. While only a limited number of specimens were available for testing, this behavior did indicate that the specimen was severely damaged and very near ultimate failure.

5.3.2 $[0_{36K}/\pm45_{15K}]_{46\% \, axial}$ (LLS) Architecture

Unnotched - The peak stress versus life plot for the four specimens tested to failure from the LLS architecture is shown in Figure 5.23, along with a straight-line log-linear fit
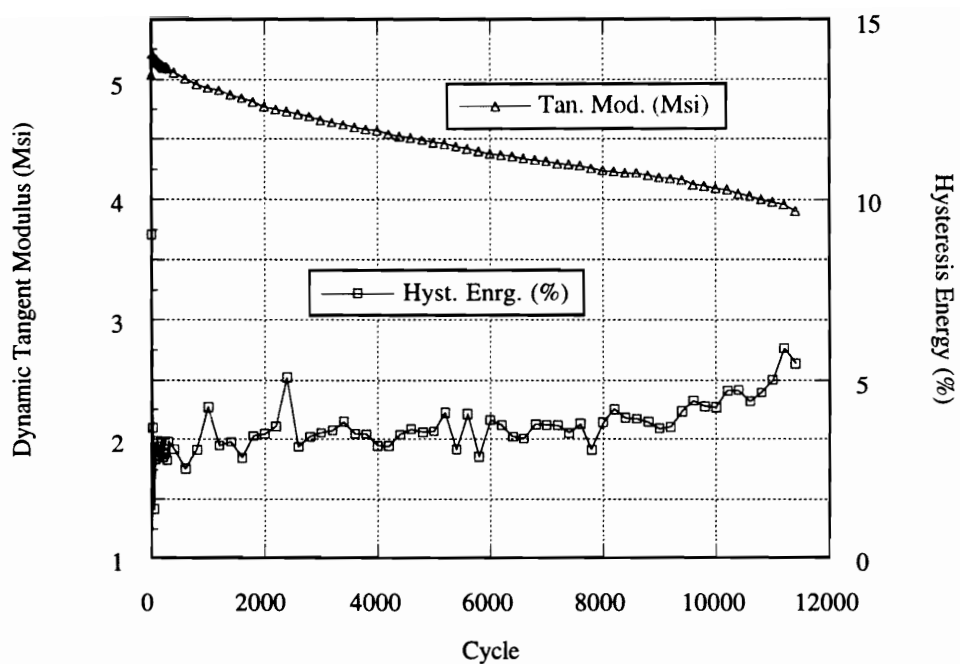
Figure 5.22 - Characteristic Dynamic Tangent Modulus and Hysteresis Energy Information vs. Cycle Number Graph for a Notched LSS Specimen with an Increasing Hysteresis Energy Trend
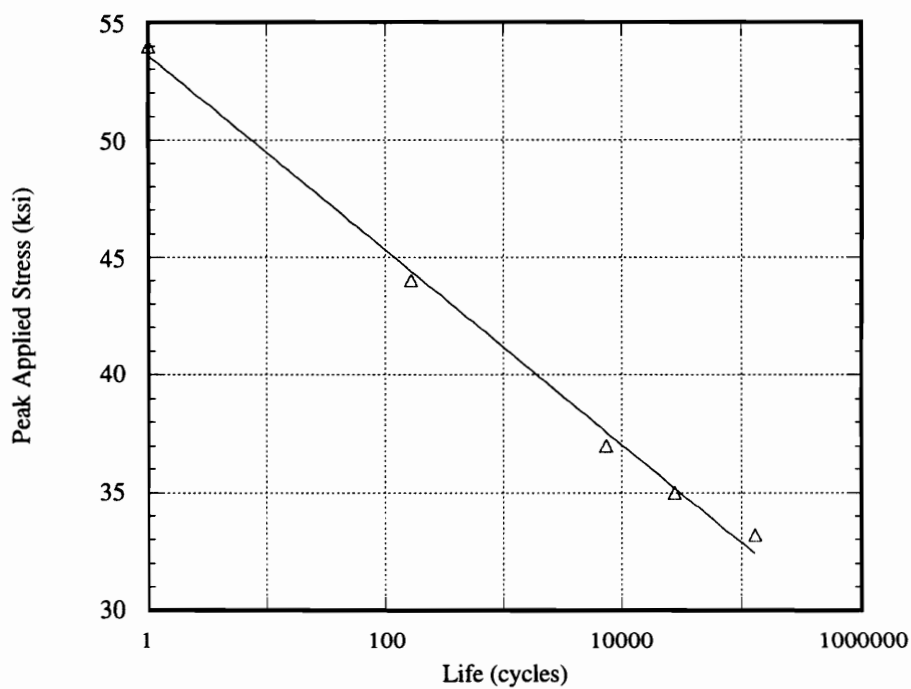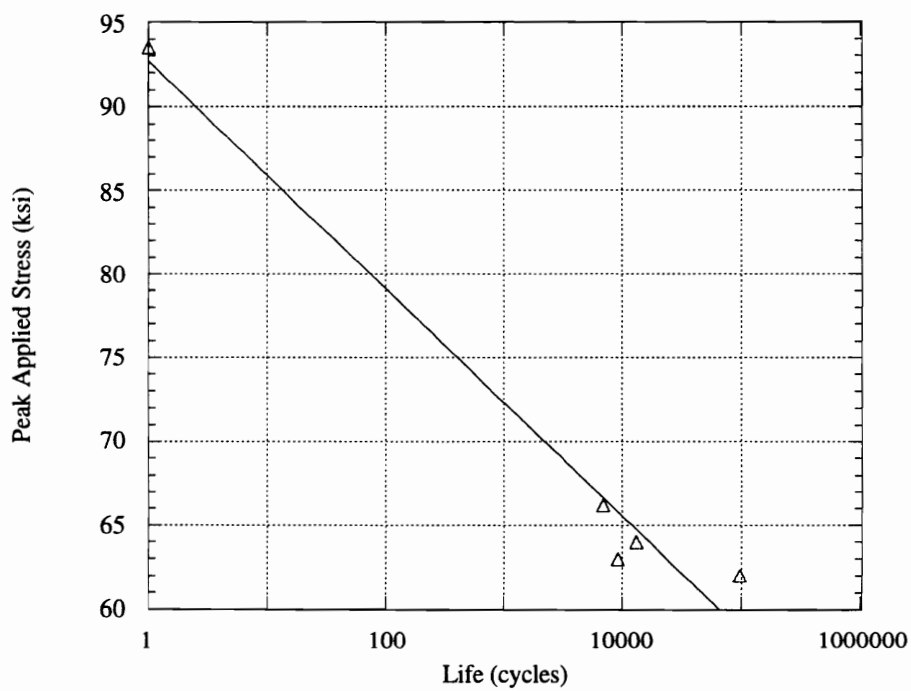
Figure 5.23 - Peak Stress vs. Life Plot for Four Tension-Tension Fatigue Specimens
from the LLS Architecture

of the data points. This data set was used to determine high and low stress levels for the second phase of testing, which were 63 ksi and 60 ksi respectively. Due to the limited number of data points, only the two values of peak applied stress were extracted from this information. No other conclusions were inferred.

No trends in dynamic tangent modulus and hysteresis energy versus cycle number information were found when comparing unnotched specimens tested at the low stress level to those tested at the high stress level for the LLS architecture. The random nature of the behavior precluded the determination of characteristic dynamic stiffness versus cycle number responses. In several tests, large decreases in dynamic stiffness were found to occur randomly during the test, the onset of which was associated with large hysteresis energy events. Also no differences were found in the type and order of occurrence of damage mechanisms. Therefore, the following section presents a characteristic initial and progressed damage state for the unnotched specimens from the LLS architecture.

A micrograph from an unnotched specimen containing an initial state of damage is shown in Figure 5.24, along with the corresponding dynamic tangent modulus and hysteresis energy information. Cracks in the resin rich areas and splits in the braider bundles were found in the specimen containing an initial damage state. The cracks and splits are represented by thin dark lines oriented vertically in the micrograph. Overall, the dynamic tangent modulus decreased as the number of test cycles increased, with the
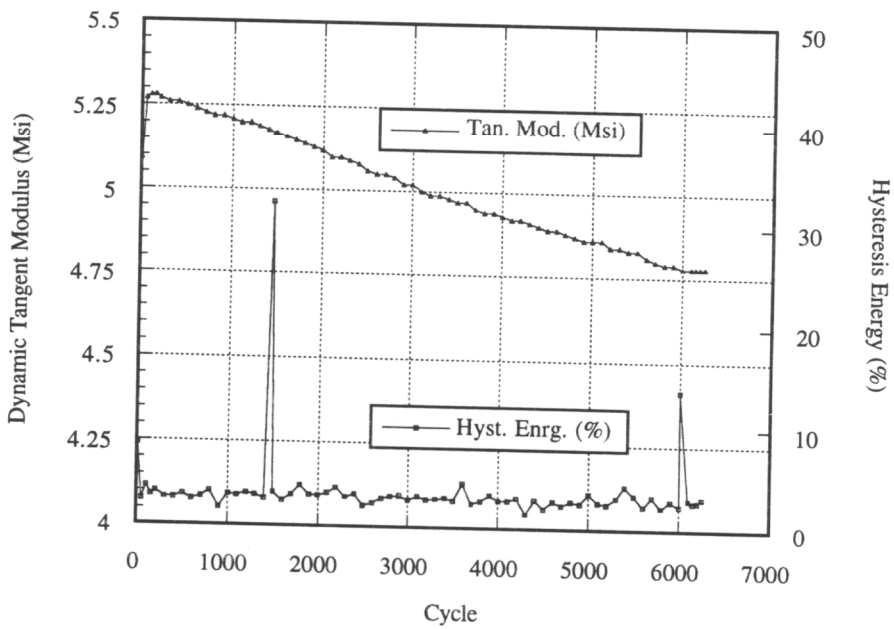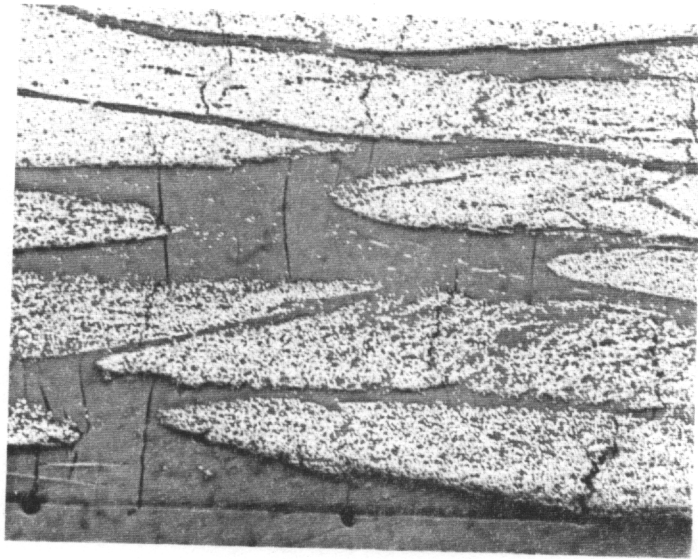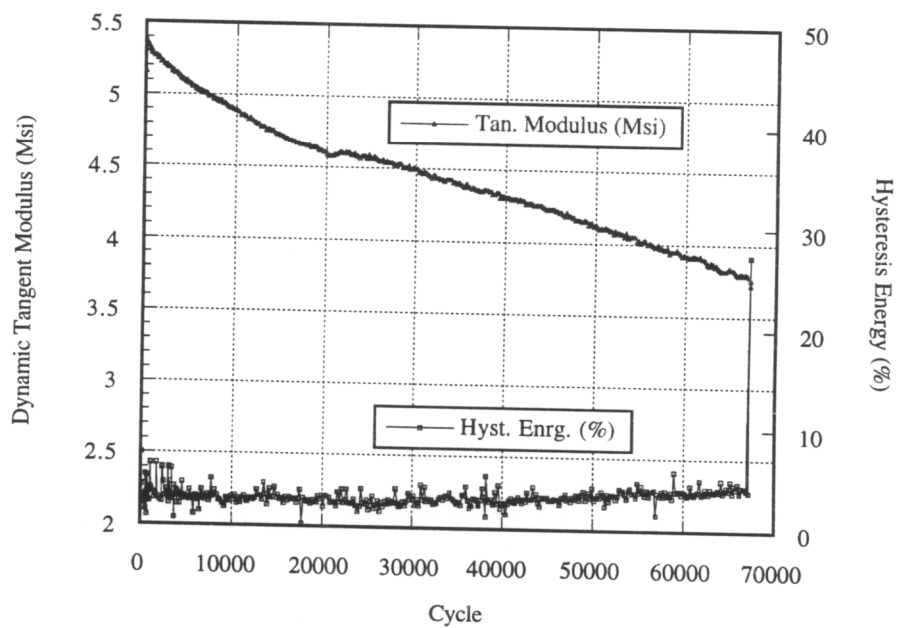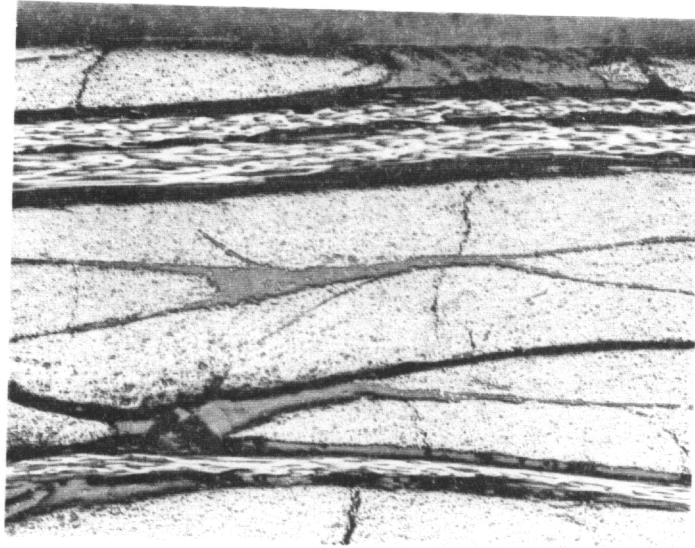
Figure 5.24 - Micrograph and Corresponding Dynamic Tangent Modulus and Hysteresis Energy Information vs. Cycle Number for an Unnotched Specimen from the LLS Architecture Containing an Initial Damage State

exception of the first region (~100 cycles) of the test. In that initial region, the dynamic tangent modulus increased from the first cycle, reached a peak value, and began a steadily decreasing response. This behavior was observed in all unnotched specimens tested. However, a clear relationship between the dynamic modulus measured on the first cycle and the peak value was not established. Hysteresis energy levels were nearly constant throughout the test, with one small energy event occurring near the end of the test.

A micrograph from an unnotched specimen containing a progressed state of damage is shown in Figure 5.25, along with the corresponding dynamic tangent modulus and hysteresis energy information. In the progressed damage state, extensive splitting in the axial fiber bundles along their length, and disbonding of the axial fiber bundles from their surrounding constituents was found. The splits and disbonds are represented by thick black lines oriented horizontally in the micrograph. An axial fiber bundle is contained between the black lines, and spans the micrograph horizontally. Splits in the adjacent braider bundles were also present. Several large hysteresis energy events were detected throughout the test as seen in the specimen response graph, the largest of which occurred just prior to test stoppage. With the exception of the large events, the average hysteresis energy response was nearly constant. A large decrease in dynamic tangent modulus was observed at approximately 17,000 cycles. This decrease was associated with one of the large hysteresis energy events. The large decrease in dynamic tangent modulus was found to coincide with disbonding and straightening of the undulating axial fiber bundles by
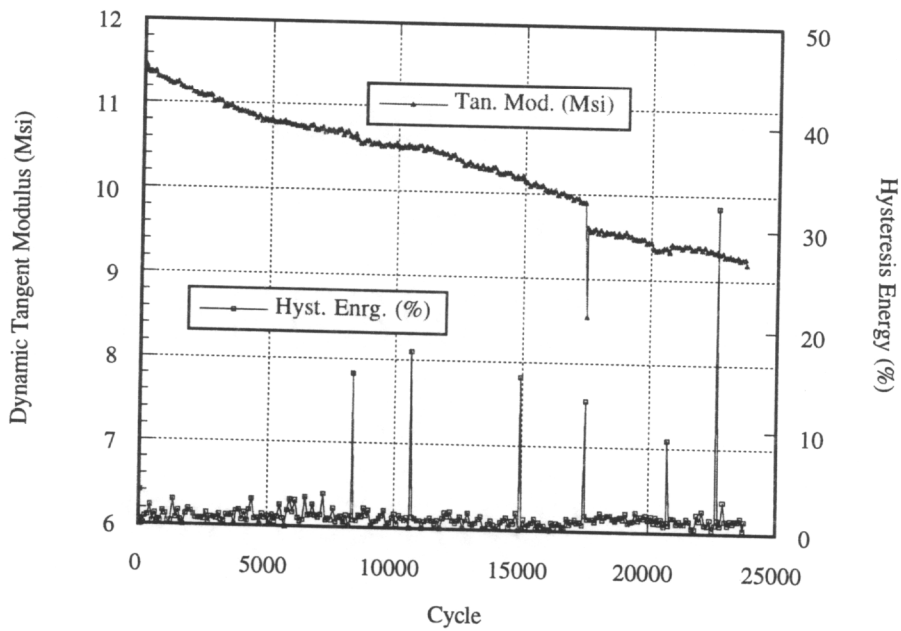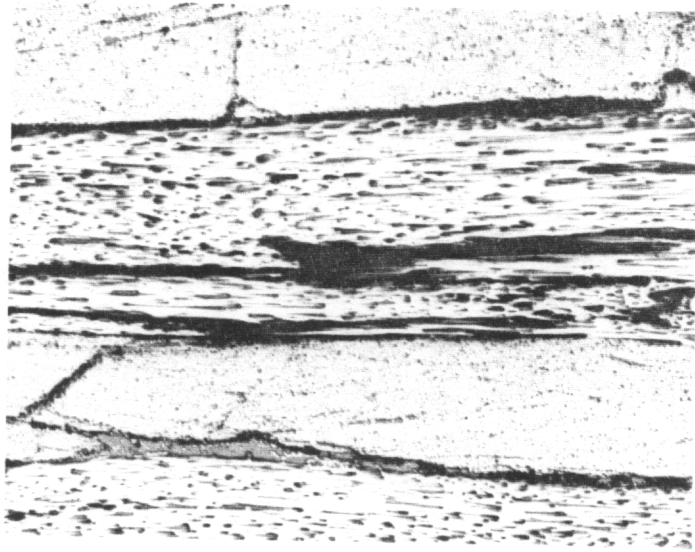
Figure 5.25 - Micrograph and Corresponding Dynamic Tangent Modulus and Hysteresis Energy Information vs. Cycle Number for an Unnotched Specimen from the LLS Architecture Containing a Progressed Damage State

viewing the edge of the specimen during the test with the microscope, and determining what damage mode occurred immediately after the drop in stiffness. Disbonding of the axial fiber bundles occurred throughout the specimen, the effects of which could only be determined when the damage was visible on the free edge of the specimen.This type of response was common in specimens tested from the LLS architecture.

Notched - The notched specimen responses from the LLS architecture were extremely inconsistent. The random nature of the individual specimens masked any change in response resulting from varying the peak applied stress level. The goal of the program was to test three specimens to three different damage levels at the same peak applied stress. The three damage levels corresponded with a 5%, 15%, and 25% dynamic tangent modulus reduction as compared to the initial dynamic tangent modulus. It was found that there was no relationship between the number of cycles and a given damage level, regardless of peak applied stress level. The type and progression of damage mechanisms was established for both the high and low peak applied stress level, and were found to be the same regardless of peak applied stress level. The following section presents a discussion of the hysteresis response, and the characteristic damage mechanism types and progression.

Normalized dynamic tangent modulus versus cycle number information for all six notched specimens is shown in Figure 5.26. Specimens 1,2 and 3 were tested at the low
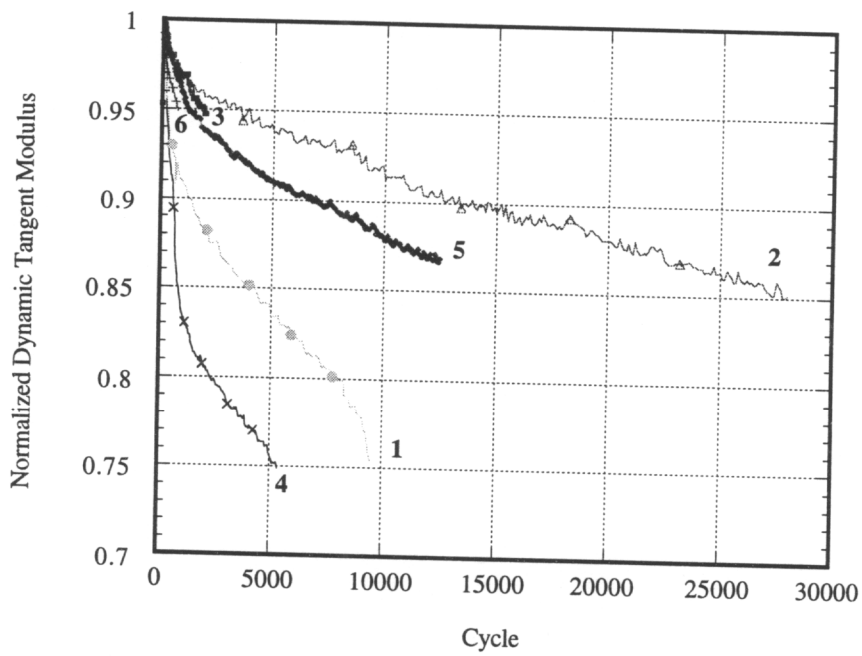
Figure 5.26 - Normalized Dynamic Tangent Modulus vs. Cycle Number for Six Notched Specimens from the LLS Architecture

stress level, while specimens 4,5 and 6 were tested at the high stress level. As is seen from the graph, there is no relationship between the magnitude of the dynamic stiffness reduction and the corresponding cycle number, regardless of the peak applied stress level. No differences in internal geometry in the LLS architecture were found which could account for the differences in rate of dynamic stiffness reduction. The types of damage mechanisms found at each individual level of dynamic stiffness reduction were however, consistent. Micrographs containing initial and progressed levels of damage are shown in Figure 5.27. In the initial damage state, cracks in the resin rich areas and splits in the braider bundles were found, represented by thin dark lines oriented vertically in the micrograph. In the progressed damage state, cracks in the resin rich areas and splits in the braider fiber bundles are present along with disbonding of the axial fiber bundles from their surrounding constituents, and splitting of the axial fiber bundles along their length.

Hysteresis energy information for the notched specimens differed from the unnotched specimens. The hysteresis energy values on the first cycle were typically two to three times greater than on subsequent cycles. Some spikes in the hysteresis energy were seen during the test, but occurred at a much lower frequency than in the unnotched specimens. The average hysteresis energy values were typically constant throughout the test, with the exception of the two specimens which yielded the highest rate of dynamic stiffness loss. In those two specimens, the average hysteresis energy values increased as the test progressed, as shown in Figure 5.28. The average hysteresis energy value approximately
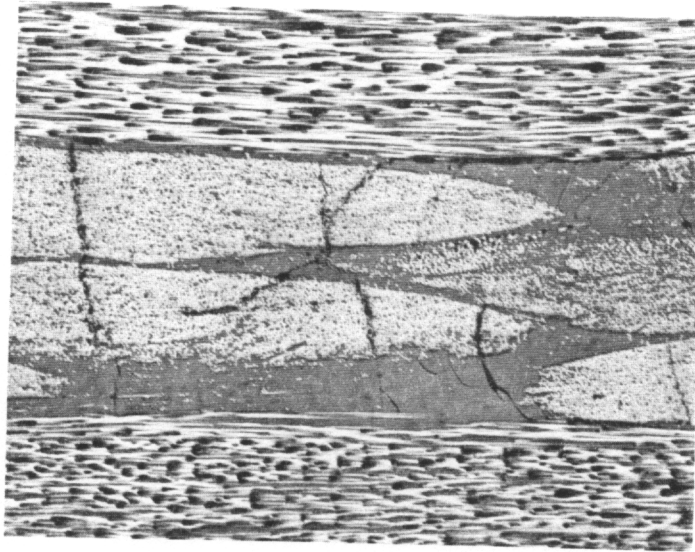
Initial Damage State
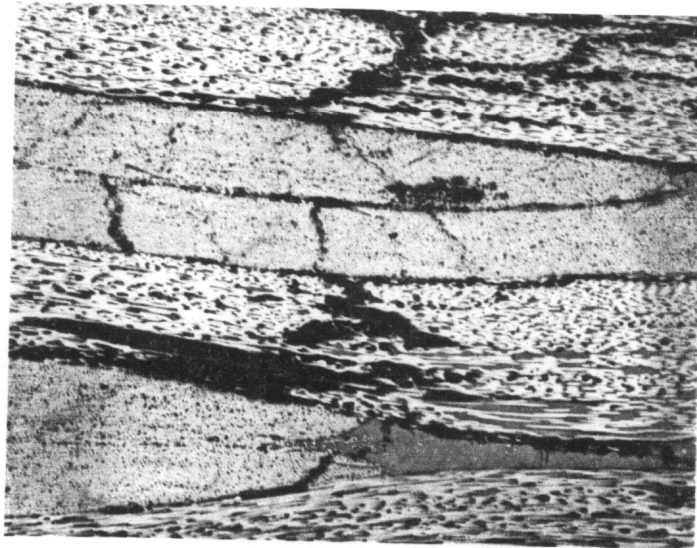
Progressed Damage State

Figure 5.27 - Micrographs of Characteristic Initial and Progressed Damage States in Notched Specimens from the LLS Architecture
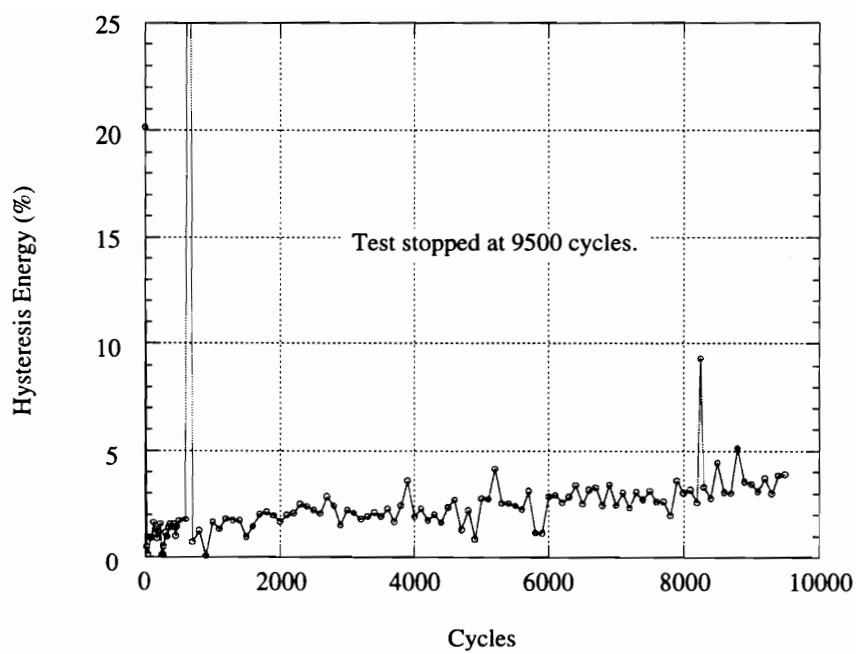
Figure 5.28 - Characteristic Hysteresis Energy Information vs. Cycle Number Graph for Notched LLS Specimens with an Increasing Hysteresis Energy Trend

doubled when the specimens were very near ultimate failure.

Overall, the responses from notched specimens were very inconsistent. There was no correlation between the number of cycles tested and the reduction in dynamic tangent modulus. The random nature of the individual specimens masked any change in response resulting from varying the peak applied stress level. A progression of damage mechanisms was established. Initially, cracks in the resin rich areas and splits in the braider bundles occurred. This damage state progressed into disbonding of the axial fiber bundles from their surrounding constituents, and splitting along their length.

5.3.3 $[0_{30K}/\pm70_{6K}]_{46\% \text{ axial}}$ (SLL) Architecture

Unnotched -The peak stress versus life plot for the four specimens tested to failure from the SLL architecture is shown in Figure 5.29, along with a straight-line log-linear fit of the data points, including the static strength value. This data set was used to determine high and low stress levels for the second phase of testing, which were 85 ksi and 84 ksi respectively. Due to the limited number of data points, only the two values of peak applied stress were extracted from this information. No other conclusions were inferred.

No trends in dynamic tangent modulus and hysteresis energy versus cycle number were found when comparing unnotched specimens tested at the low stress level to those tested at the high stress level for the SLL architecture. This random nature of behavior
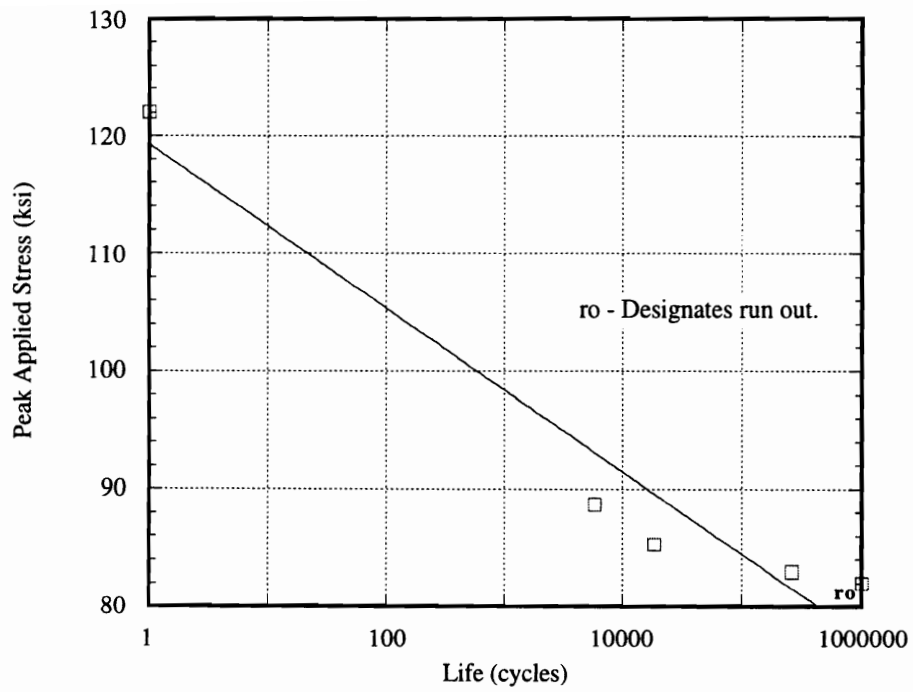
Figure 5.29 - Peak Stress vs. Life Plot for Four Tension-Tension Fatigue Specimens from the SLL Architecture

precluded determination of the effect of varying the peak applied stress level.

Two different types of dynamic tangent modulus versus cycle number responses were found. In the first case, the dynamic tangent modulus decreased as the number of test cycles increased. A dynamic tangent modulus and hysteresis energy versus cycle number graph and x-ray radiograph which display this type of behavior are shown in Figure 5.30. An x-ray radiograph of the damage was used to show the disbonding of the axial fiber bundles at the edges of the specimen along the gage length. Also, the extremely high density of splitting in the braider fiber bundles can be easily seen along with the splitting of many axial fiber bundles along their length. This type of damage mechanism was observed in $[0°/90°]_s$ crossply laminates under tension-tension fatigue loading by Reifsnider and Jamison [51]. It was determined using a simple classical lamination theory analysis that the 90° layers produced a positive transverse stress in the 0° layers which exceeded the transverse failure stress of the 0° layers, thus causing longitudinal splits in the 0° layers. A large amount, but not all of the splitting in the 0° layers occurred on the first cycle.

In the second case, the dynamic tangent modulus decreased during the initial portion of the test, and steadily increased in the latter portion of the test, as shown in Figure 5.31. This behavior was not a true specimen response, but a result of the type of strain measurement used in the testing. As was described in the test specimen fabrication
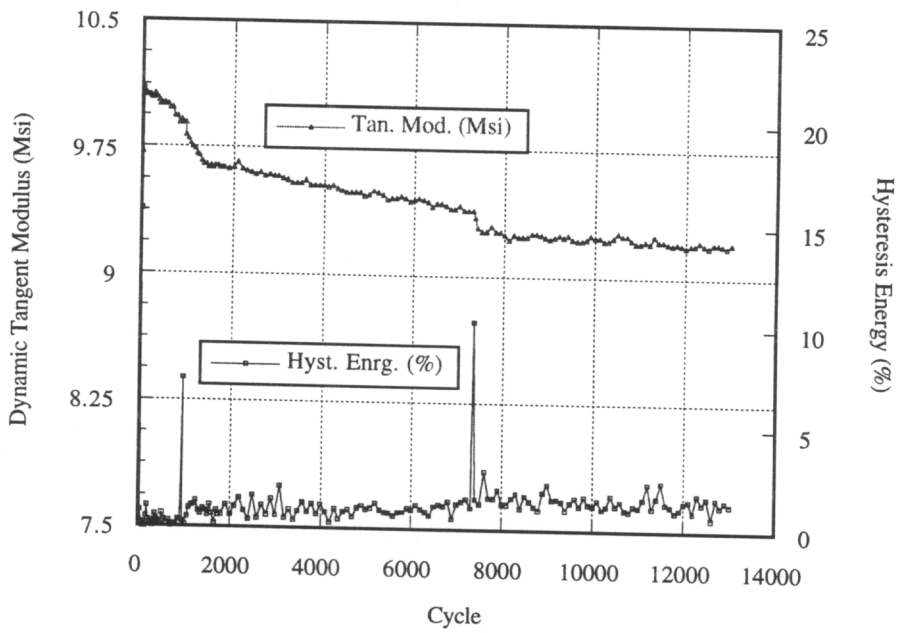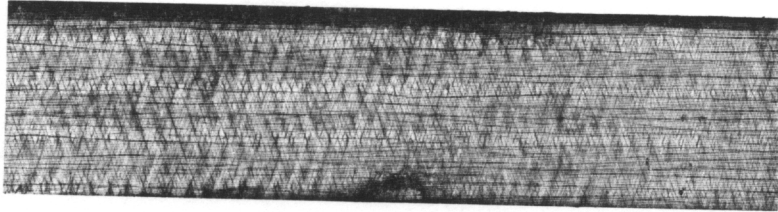
Figure 5.30 - First Type of Damage Micrograph and Corresponding Dynamic Tangent Modulus and Hysteresis Energy Information for an Unnotched Specimen from the SLL Architecture

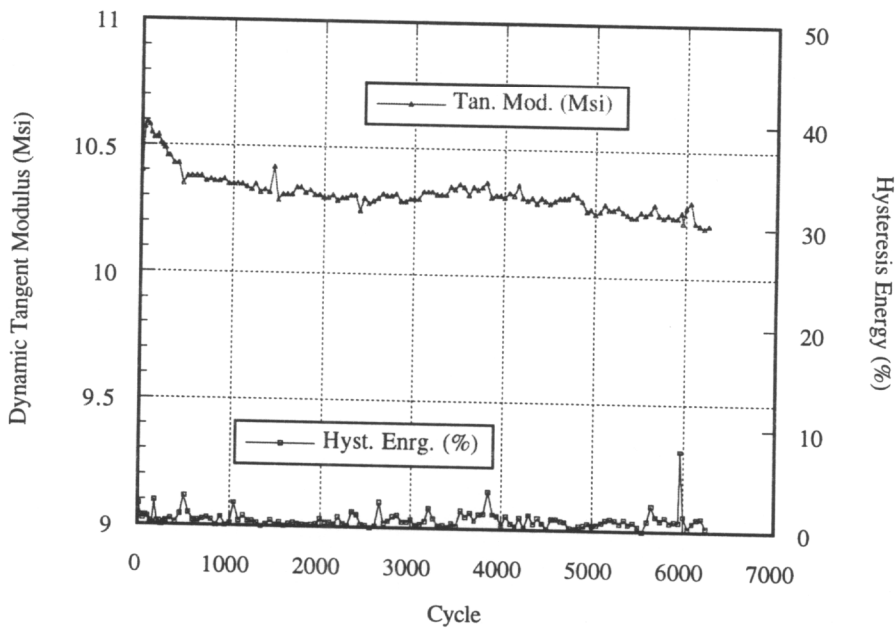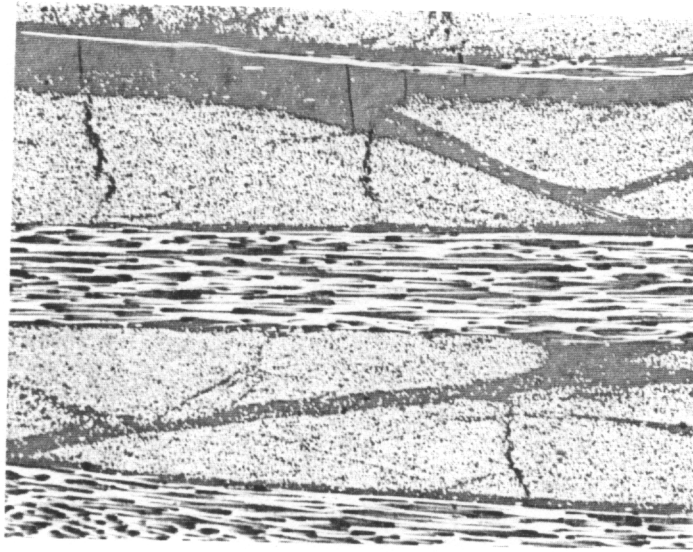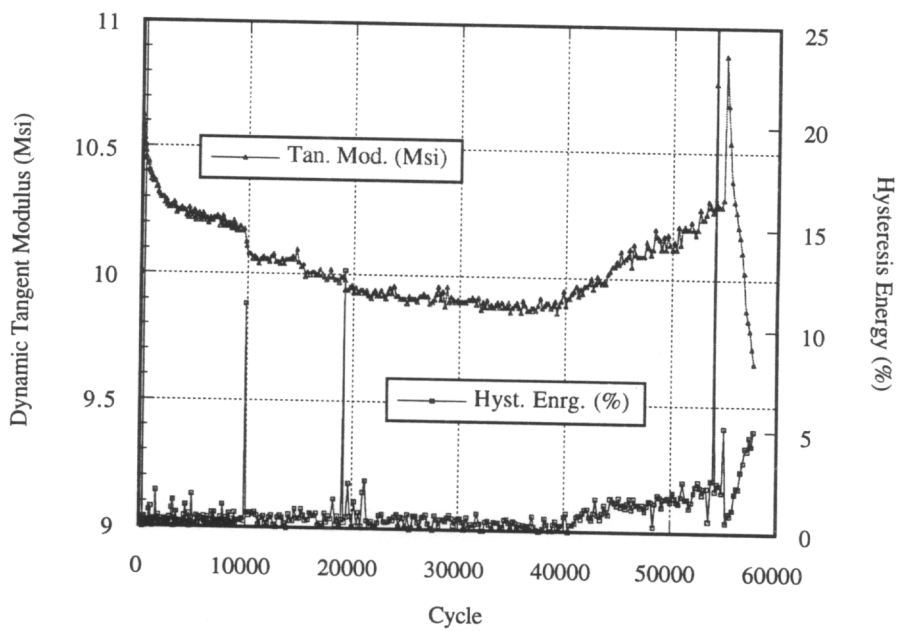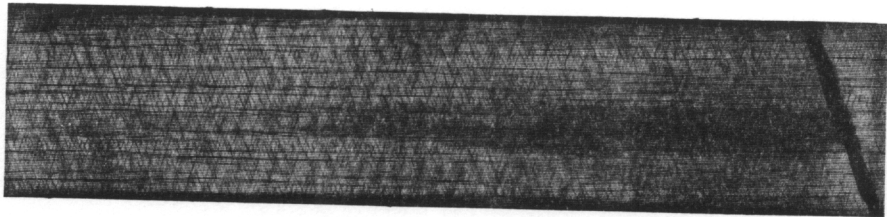Figure 5.31 - Second Type of Damage Micrograph and Corresponding Dynamic Tangent Modulus and Hysteresis Energy Information for an Unnotched Specimen from the SLL Architecture

section, the extensometer was mounted on the specimen using grooved aluminum pads to secure the individual feet of the extensometer. In the corresponding radiograph, a long dark region can be seen in the center of the specimen along its gage length. This represents an axial fiber bundle which has disbonded from its surrounding constituents. This also corresponds with the line on which the extensometer was placed. When the axial fiber bundle disbonded from the surrounding braider fiber bundles, the strains in the braider fiber bundles decreased, particularly those on the surface of the specimen on which the extensometer was mounted. The damaged braider bundles on the surface had a significantly reduced load carrying capability, and when detached from the primary load carrying components (i.e. axial fiber bundles) sustained much lower strain levels. Therefore, the extensometer indicated a smaller strain in the specimen at the same applied load level, and thus a much higher apparent stress level. The overall result was the erroneous dynamic stiffness response shown in the figure.

Most of the splitting in the braider fiber bundles occurred on the first cycle. Stress-strain information for a representative sample is shown in Figure 5.32. Information from the first cycle and the 300th cycle are plotted. The area inside the first cycle stress-strain loop is much greater than the area inside the 300th cycle. In all specimens tested from the SLL architecture, the hysteresis energy values on the first cycle were 25-30 times higher than on subsequent cycles.
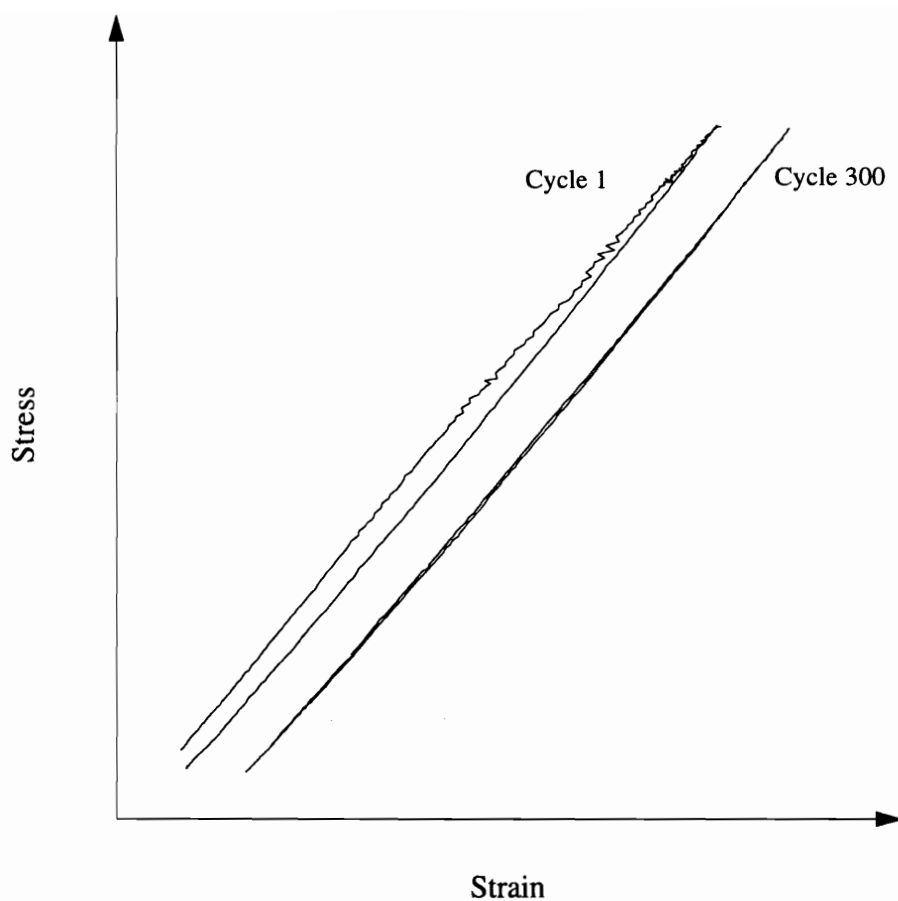
Figure 5.32 - Representative Stress vs. Strain Information for Loading Cycles from the First and 300th Test Cycle in an Unnotched Specimen from the SLL Architecture

Overall, the damage mechanisms found in the unnotched specimens from the SLL architecture were splitting in the axial and braider fiber bundles along their length, and disbonding of the axial fiber bundles from their surrounding constituents. A significant portion of the splitting in the axial and braider fiber bundles took place on the first cycle of the test, which corresponded with hysteresis energy values 25-30 times greater than on subsequent cycles.

Notched - Specimens from the SLL architecture were extremely notch sensitive as compared to the unnotched specimens. Test durations were typically an order of magnitude less for a notched specimen as compared to an unnotched specimen at the same level of dynamic tangent modulus reduction. The dynamic tangent modulus versus cycle number responses for the notched SLL architecture specimens were the most consistent of any of the architectures tested. Although the specimens were consistent, there were still no distinguishable differences found between specimens tested at the high stress level and those tested at the low stress level. The following section presents representative notched specimen responses from the SLL architecture.

Normalized dynamic tangent modulus versus cycle number curves are shown in Figure 5.33 for three specimens tested at the high stress level. The number corresponding to each test is placed on the graph at the point where the respective test was stopped. The response from the three specimens was very consistent. As the number of test cycles
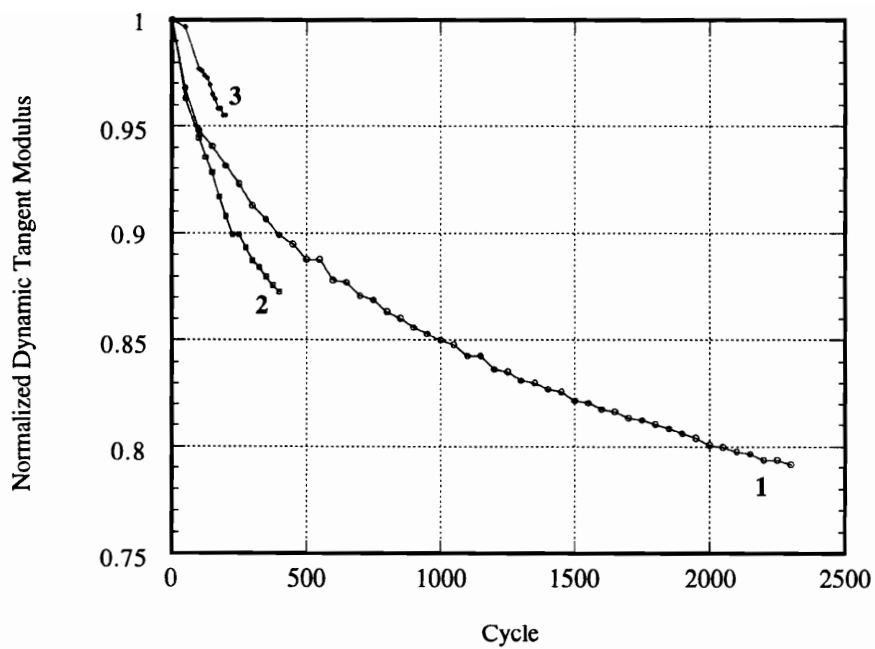
Figure 5.33 - Normalized Dynamic Tangent Modulus versus Cycle Number Curves for Three Notched Specimens from the SLL Architecture Tested at the High Stress Level.

increased, the normalized dynamic stiffness decreased in a smooth manner. No jumps or drops were seen in the dynamic stiffness responses. A representative hysteresis energy response curve for the notched specimens is shown in Figure 5.34. In all specimens, the value on the first cycle of the test was 20-30 times higher than the values of subsequent cycles. As the test progressed, the hysteresis energy value increased in a linear fashion. In tests which the specimen was near ultimate failure, the final hysteresis energy value was nearly double the initial average value of the test.

X-ray radiographs from specimens containing initial and progressed damage states are shown in Figure 5.35. In the initial damage state, extremely high densities of splitting in the axial and braider fiber bundles is present. A significant portion of this damage took place on the first cycle. Disbonding of an axial fiber bundle immediately above the notch is represented by a dark region in the radiograph. In the specimen containing a progressed damage state, the black line running along the center of the radiograph represents a nickel coated axial fiber bundle. These nickel coated bundles are white in color, as compared to the normally black uncoated graphite fiber bundles, and are used by the textile manufacturer as tracer fiber bundles. The braid type can be verified by checking the path of the tracer bundles. The radiograph of the progressed damage state exhibits splitting of the axial and braider fiber bundles along their respective lengths, and also a more advanced state of disbonding of an axial fiber along its length, indicated by the dark regions adjacent to the nickel coated axial fiber bundle. The specimen with the initial
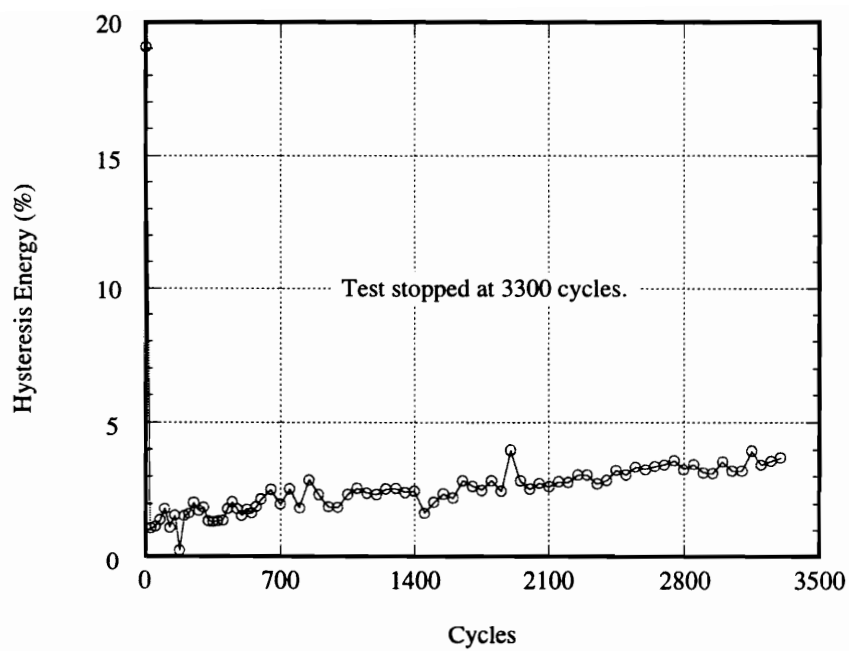
Figure 5.34 - Representative Hysteresis Response Curve for Notched Tension Fatigue
Specimens from the SLL Architecture
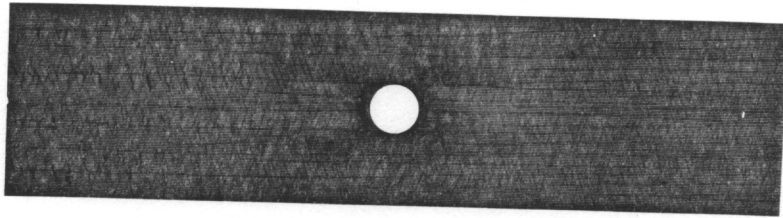
Initial Damage State
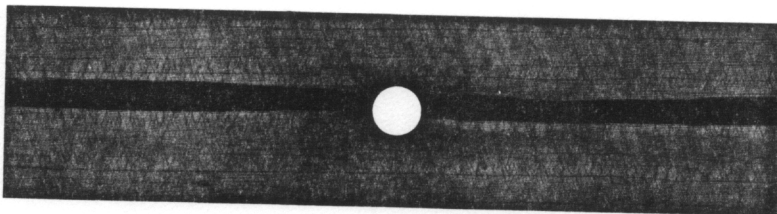
Progressed Damage State

Figure 5.35 - Radiographs of Initial and Progressed Damage States from Notched
Tension Fatigue Specimens from the SLL Architecture

damage state underwent a 5% dynamic stiffness decrease, while the specimen with the progressed damage state underwent a 25% dynamic stiffness decrease.

Overall, notched specimens from the SLL architecture were extremely notch sensitive as compared to unnotched specimens from the same architecture. Most of the damage took place on the first cycle, and was in the form of splitting in the axial and braider fiber bundles along their length, and disbonding of the axial fiber bundles from their surrounding constituents.

5.3.4 $[0_{75K}/\pm70_{15K}]_{46\% \ axial}$ (LLL) Architecture

Initial tension-tension fatigue testing was completed on specimens from the LLL architecture. Of the three specimens tested, a dominant behavior was found. In the initial stages of the test, damage mechanisms consistent with those found in the SLL architecture were found. A radiograph from one of the LLL architecture specimens containing an initial damage state is shown in Figure 5.36. Splitting in both the braider and axial fiber bundles is present in large densities. The dark band in the radiograph is a nickel coated axial fiber bundle. As the test progressed, the axial fiber bundles disbonded along their length as was explained in the previous section on the response of the SLL architecture. In the case where the axial fiber bundle beneath the extensometer disbonded from the damaged braider bundles, the apparent strain reading decreased, yielding an increasing stiffness value with increasing cycle number. This behavior was dominant in the LLL
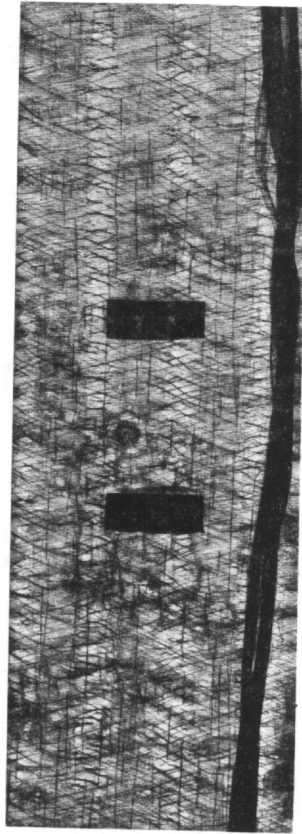
Figure 5.36 - Radiograph of an Unnotched LLL Architecture Specimen Containing an Initial Damage State

architecture. The increased size of the axial fiber bundles made accurate strain measurements impossible with the present strain measurement system. The width of the axial fiber bundles was approximately equal to the width of the aluminum pads used to mount the extensometer to the specimen. Therefore, the remaining specimens from the LLL architecture were reserved for future testing, after an accurate method of strain measurement has been established. No further detailed results on tension-tension fatigue testing of the LLL architecture will be presented.

5.4   Overall Conclusions

5.4.1 Effect of Axial Bundle Size (LSS vs. LLS)

Unnotched - The type and order of damage mechanisms was found to be consistent for both the LSS and LLS architectures. The initial damage mechanism was splitting of the braider fiber bundles along their length. Next, axial fiber bundles began to disbond along their length from the surrounding constituents. The final failure mechanism was rupture of the axial fiber bundles.

The dynamic tangent modulus versus cycle number response decreased smoothly as the number of test cycles increased for the LSS architecture. The dynamic tangent modulus decreased as the number of test cycles increased for the LLS architecture as well, however, sudden drops in dynamic tangent modulus yielded a piecewise smooth response.

Large random hysteresis energy events were detected throughout unnotched testing in both architectures. Because the gage section was four times larger than the extensometer gage length, only those energy events in the immediate vicinity of the extensometer were detected; some audible events were not detected. The most common correlation observed by comparing the real time response output and the video monitoring of the specimen edge was between splitting of the axial fiber bundles and spikes in the hysteresis energy response. Abrupt propagation of disbonding of the axial fiber bundles along their length was also correlated with spikes in the hysteresis energy response. The largest hysteresis energy spikes were caused by rupture of the axial fiber bundles immediately prior to ultimate failure.

The average hysteresis values for all specimens from the LSS architecture were approximately twice that of specimens from the LLS architecture. This correlated with the results from the static tension testing which showed that the stress-strain response from LSS architecture was nonlinear to failure, while that from the LLS architecture was nearly linear to failure.

Variability in specimen response precluded a correlation between the number of cycles tested at a given stress level, and the amount of dynamic stiffness decrease and corresponding damage state for the LLS architecture. Also, the effect of changing the peak applied stress level was masked by the variability of the specimen responses.

Notched - The type and order of damage mechanisms was found to be consistent for both the LSS and LLS architectures. The initial damage mechanism was splitting of the braider fiber bundles along their length. Next, axial fiber bundles began to disbond along their length from the surrounding constituents. The final failure mechanism was rupture of the axial fiber bundles. In all notched specimens, the damage was concentrated around the edges of the notch, and progressed toward the edges of the specimens along 45° lines starting at the notch edges. This corresponded with the 45° braid angle of both the LSS and LLS architectures.

The dynamic tangent modulus versus cycle number response decreased smoothly as the number of test cycles increased for notched specimens from both the LSS and LLS architectures.

Both the LSS and LLS architectures displayed variable notch sensitivities. In the LSS architecture, the rate of dynamic tangent modulus decrease was found to occur more rapidly as the axial fiber bundles were placed in a stacked configuration adjacent to the notch. The greater the number of axial fiber bundles stacked along the edge of the notch, the greater the rate of dynamic stiffness decrease. In the LLS architecture, variable notch sensitivities were also found, but were not correlated with any specific stacking sequence of the axial fiber bundles.

No major hysteresis energy events were detected in the notched LSS specimens until

immediately prior to ultimate failure. Large hysteresis energy events were also very rare in notched specimens from the LLS architecture, but were found to occur at random points throughout the tests.

Variability in specimen response precluded the determination of the effect of changing the peak applied stress level. The effects of the high and low applied stress levels were masked by the varied response of notched specimens.

5.4.2 Effect of Architecture Scaling (SLL vs. LLL)

Unnotched - The type and order of damage mechanisms was found to be consistent for both the SLL and LLL architectures. The initial damage mechanism was splitting of the braider fiber bundles along their length, most of which occurred on the first cycle of the test. Next, axial fiber bundles began to split along their length. Later in the test, axial fiber bundles began to disbond along their length from the surrounding constituents. The final failure mechanism was rupture of the axial fiber bundles. The disbonding of the axial fiber bundles along their length yielded erroneous strain readings when the bundles resided under the location of the extensometer. This behavior occurred in some specimens tested from the SLL architecture, and all specimens tested from the LLL architecture. Further testing of the LLL architecture was halted until an improved method of strain measurement is devised. The following conclusions refer to the SLL architecture only.

The variability of the unnotched specimens from the SLL architecture precluded the determination of the effects due to changing the peak applied stress level.

A significant portion of the splitting found in the braider fiber bundles occurred on the first cycle of the test as indicated by the large hysteresis energy values on the first test cycle. Large hysteresis energy events also occurred randomly through all unnotched tests, and were associated with splitting in the braider fiber bundles and disbonding of the axial fiber bundles along their length.

Notched - Damage mechanism types and sequences for notched SLL architecture specimens were consistent with those found for the unnotched specimens. In the notched specimens, however, the damage was localized around the edges of the notch.

The SLL architecture was extremely notch sensitive. Stress levels below those defined by an equivalent net-section level from the unnotched specimens had to be used in order to obtain specimen lives long enough to permit study of the specimen response. Therefore, the effect of varying the applied stress level could not be determined. Dynamic tangent modulus values decreased in a smooth fashion as the number of test cycles decreased for all notched specimens.

The first cycle of each notched specimen test yielded hysteresis energy events 20 to 30 times greater than on subsequent cycles. No other significant hysteresis energy events were detected after the first cycle in any of the six notched specimen tests.

6. Compression Fatigue Testing

Compression-compression fatigue testing was completed on the four braided architectures presented in this investigation. A first group of specimens was tested to failure to determine the characteristic fatigue responses of each architecture. A second group of specimens was tested to predetermined damage levels in order to destructively evaluate damage types and mechanisms. This chapter presents the experimental results from the compression-compression fatigue testing program.

6.1 Test Configuration Selection

Several different methods exist for compression-compression fatigue testing of composite materials. Generally, there are two types of fixtures. The first type consists of a fixture which supports the gage length of the test specimen, thus suppressing buckling. The second type is a free gage length configuration which does not restrict the motion of the gage section of the specimen. These fixtures can provide either end-loading, shear-loading, or a combination of the two types of loading. In the present study, a free gage

section was chosen in order that damage mechanisms could more easily be monitored during the test. A second requirement was that the test specimen also meet the specifications for a tension-compression loading configuration. Together, these specifications meant that the unsupported gage length be as long as possible, without being susceptible to buckling. The chosen testing configuration is shown in Figure 6.1. The testing fixture was simply the hydraulic grips of the servohydraulic test system. The specimen has 1.75 inches in both the upper and lower grips. Stainless steel mesh was placed between the actual gripping surface and the specimen in order to provide a smooth loading transition from the grips to the specimen. The gage length was 1.20 inches long, and was unsupported. This allowed the faces and edges of the specimen to be monitored during the test, as well the application of strain measurement devices on the front and back faces.

Buckling load calculations for specimens from the four braided architectures were completed as described in Appendix B. It was required that the peak loads applied to the specimens be well below the buckling loads of the specimens to avoid the global buckling failure mode. For the 1.2 inch gage length used in this study, the peak applied loads to specimens from each respective architecture were all less than twice the corresponding buckling load. This factor of two allowed for a significant reduction in longitudinal modulus during the test, while still remaining below the global buckling load of the damaged specimen.

steel mesh between specimen
and grips (top and bottom)

0.5 " extensometer
mounted on face

0.25" x 0.25" strain gage
mounted on face

specimen

machine grips

aluminium mounting pads
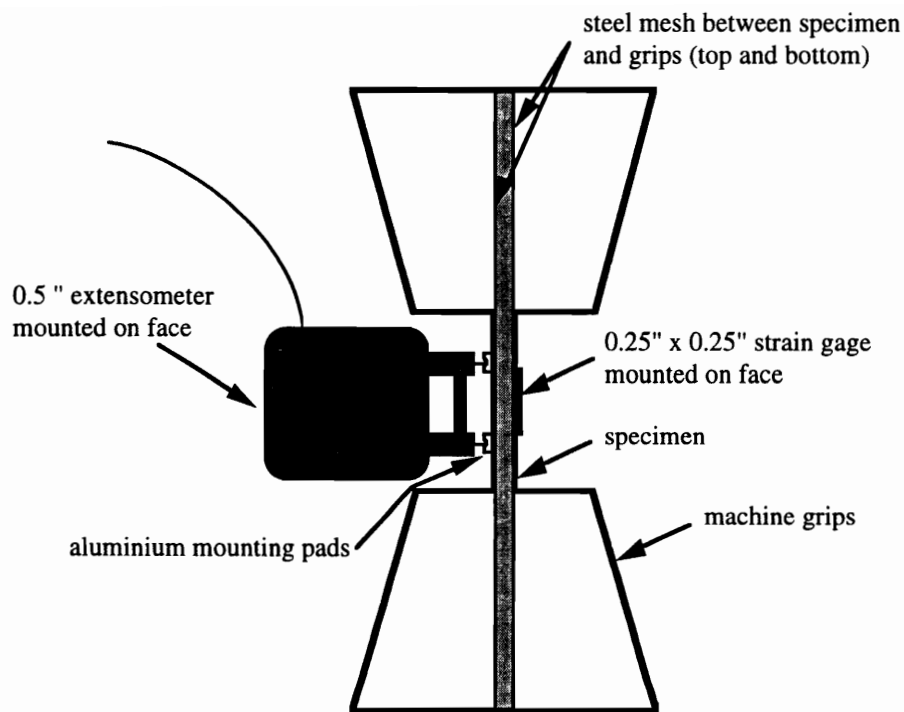
Figure 6.1 - Compression-Compression Fatigue Testing Configuration Schematic

6.2 Test Specimen Fabrication

Individual specimens were cut from the main panel using a water cooled diamond blade saw to the dimensions shown in Figure 6.1. All specimens had a 1.20 inch gage length, with 1.75 inches in each of the hydraulic grips of the load frame. Specimens were 1.0 inches wide for each architecture with the exception of the LLL architecture, which had a gage width of 1.5 inches to accommodate the larger scale of the LLL architecture. The circular notch was machined in each specimen using a water cooled drill bit.

If the edge of the specimen was not smooth enough to view after the saw cut had been completed, the edge was polished as discussed in previous chapters. Aluminum extensometer tabs were adhered to the face of the specimen using silicone glue. The tabs were placed such that the extensometer would rest in the geometric center of the gage section. For the notched specimens, the aluminum pads were placed so the extensometer would rest directly over the notch.

6.3 Experimental Program

The knowledge gained from completing the tension fatigue testing program influenced the test matrix of the compression fatigue testing program. Instead of trying to establish "high" and "low" stress levels, one stress level which would yield a life of approximately 100,000 cycles was chosen. The first ten specimens from each architecture were tested to failure at various stress levels. This data was used to establish a peak stress level versus

w = 1.0" for the LSS,LLS & SLL arch's.
w = 1.5" for the LLL arch.

w

1.875"   grip section

1.2"   gage length

4.95"

d=w/4, hole centered
on face of specimen
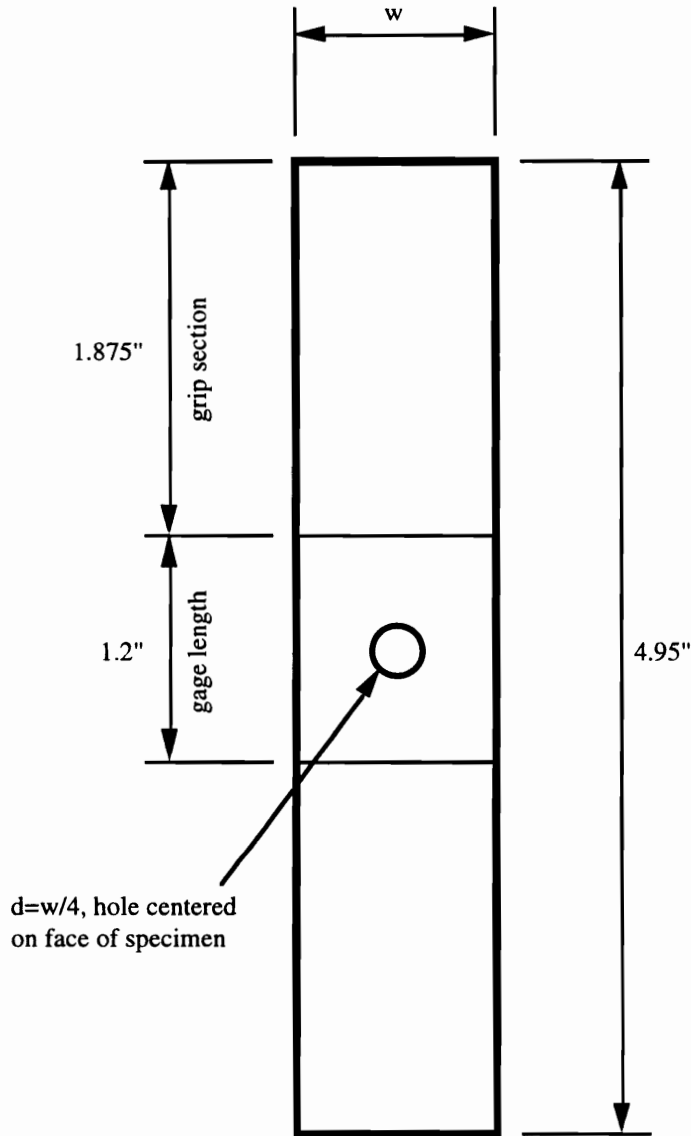
Figure 6.2 - Compression-Compression Fatigue Specimen Dimensions

life (S-N) diagram. From this diagram, the peak stress level at which an average specimen would last 100,000 cycles was chosen for each architecture. At this stress level, six unnotched specimens and six notched specimens were tested in groups of two to specific damage states . Notched compression-compression fatigue specimens were tested at the same net stress levels as were the unnotched specimens. All notched specimens contained a circular notch located at the geometric center of the gage area. The notch diameter was 0.25 times the gage width of the specimen. For the LSS, LLS, and SLL architectures, a 0.25 inch diameter hole was used. For the LLL architecture, a 0.375 inch diameter hole was used. The peak applied load for the notched specimens was determined by multiplying the peak applied stress level for the unnotched specimens by the reduced cross-sectional area at the center of the notched gage section, perpendicular to the direction of loading. This consistency of peak applied net-section stress provided the capability of evaluating the response of each architecture subjected to a stress concentration. Identical tests were run on two specimens in contrast to the tension fatigue testing program which used one specimen. A graphical representation of the three damage/life regions of interest is shown in Figure 6.3. The data set in the figure is a typical dynamic tangent modulus versus life response from a braided composite in compression fatigue. Region 1 included any initial damage at the beginning of the test. Region 2 included any damage which occurred in the middle ranges of the test. Region 3 included information as close to ultimate failure as possible without ultimate failure actually occurring. The goal was to test two specimens in each damage region. The first two
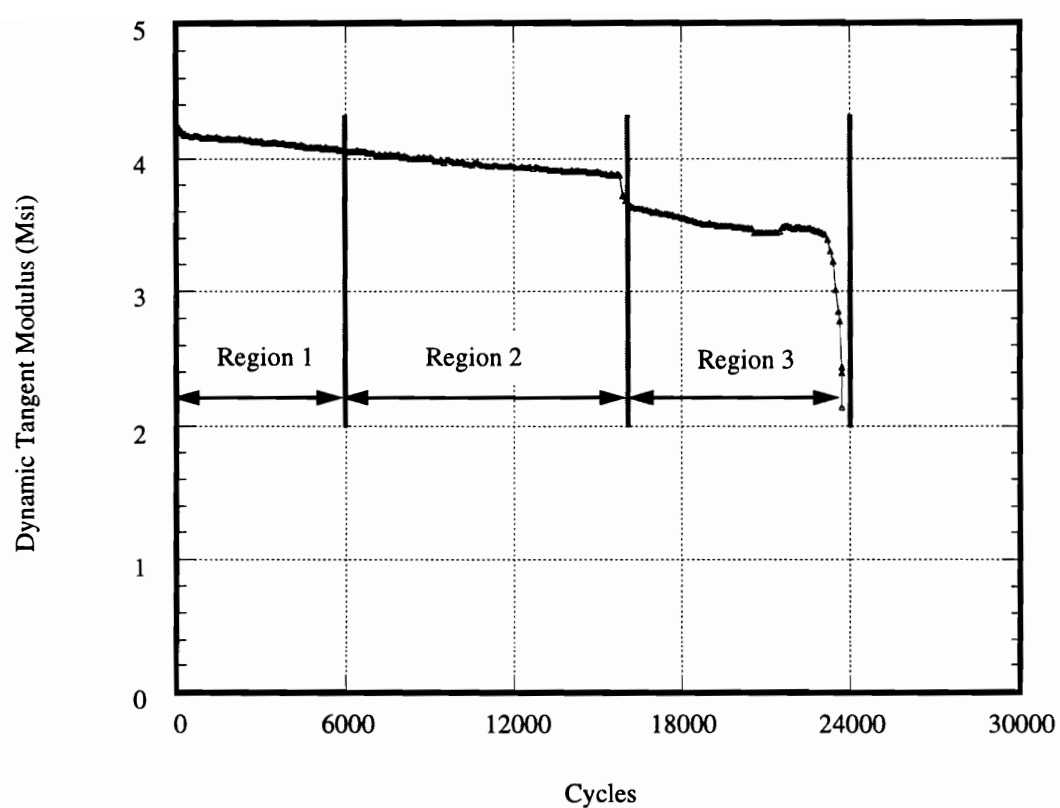
Figure 6.3 - Description of Damage Regions for Compression Fatigue Testing of 2-D Braided Composites

specimens were tested to damage levels as close to failure as possible, without reaching catastrophic failure. The second two specimens were tested until the first signs of damage were seen either in the form of dynamic stiffness loss or significant hysteresis energy events. The final two specimens were tested to levels where there was no outwardly detectable damage in the specimen, but where the specimen had undergone several loading cycles.

Tested specimens were impregnated with a zinc-iodide solution and x-rayed. From the x-ray information, damaged areas in the gage section were identified, and specimens were sectioned such that damaged areas could be examined in a microscope. The sectioned segments were then cast in epoxy resin and polished for microscopy work. All cuts were made with a water-cooled diamond blade saw.

All tests were completed on an 20 kip MTS 810 servohydraulic load frame fitted with an MTS 458 controller. Loading input was a 5 Hz sine wave programmed through a micro-profiler. This allowed the first cycle to start at zero load, ramp up to the desired peak load, and from there complete the specified minimum to maximum load ratio (R). All tests were run at R=10. Load and strain were monitored with the data acquisition setup described in Appendix A. Strain was measured using an MTS 0.5 inch gage length extensometer, attached to the specimen as shown in Figure 6.1. A small rubber band extended from one side of each foot of the extensometer, around the back of the specimen,

and to the hook on the opposite side of the respective extensometer foot. When a second

strain measurement was required, a Micro Measurements EA-06-250AE-350 (0.25 inch

by 0.25 inch square gage area) strain gage was placed on the face opposite the

extensometer and read simultaneously with the extensometer. Bending calculations were

completed real time by calculating the percent difference between simultaneous strain

readings from the gage and the extensometer over the loading portion of the cycle. The

average difference was then calculated by finding the average of all the data points. This

number was termed "percent bending". Percent bending calculations were completed on

randomly selected unnotched specimens. A stereo microscope was used to monitor areas

of the gage section where damage did or might occur. A video recording unit was attached

to the microscope in order to save damage events for later study.

6.4   Discussion of Results

6.4.1 $[0_{6K}/\pm45_{15K}]_{12\% \, axial}$ (LSS) Architecture

Unnotched - The peak stress versus life plot for the ten specimens tested to failure

from the LSS architecture is shown in Figure 6.4, along with a fit to the equation

$y = a + b\log N$. The linear correlation coefficient R is also listed. This parameter gives an

indication as to how well the data fit the straight line. An R value of 1.0 means the line fit

the data perfectly, while an R value of zero means the data showed no linear tendencies.

The LSS architecture had an R value of 0.985 indicating the data matched the linear
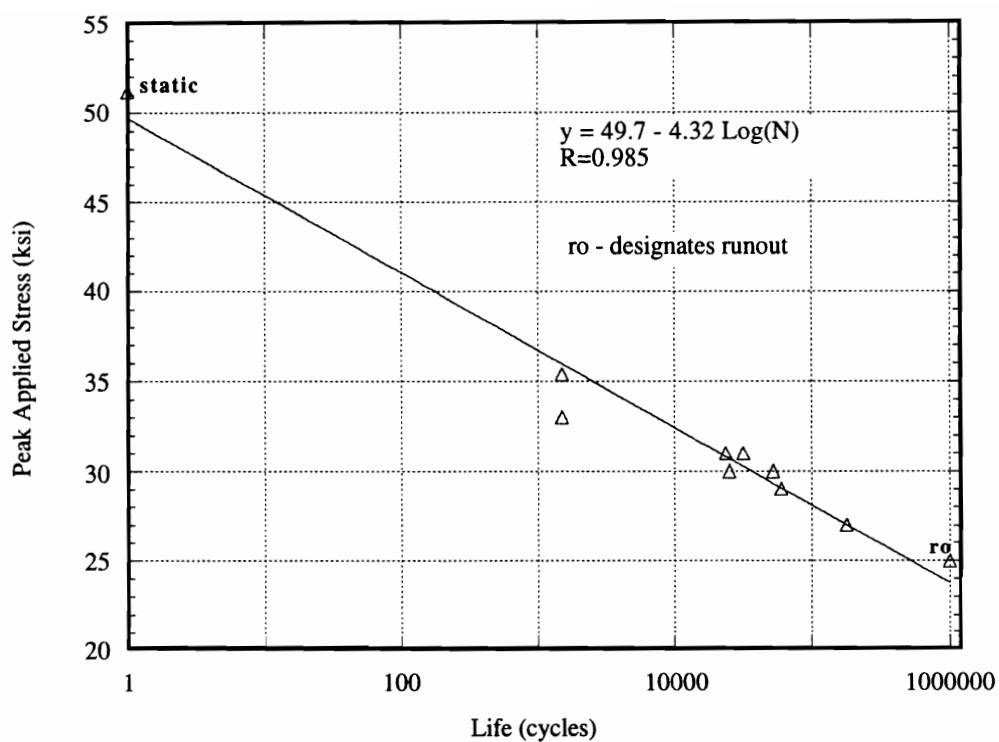
Figure 6.4 - Peak Stress versus Life for Ten Specimens Tested to Ultimate Failure from the LSS Architecture

relationship reasonably well. However, when looked at from a statistical point of view, the accuracy of the fit is called into question. The linear correlation coefficient does not address the probability of the data set actually matching the linear model. A second analysis was completed using a least squares fit as a maximum likelihood estimator. This analysis requires knowledge of the errors involved in the measurement of the data. From this information, the probability that the data could have come from the least squares linear model is calculated. The computer code used in this analysis was the program "fit.c" obtained from reference [78]. For specimens with a 1.0 inch wide gage length and thicknesses between 0.105 inches and 0.109 inches, the error in measurement of the peak stress values using the data acquisition setup described in Appendix A was ±0.10 ksi. When the analysis was completed with this error value, the probability that the peak stress versus life data matched the linear fit was zero. From a statistical point of view, there is no chance the model fit the data. This is not an indication of a poor choice in models, but rather a true picture of the random nature of fatigue testing results. The experimental scatter of life versus peak stress level data is very high. This study is not concerned with accurate prediction of life at a given peak stress level, but rather determining the damage mechanisms that occur as the life of the specimen progresses. Thus, no significance should be placed on the linear fit of data shown in Figure 6.4.

Generally there were two characteristic stiffness versus cycle number responses found, both of which are shown in Figure 6.5. The first type of response yielded a steadily
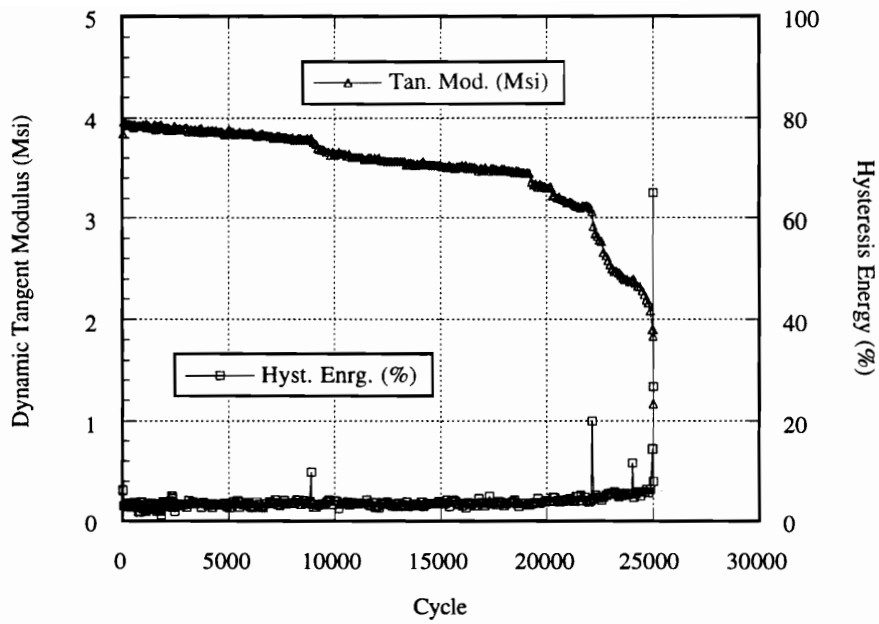
Type 1
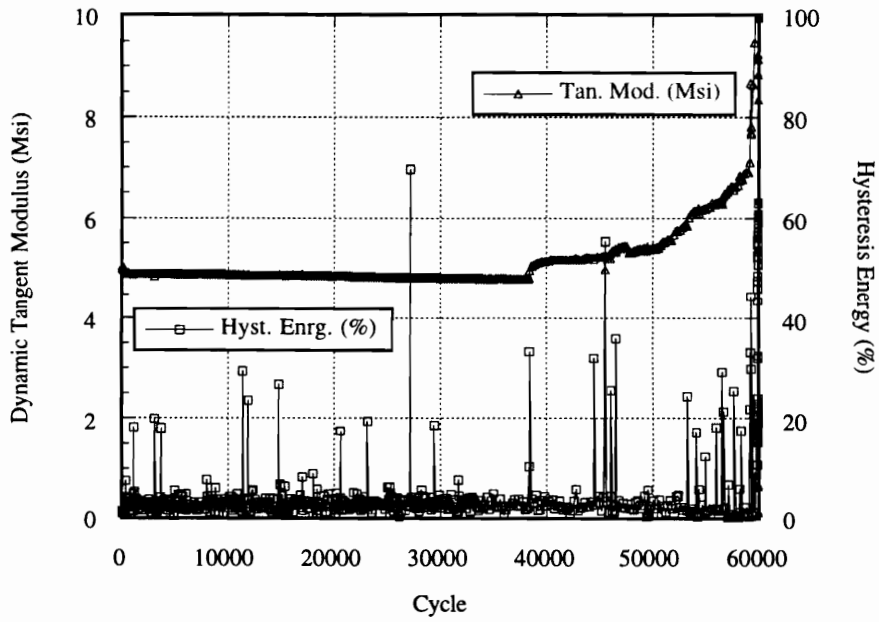
Type 2

Figure 6.5 - Characteristic Dynamic Tangent Modulus and Normalized Hysteresis Energy versus Cycle Number Graphs for the LSS Architecture.

decreasing stiffness value as the number of cycles increased. Significant energy events were sometimes associated with the onset of a rapidly decreasing stiffness region, as well as occurring randomly throughout the test. The second type of response yielded a decreasing stiffness value as the number of cycles increased, up to a critical point where an energy event triggered a region in which the stiffness value increased and became very erratic until ultimate failure. The onset of this region was always accompanied by a significant energy event.

Information from the ten specimens tested to failure was used to determine the peak stress level used for the second phase of testing, as well as stopping points for each of the three damage regions described in section 6.3. The peak stress level for the second phase of testing was chosen to be 28.0 ksi. This stress level yielded an approximate life of 100,000 cycles, based on the average response of the ten failed specimens.

In approximately the first 10% of life, splitting of the braider bundles along their length, and disbonding of the axial bundles from their surrounding constituents was found. Figure 6.6 shows an axial bundle which has begun to disbond along its length as indicated by the dark line running along the lower side of the upper bundle. The axial bundles in the micrograph are seen running from left to right. A crack was also found that existed in both the curved region of an axial bundle and an adjacent braider bundle. This crack opened to the free face of the specimen.
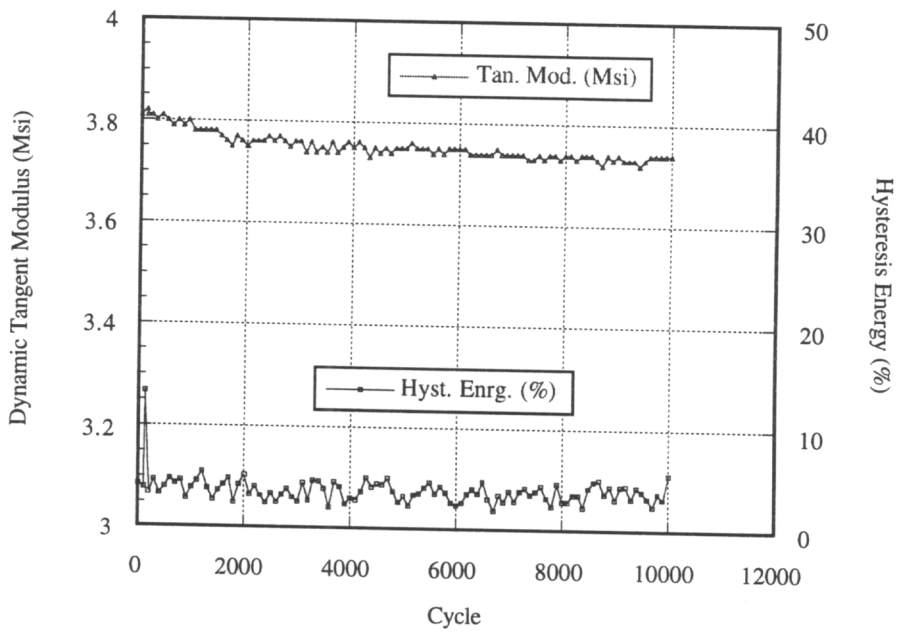
Figure 6.6 - Micrograph and Corresponding Dynamic Tangent Modulus and Normalized Hysteresis Energy Information vs. Cycle Number for an Unnotched LSS Architecture Specimen Tested to Damage Region 1.

Figure 6.7 shows the mechanical response curve and corresponding micrograph of a specimen from damage region two. Three significant energy events occurred, the first of which triggered the stiffening response as was found in some of the specimens tested to failure. Damage mechanisms associated with this behavior were splitting of the braider bundles, disbonding of axial fiber bundles along their length, and kink band formation in the axial bundles. It is important to note the condition of the kink band. The fibers forming the center of the kink band are still intact, and have not been crushed. This is indicative that the kink band had recently formed.

The mechanical response curve and corresponding micrograph from a specimen from damage region three is shown in Figure 6.8. The state of damage is similar to, but advanced from that seen in the micrograph from damage region two. As can be seen in the micrograph from damage region three, splitting in the braider bundles (dark vertical lines) are found in higher densities. In contrast to the newly formed kink band seen in the micrograph from damage region two, the kink band in the axial fiber bundle at the center of the micrograph has progressed to the state where the fibers forming the center of the kink band have been completely crushed (black area in center of micrograph).

The overall unnotched behavior of the LSS architecture was consistent with respect to establishing damage mechanism progressions with increasing numbers of cycles tested. Initial damage modes included splitting of the axial fiber bundles along their length, and

Figure 6.7 - Micrograph and Corrresponding Dynamic Tangent Modulus and Normalized Hysteresis Energy Information vs. Cycle Number for an Unnotched LSS Architecture Specimen Tested to Damage Region 2.
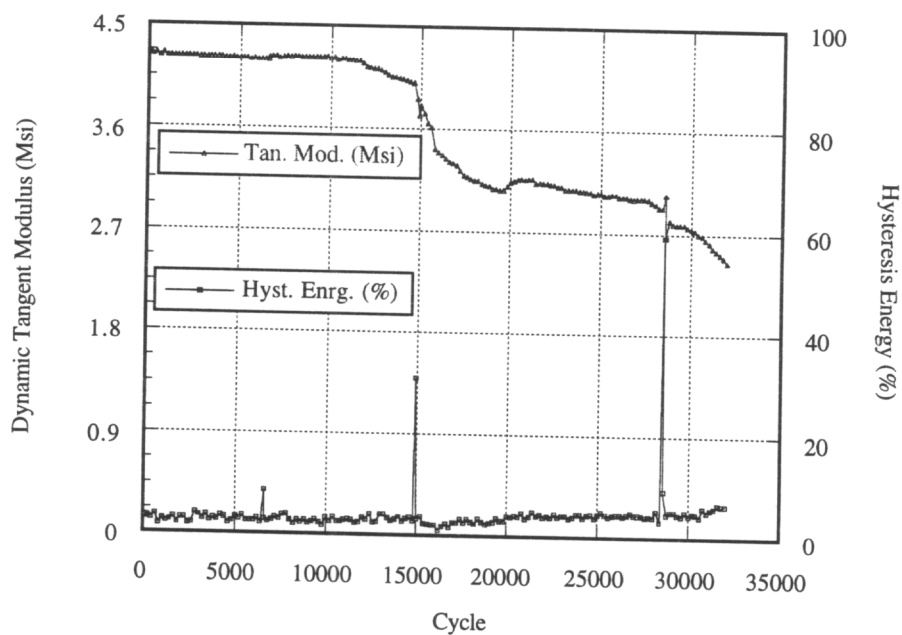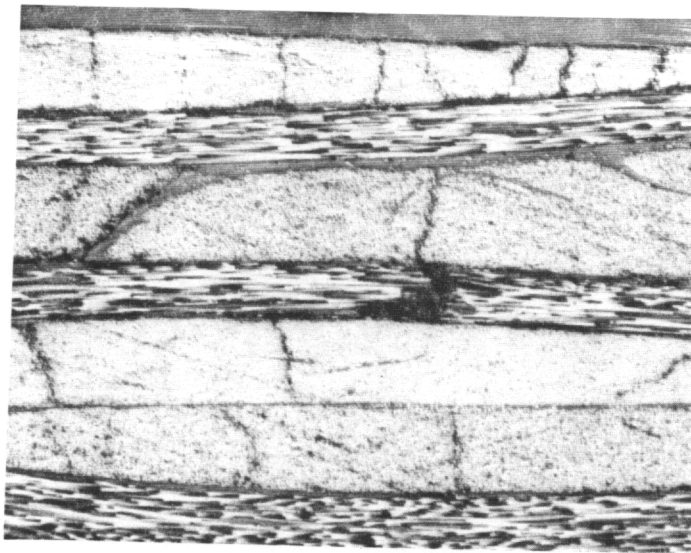
Figure 6.8 - Micrograph and Corrresponding Dynamic Tangent Modulus and Normalized Hysteresis Energy Information vs. Cycle Number for an Unnotched LSS Architecture Specimen Tested to Damage Region 3.

disbonding of the axial fiber bundles from surrounding constituents. In the latter stages of the test, kink band formation in axial fiber bundles was found. After a kink band formed, subsequent cycles crushed the fiber segments in the kink band, and damage to the constituents adjacent to the kink band progressed.

Notched - Notched compression-compression fatigue specimens were tested at the same net stress level as the unnotched specimens. The one inch wide specimens from this architecture contained a 0.25 inch diameter notch in the center of the gage length. This geometry required that the peak load level be 75% of that for the unnotched specimens to yield an equivalent net section stress. This tested the ability of the material system to sustain a stress concentration. All micrographs presented in the following sections show damage regions at the edge of the notch. The viewing angle is from the center of the hole looking toward the free edge of the specimen.

The mechanical response and corresponding micrograph for a notched specimen tested to damage region one is shown in Figure 6.9. The remains of a kink band are shown by the dark gap in the axial fiber bundle which runs horizontally in the micrograph. Also, small areas of disbonding of the axial fiber bundles along their length are seen. Some splitting in the braider bundles was also found. The existence of this kink band is correlated with a large energy event which occurred on the first loading cycle.

Very similar damage states were found in specimens tested to damage region two. The

Figure 6.9 - Micrograph and Corrresponding Dynamic Tangent Modulus and Normalized Hysteresis Energy Information vs. Cycle Number for a Notched LSS Architecture Specimen Tested to Damage Region 1.

mechanical response curve and corresponding micrograph are shown in Figure 6.10. Again, remains of a kink band are found in an axial fiber bundle. The disbonding of the axial fiber bundles along their length is more pronounced as compared to the micrograph of the specimen tested to damage region one. The kink band in the axial fiber bundle is again correlated with a significant energy event which occurred very early in the test.

A very advanced state of damage was found in specimens tested to damage region three. As can be seen in the micrograph in Figure 6.11, the remains of two kink bands are in existence in close proximity to one another. This corresponds directly with the mechanical response curve. The first significant energy event triggered a large decrease in dynamic tangent modulus. Just prior to the stoppage of the test, another significant energy event occurred. Disbonding of the axial fiber bundles along their length is also seen in the micrograph, denoted by the dark lines running along the edges of the axial fiber bundles, which extend horizontally from right to left in the micrograph.

The overall notched fatigue behavior of the LSS architecture was controlled by kink band formation in the axial fiber bundles. Kink bands occurred in all three damage regions, with multiple kink bands occurring in the third damage region. Increased levels of disbonding of the axial fiber bundles from the surrounding constituents was also found as the number of test cycles increased.

Figure 6.10 - Micrograph and Corrresponding Dynamic Tangent Modulus and Normalized Hysteresis Energy Information vs. Cycle Number for a Notched LSS Architecture Specimen Tested to Damage Region 2.

Figure 6.11 - Micrograph and Corrresponding Dynamic Tangent Modulus and Normalized Hysteresis Energy Information vs. Cycle Number for a Notched LSS Architecture Specimen Tested to Damage Region 3.

6.4.2 $[0_{36K}/\pm45_{15K}]_{46\% \, axial}$ (LLS) Architecture

Unnotched - The first ten unnotched specimens were tested to failure in order to establish a relationship between the peak stress level and life. This data is plotted in Figure 6.12 along with a linear fit of the form $y = a + b \log(N)$. The corresponding linear correlation coefficient R was equal to 0.964. The linear correlation coefficient suggests that the data reasonably fits the straight line assumption. However, when the statistical analysis described in section 6.4.1 is completed on the data, the probability that the data matched the linear model was found to be zero. Again, this is not an indication of a poor model, but rather a true picture of the random nature of fatigue testing results. This data was used to determine the peak stress level at which a life of 100,000 cycles might be achieved, in the absence of a better tool. For the LLS architecture, this level was chosen to be 45 ksi.

Generally, there were two characteristic stiffness versus cycle number responses found, both of which are shown in Figure 6.13. The responses are also very similar to those found for the LSS architecture. The first type of response yielded a steadily decreasing stiffness value as the number of cycles increased. Locations where abrupt decreases took place in the stiffness curve were nearly always associated with a significant energy event. Significant energy events also took place randomly throughout the test. The second type of response yielded a relatively constant stiffness response as the number of cycles increased, up to a critical point where a significant energy event triggered a region in
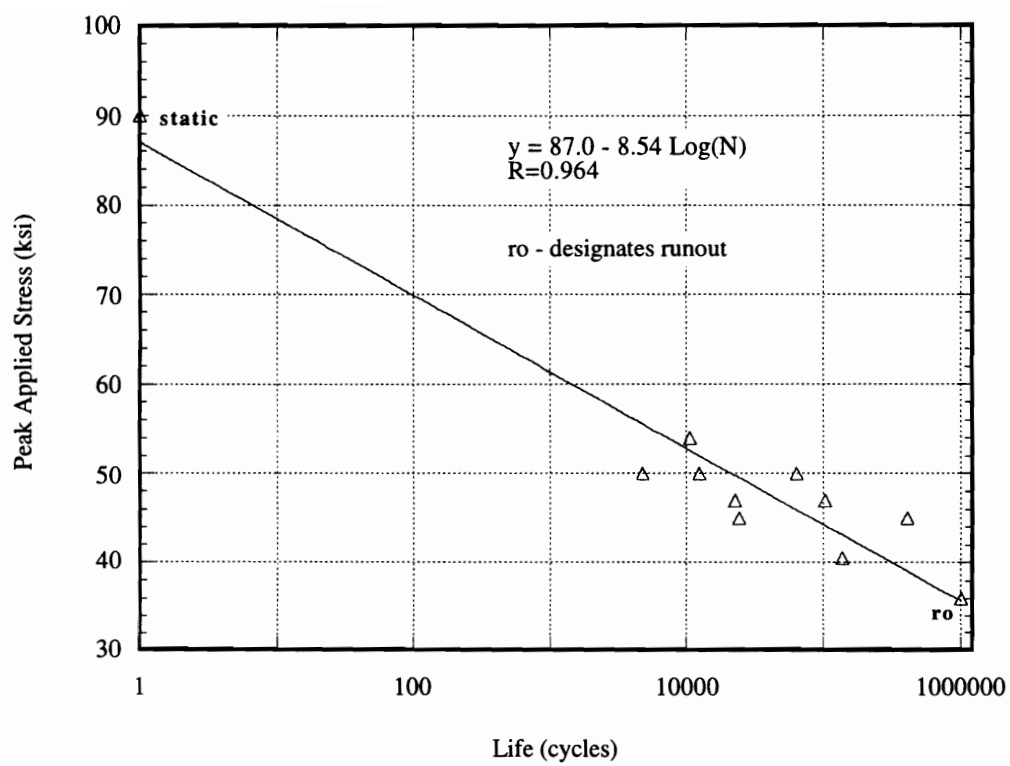
Figure 6.12 - Peak Stress versus Life for Ten Specimens Tested to Ultimate Failure from the LLS Architecture
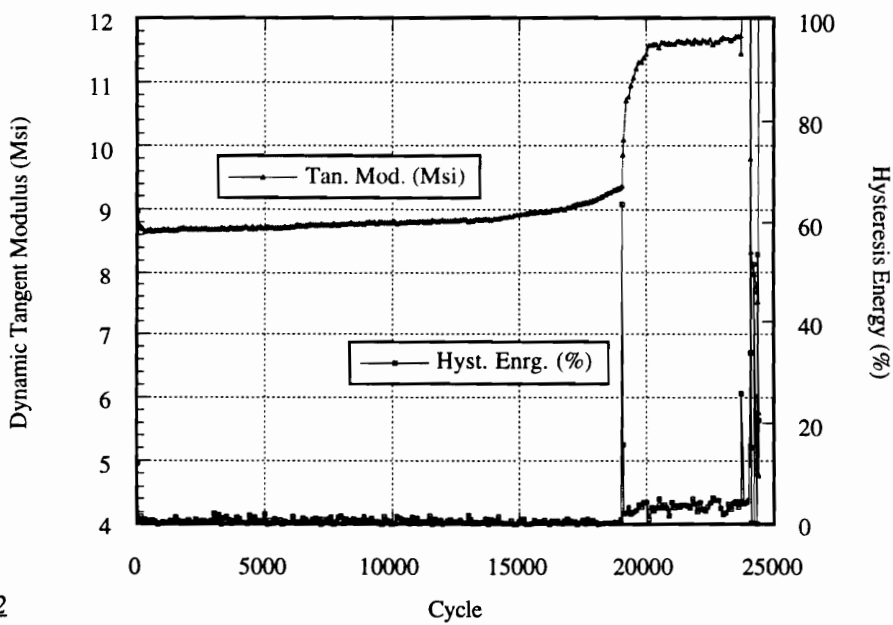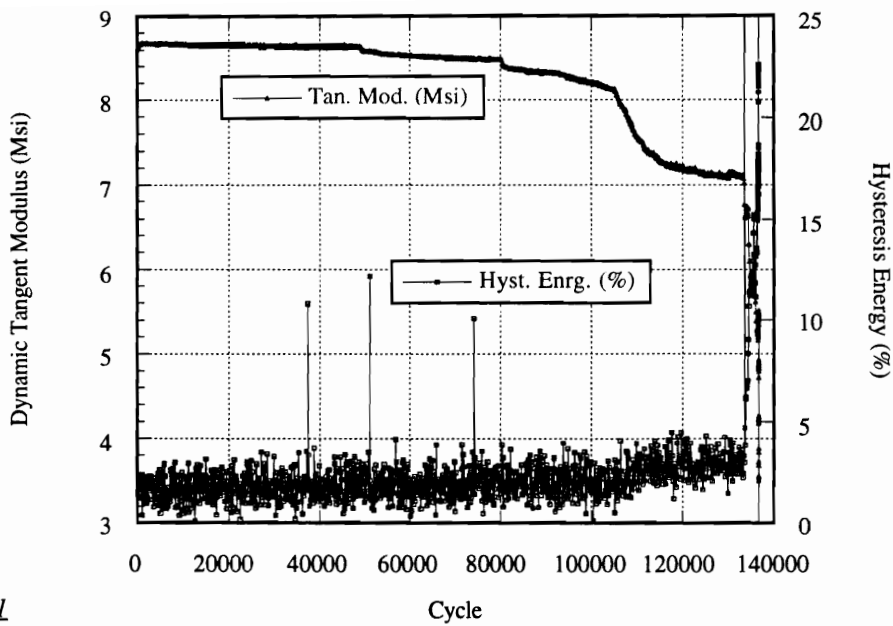
Figure 6.13 - Characteristic Dynamic Tangent Modulus and Normalized Hysteresis Energy versus Cycle Number Graphs for the LLS Architecture.

which the stiffness value increased and became very erratic until failure. The two characteristic responses were not a function of peak applied stress level. Both types of responses were found for the full range of stress levels used.

Information from the first ten specimens tested to failure was used to determine the peak stress level used for the second phase of testing, as well as stopping points for each of the three damage regions described in section 6.3. As previously stated, the peak stress level for the second phase of testing was chosen to be 45 ksi.

The LLS architecture yielded very little damage in the first two regions of the stiffness versus cycle number response. A damage micrograph and corresponding dynamic tangent modulus versus cycle number graph are shown in Figure 6.14. The black segments in the center of the micrograph are a crack which has initiated in a resin rich area. The resin rich area is bounded on the top and bottom by axial fiber bundles, and on the left and right by braider fiber bundles. No significant energy events were detected by the hysteresis energy monitoring, which corresponded with a relatively constant dynamic modulus response. Kink band formation was also absent.

Specimens tested to the second damage region again yielded relatively small amounts of damage. A representative micrograph and corresponding dynamic tangent modulus and hysteresis energy versus cycle number graph is shown in Figure 6.15. An axial fiber runs horizontally through the center of the micrograph. Immediately above the axial fiber
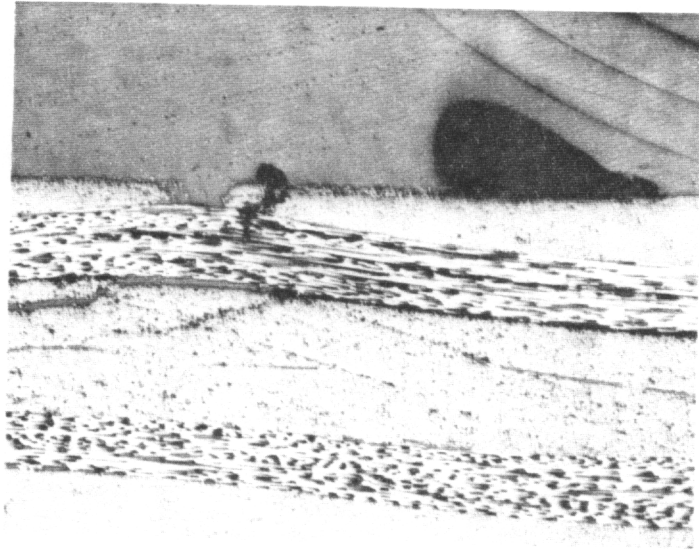
Figure 6.14 - Micrograph and Corresponding Dynamic Tangent Modulus and Normalized Hysteresis Energy Information vs. Cycle Number for an Unnotched LLS Architecture Specimen Tested to Damage Region 1.
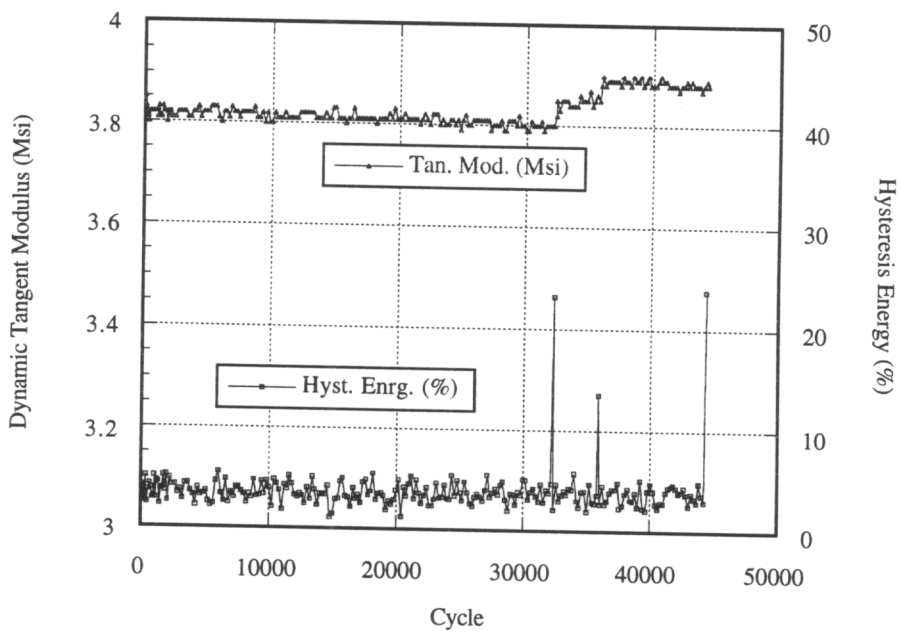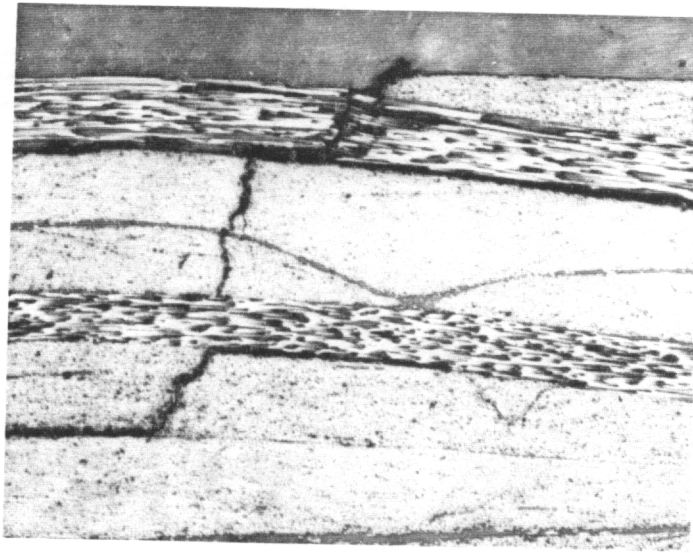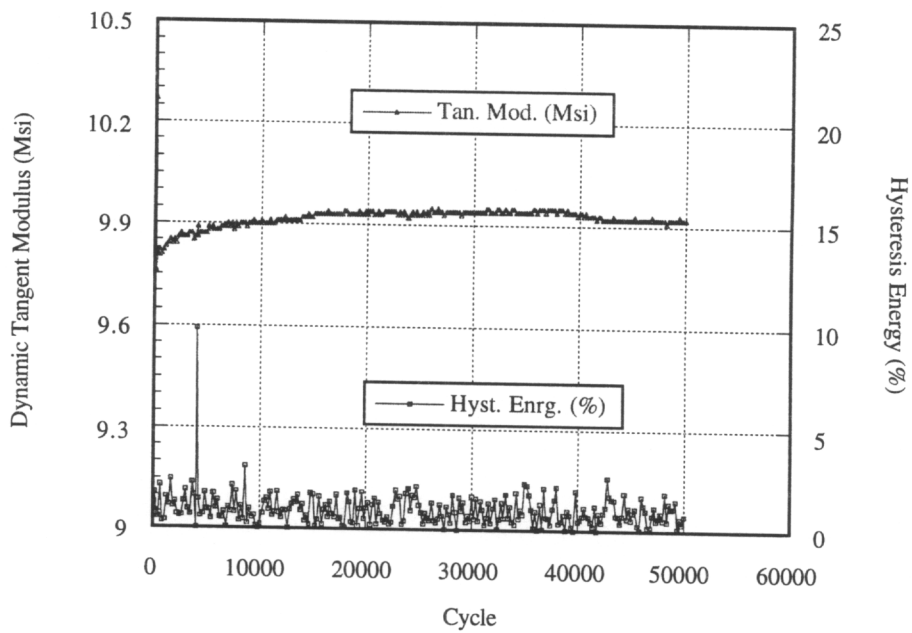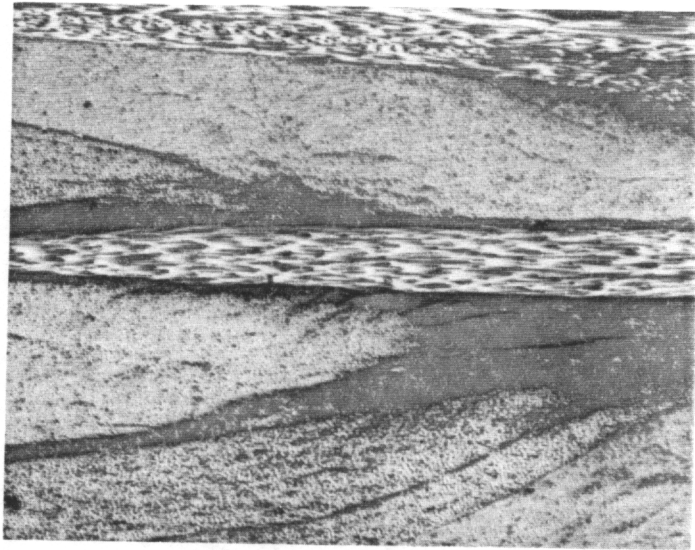
Figure 6.15 - Micrograph and Corresponding Dynamic Tangent Modulus and Normalized Hysteresis Energy Information vs. Cycle Number for an Unnotched LLS Architecture Specimen Tested to Damage Region 2.

bundle, a series of cracks in a resin rich area between the axial fiber bundle and surrounding braider fiber bundles can be seen in the form of short dark lines oriented at approximately 20° above the horizontal. This cracking in resin rich areas was the only type of damage found. The dynamic tangent modulus and hysteresis energy response corresponding to the micrograph indicate one significant energy event, and a slightly increasing dynamic tangent modulus value as the test progressed. Regions of slight dynamic tangent modulus increases were common throughout all testing for the LLS architecture, and are believed to be a true response of the material system. No kink bands were found in this damage region. Most major damage events in the LLS architecture took place in the third damage region.

A micrograph and corresponding dynamic tangent modulus and hysteresis energy versus cycle number graph for damage region three is shown in Figure 6.16. Multiple kink bands can be seen in the micrograph. The three arched segments running across the micrograph from left to right are actually all constituents of the same axial fiber bundle. The uppermost segment contains a kink band which is severely degraded, while the center segment contains a newly formed kink band seen on the far right of the micrograph. This type of axial bundle configuration was found in several locations throughout the LLS architecture. It is a result of winding together several smaller fiber bundles to make one large bundle. In several locations, the individual fiber bundles did not mesh together, and actually remained as several smaller bundles wound in a spiral fashion. This is believed to
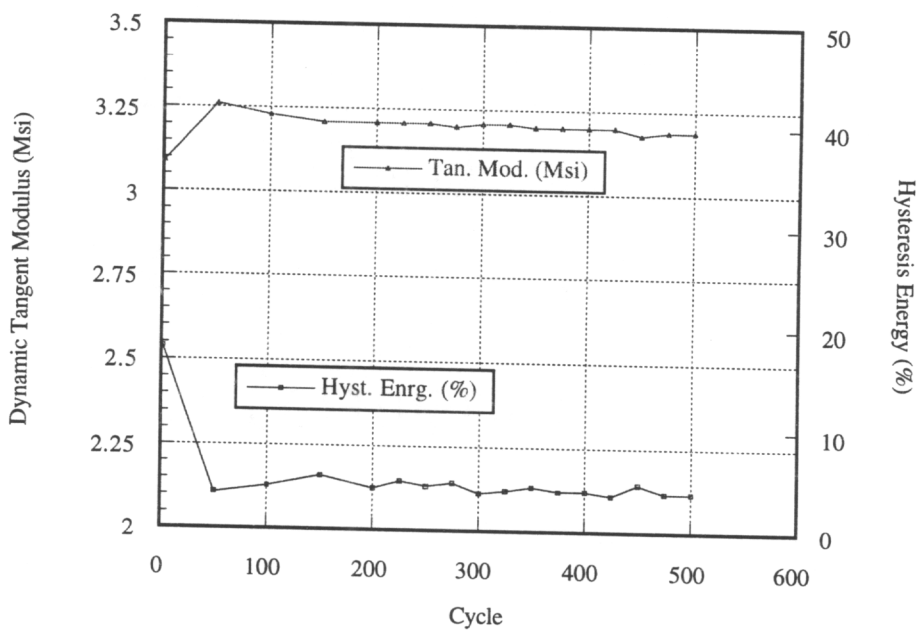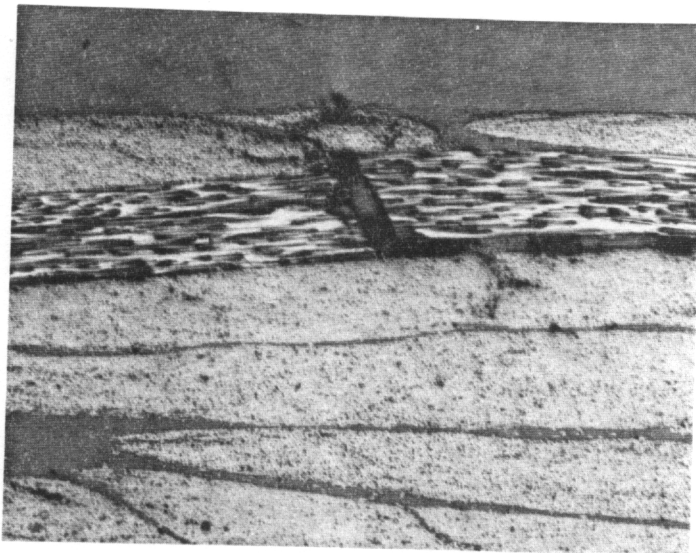
Figure 6.16 - Micrograph and Corresponding Dynamic Tangent Modulus and Normalized Hysteresis Energy Information vs. Cycle Number for an Unnotched LLS Architecture Specimen Tested to Damage Region 3.

be a major contributor to the extreme variability found in this architecture. The dynamic tangent modulus curve indicated a steadily decreasing value up to catastrophic failure. Five significant hysteresis energy events occurred throughout the test, with those of the largest magnitude occurring just prior to catastrophic failure.

The overall unnotched compression-compression fatigue behavior of the LLS architecture was reasonably consistent from a damage mechanism versus point in life perspective. Increasing damage levels corresponded to longer lives in all of the six specimens tested. Kink band formation was found to occur near the end of the life of the specimen. No kink bands were found in the first two damage regions. Significant energy events were found to occur throughout the test. Some were correlated with matrix cracking only. The magnitude of the event was not enough to distinguish between matrix cracking or kink band formation in axial fiber bundles.

Notched - Introduction of the notch into the LLS architecture resulted in an extremely inconsistent response to a stress concentration. Increased damage levels did not directly correspond to an increased number of cycles tested. The number of test cycles required for each damage level varied significantly. Contrary to the trend found in the unnotched specimens, increased damage levels did not directly correspond to longer tests. Therefore, more attention was given to the shape of the dynamic tangent modulus and hysteresis energy information than to the number of cycles required to reach that damage state. All

micrographs presented in the following section are from the vantage point of looking from the center of the hole outward to the inside edge of the hole, perpendicular to the line of loading.

The dynamic tangent modulus and hysteresis energy response graph for a specimen tested to damage region one is shown in Figure 6.17, along with a schematic showing the corresponding damage location. Splitting in the axial fiber bundles was found to initiate around the edges of the notch, with splits along the side of the notch being much longer than those found along the upper and lower surfaces of the notch. One significant energy event occurred on the first cycle of the test, however, no damage other than the splitting in the axial fiber bundles was found.

Splitting initiated in the axial fiber bundles around the edges of the notch in a specimen tested to damage region two, and a kink band formed in an axial fiber bundle at the edge of the notch. The dynamic tangent modulus and hysteresis energy information versus cycle number is shown in Figure 6.18, along with a corresponding micrograph. Some small fiber segments can be seen in the center of the kink band along with disbonding of the axial fiber bundle from the surrounding braider fiber bundles and resin rich areas. One significant energy event took place immediately prior to test stoppage, and was accompanied by a large decrease in dynamic tangent modulus.

Progression of those damage types found in the first two damage regions was also

Figure 6.17 - Schematic and Corresponding Dynamic Tangent Modulus and Normalized Hysteresis Energy Information vs. Cycle Number for a Notched LLS Architecture Specimen Tested to Damage Region 1.
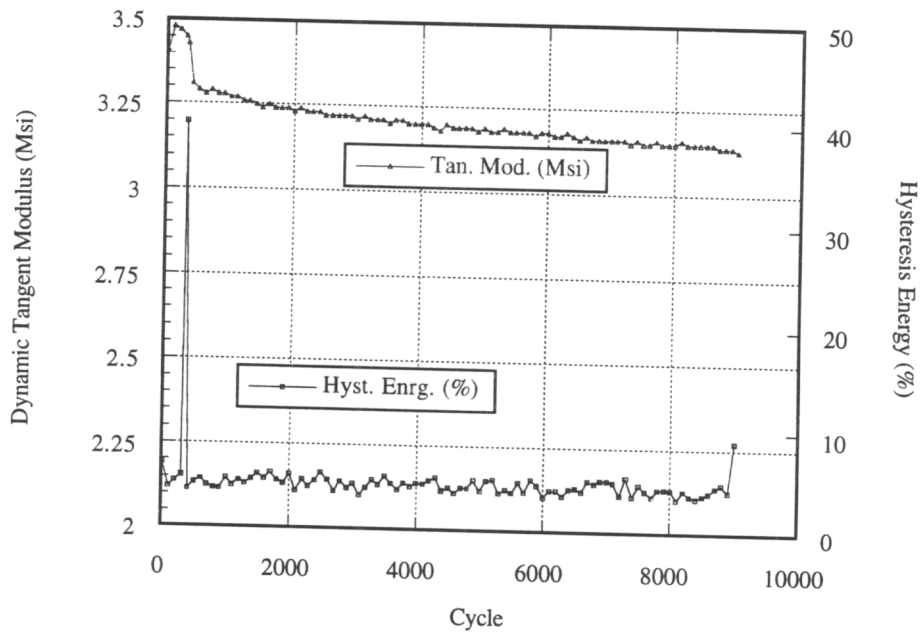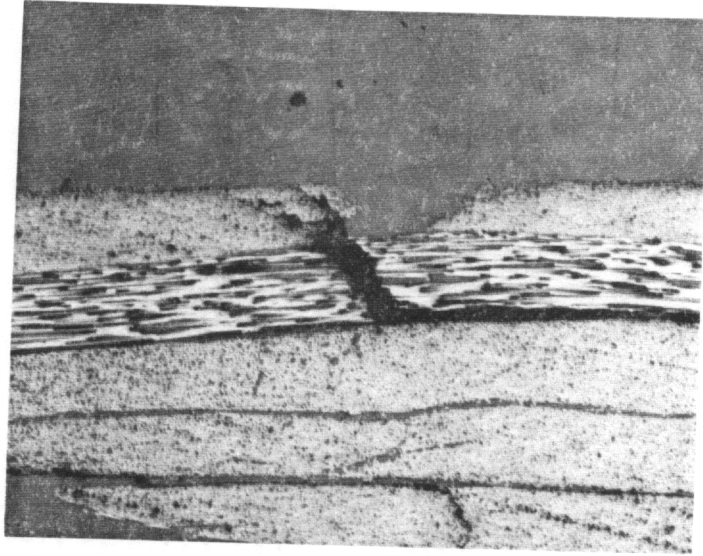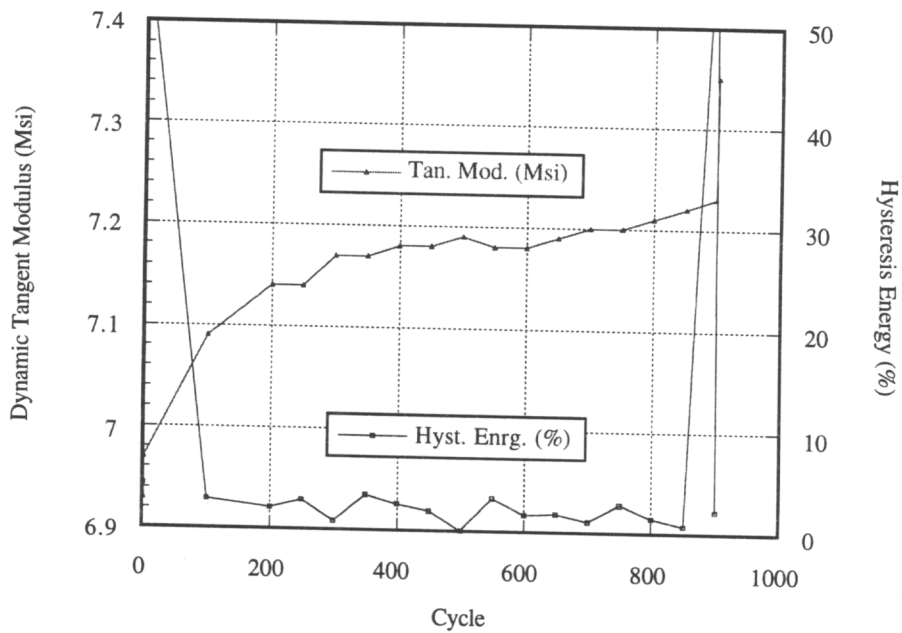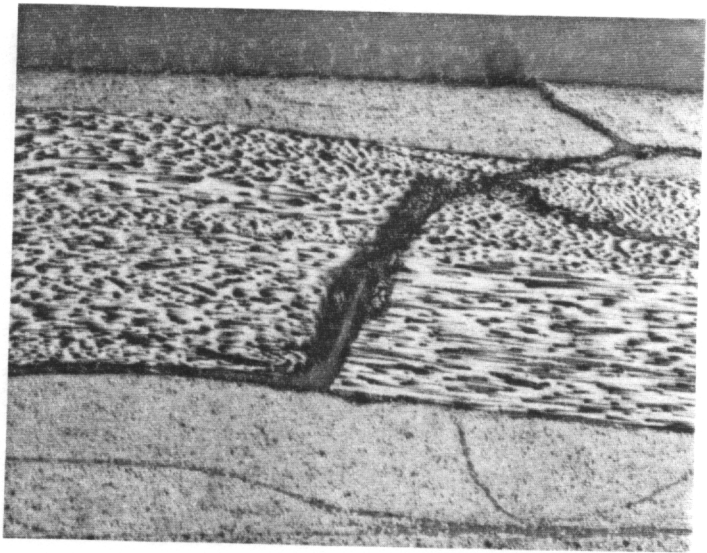
Figure 6.18 - Micrograph and Corresponding Dynamic Tangent Modulus and Normalized Hysteresis Energy Information vs. Cycle Number for a Notched LLS Architecture Specimen Tested to Damage Region 2.
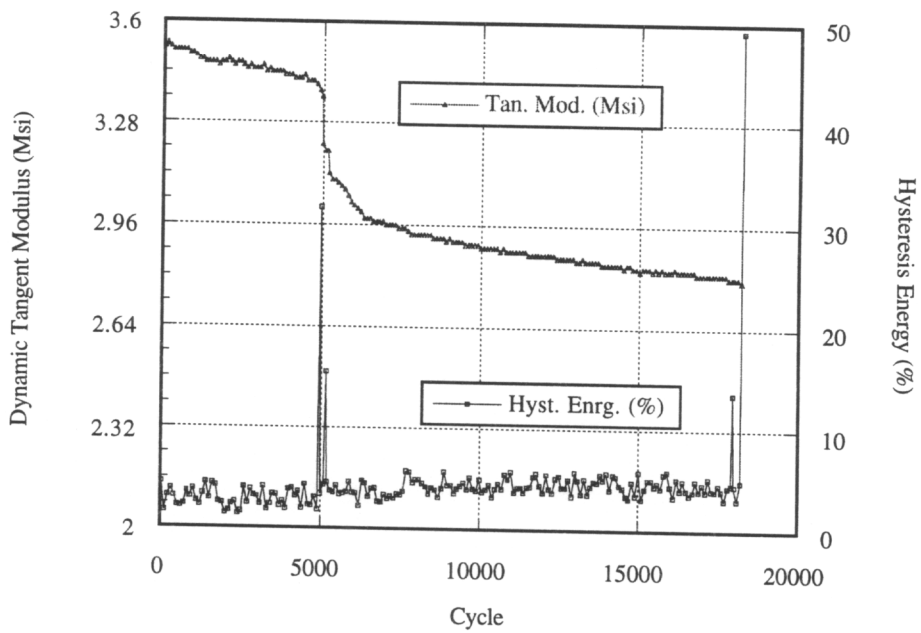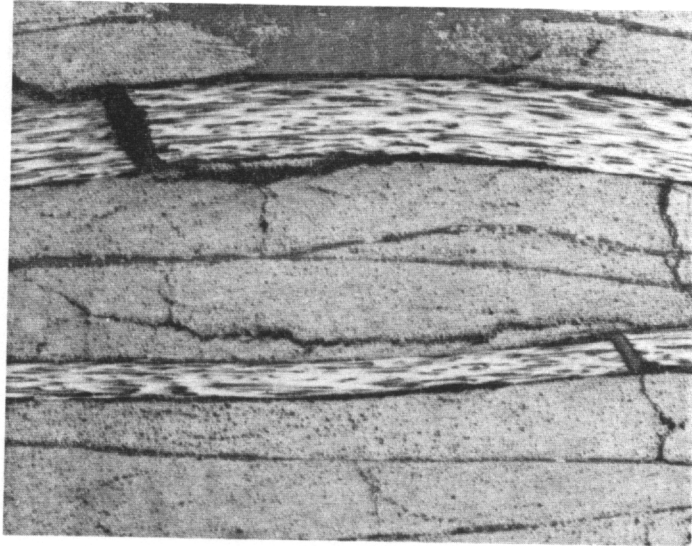
found in a specimen tested to damage region three. A micrograph and corresponding dynamic tangent modulus and hysteresis energy versus cycle number is shown in Figure 6.19. A newly formed kink band is seen in the upper-right corner of the micrograph, along with large amounts of splitting in the axial fiber bundle. Disbonding of the axial fiber bundle from the surrounding braider fiber bundles is also seen. Not shown in the damage micrograph is remains of a second kink band. Some small fiber segments can be seen in the split running along the length of the axial fiber bundle. These fiber segments are fragments which propagated from the first kink band into the split along the axial fiber bundle. The existence of the two kink bands found in the specimen is accompanied by two groups of significant energy events seen in the corresponding specimen response graph. The first group occurred approximately one third of the way through the test, and was associated with a large decrease in dynamic tangent modulus. The second group of significant energy events occurred just prior to test stoppage.

The overall notched compression-compression fatigue behavior of the LLS architecture was not consistent from a damage mechanism versus point in life perspective. Increased damage levels did not correspond to longer lives. While an increasing trend in progression of damage mechanisms was established, the number of cycles required to reach each of the progressive damage states was inconsistent. Splitting of the axial fiber bundles around the edges of the notch was found in damage region one. Splits along the sides of the notch were much longer than those seen on the top and bottom of the notch. Kink band
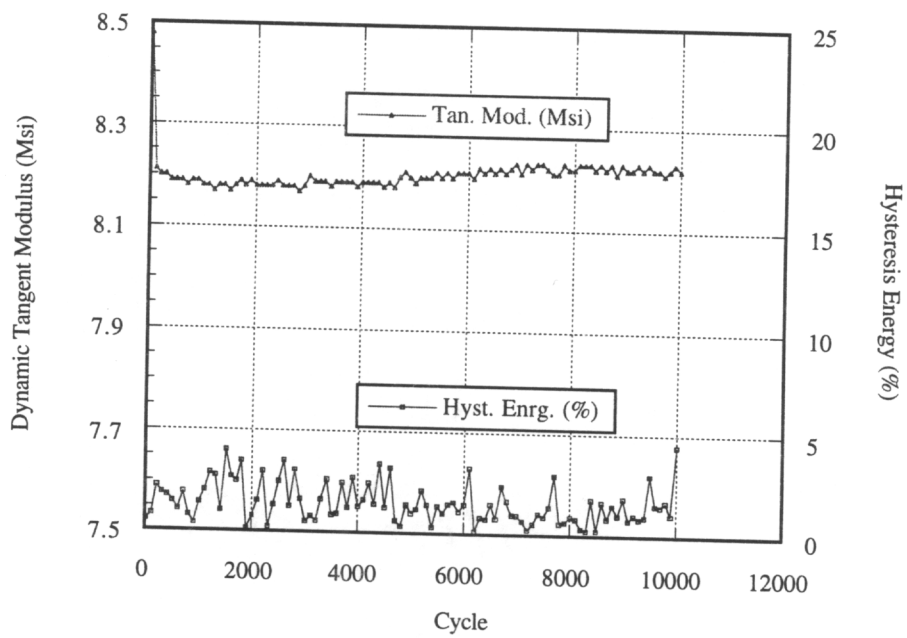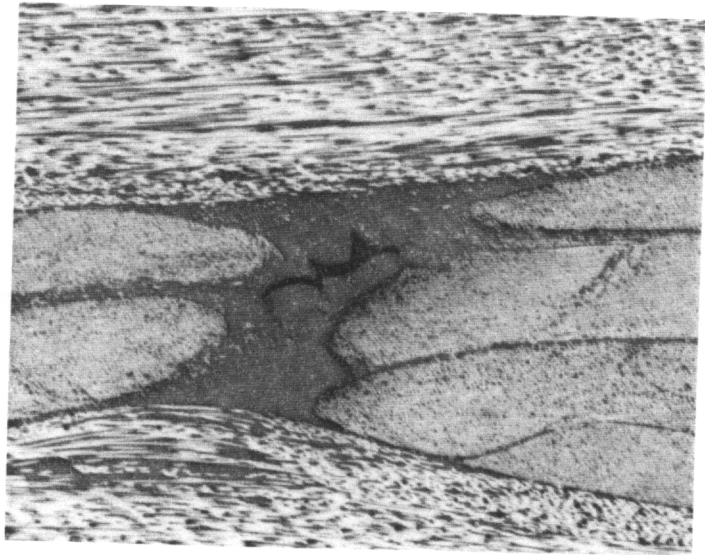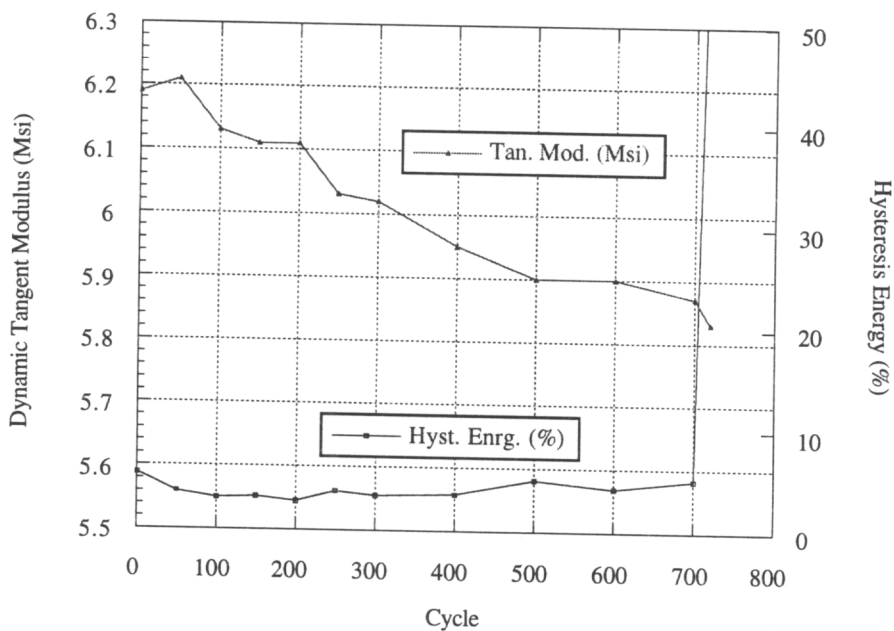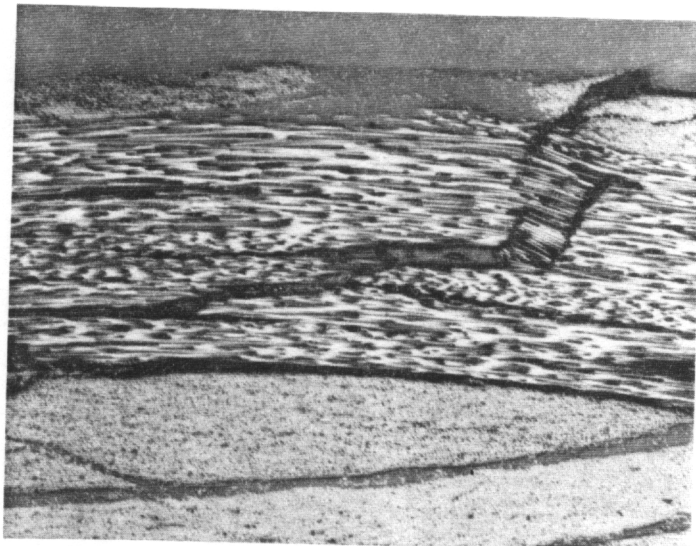
Figure 6.19 - Micrograph and Corresponding Dynamic Tangent Modulus and Normalized Hysteresis Energy Information vs. Cycle Number for a Notched LLS Architecture Specimen Tested to Damage Region 3.

formation was found in damage region two, located in the axial bundles at the sides of the notch. Disbonding of the axial fiber bundles from the surrounding constituents was also found. Damage mechanisms found in damage region three were similar to those found in damage region two but in a much more advanced state. Multiple kink bands were found, along with longer disbonds along the axial fiber bundles, and splits along the length of the axial fiber bundles.

6.4.3 $[0_{30K}/\pm70_{6K}]_{46\% \ axial}$ (SLL) Architecture

Unnotched - The first ten unnotched specimens were tested to failure in order to establish a relationship between the peak stress level and life. This data is plotted in Figure 6.20 along with a linear fit of the form $y = a + b \log(N)$. The corresponding linear correlation coefficient R was equal to 0.650. The linear correlation coefficient suggests that the data does not fit the straight line assumption. This also agrees with the statistical analysis described in section 6.4.1 which yielded the probability that the data matched the linear model was zero. Again, this is not an indication of a poor model, but rather a true picture of the random nature of fatigue testing results. This data was used to determine the peak stress level at which a life of 100,000 cycles might be achieved, in the absence of a better tool. For the SLL architecture, this level was initially chosen to be 66.5 ksi. However, the level was decreased to 65.5 ksi due to catastrophic failures at very low cycle numbers. For notched specimens the peak applied stress level had to be reduced to 60 ksi in order to obtain significant specimen lives.
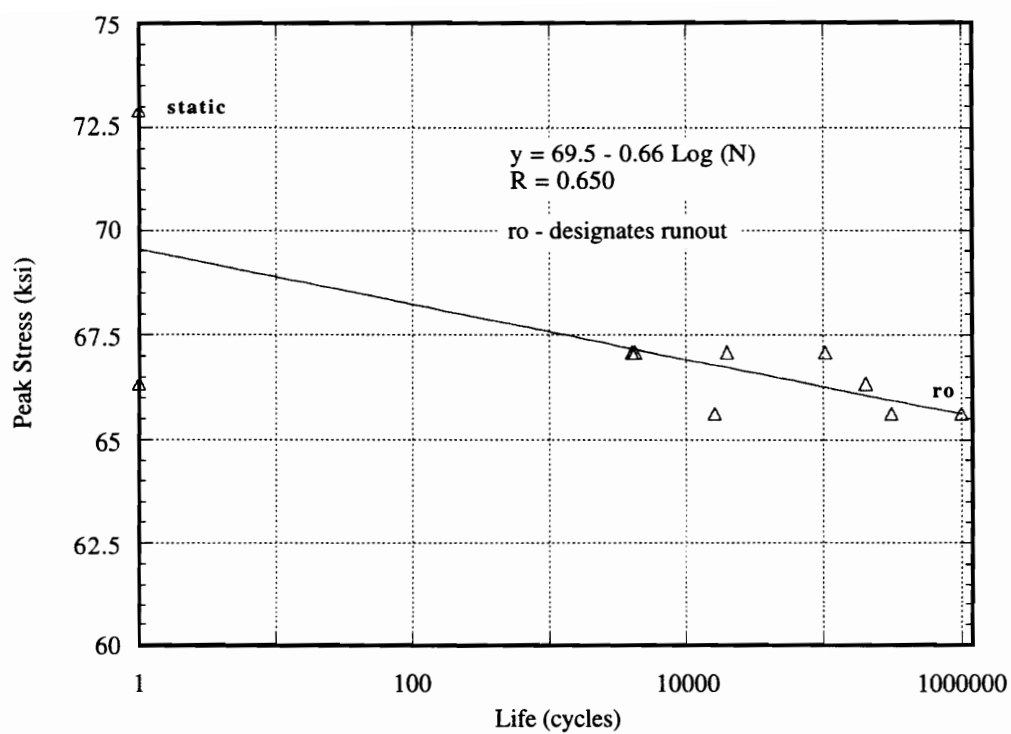
Figure 6.20 - Peak Stress versus Life for Ten Specimens Tested to Ultimate Failure from the SLL Architecture.

Generally, there was one characteristic stiffness versus cycle number response found for the SLL architecture, which is shown in Figure 6.21. The dynamic tangent modulus versus cycle number graph showed a slightly increasing trend until a significant energy event triggered a region in which the stiffness value increased and became very erratic until failure. This is similar to the second type of behavior seen in the LLS architecture. This type of response was found over the complete range of applied stress, which corresponded to specimen lives ranging from 4000 cycles to nearly 100,000 cycles.

Kink band formation was dominant in all damage regions of the SLL architecture. A micrograph and corresponding dynamic tangent modulus and hysteresis energy versus cycle number graph from the first damage region is shown in Figure 6.22. Some short fiber segments can be seen in the center of the degraded kink band. Splits running along the edges of the axial fiber bundle have propagated from the location of the kink band, along the interface of the axial fiber bundle and its surrounding constituents. Most damage, however, is localized around the kink band. The corresponding dynamic tangent modulus and hysteresis energy versus cycle number graph is very erratic, and contains only five data points for each curve. This is because the save interval for the data acquisition program is based on the number of elapsed cycles. The test was expected to span several hundred cycles, and therefore gather a reasonable number of data points. This was not the case due to the inability of the specimens to sustain the applied cyclic load level, and is a problem which stems from the scatter in the data from the ten specimens
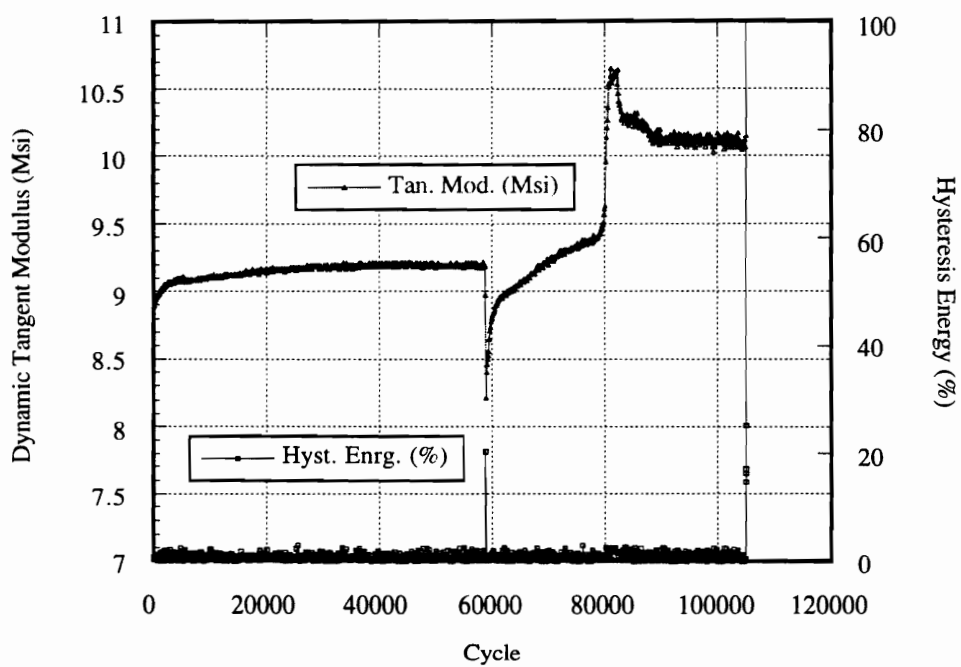
Figure 6.21 - Characteristic Dynamic Tangent Modulus and Normalized Hysteresis Energy versus Cycle Number Graph for the SLL Architecture.
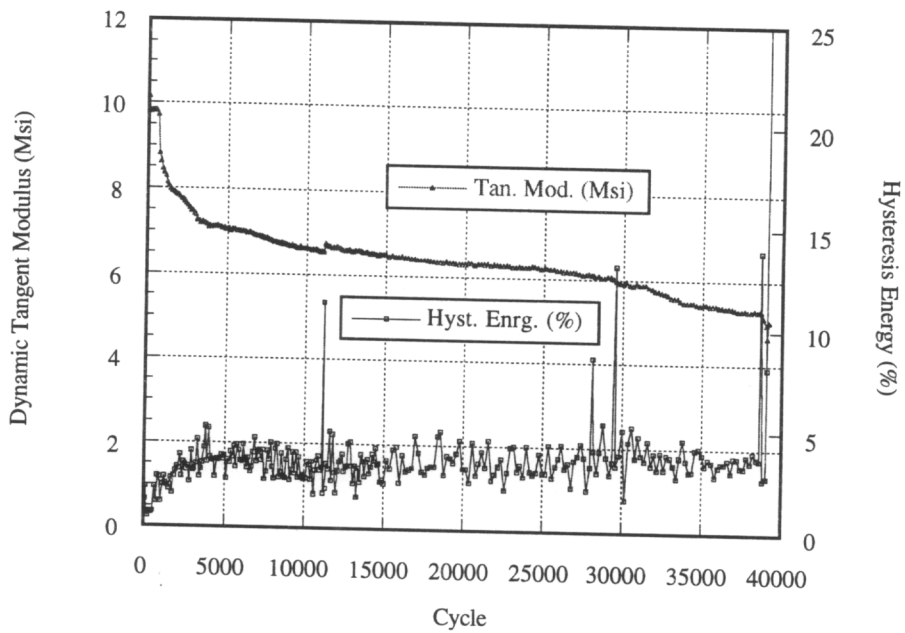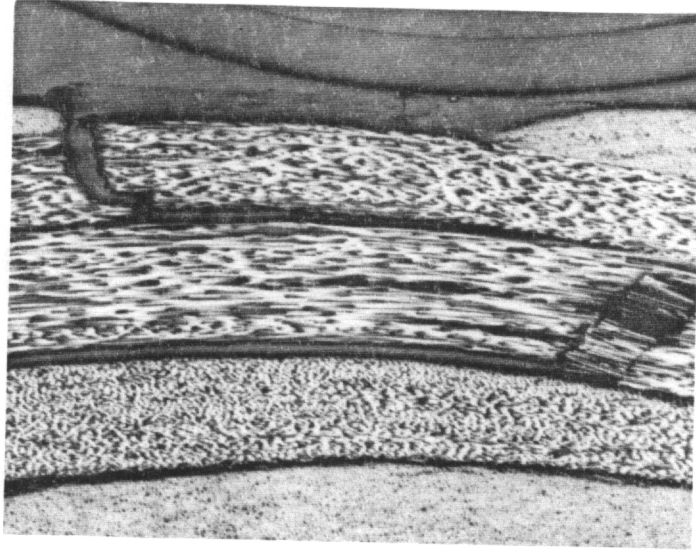
Figure 6.22 - Micrograph and Corresponding Dynamic Tangent Modulus and Normalized Hysteresis Energy Information vs. Cycle Number for an Unnotched SLL Architecture Specimen Tested to Damage Region 1.

tested to failure. The important point to note is the significant energy event which took place on the seventh cycle that is directly related to the kink band found in the axial fiber bundle.

Kink band formation was also found in a specimen tested to the second damage region. The location of the kink band is seen in the micrograph shown in Figure 6.23. The corresponding dynamic tangent modulus and hysteresis energy versus cycle number information is also shown. The kink band shown in the micrograph has degraded to the point that none of the fiber segments initially formed in the band are left in the local area. The dark lines running horizontally across the micrograph are disbonds running along the interface between the axial fiber bundle and the surrounding constituents. These disbonds are much longer than those found in damage region one. The corresponding specimen response information indicates one major energy event which occurred on the first cycle of the test, and another which occurred just prior to test stoppage. Damage resulting from the formation of the kink band is contained within the axial fiber bundle. Surrounding constituents were not damaged. The dynamic tangent modulus and hysteresis energy versus cycle number information showed a slightly decreasing dynamic stiffness trend with increasing cycles up to the point where the test was stopped.

Types of damage found in the third damage region were an advanced state of damage formed in region two. The axial fiber bundle in the micrograph shown in Figure 6.24

Figure 6.23 - Micrograph and Corresponding Dynamic Tangent Modulus and
Normalized Hysteresis Energy Information vs. Cycle Number for an Unnotched SLL
Architecture Specimen Tested to Damage Region 2.
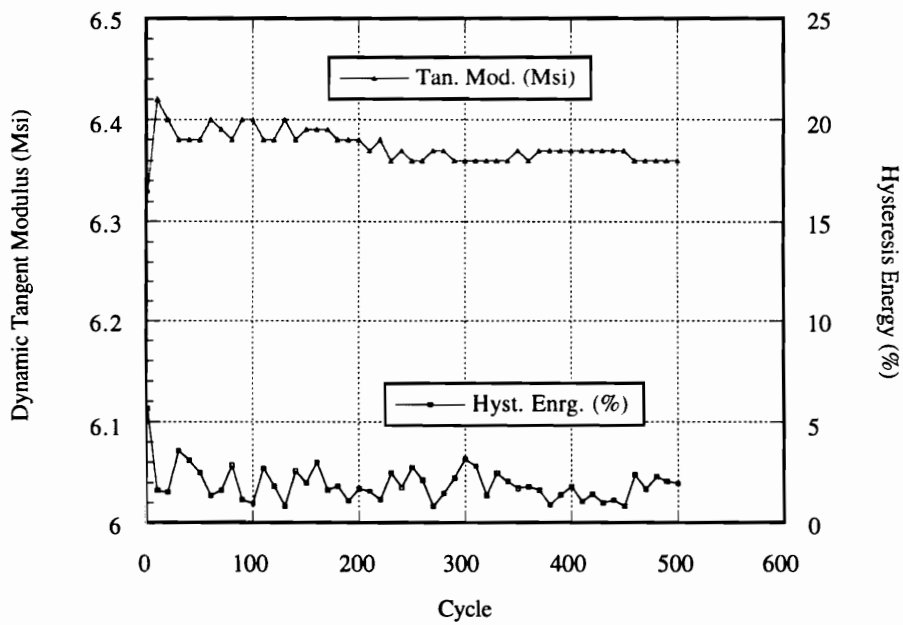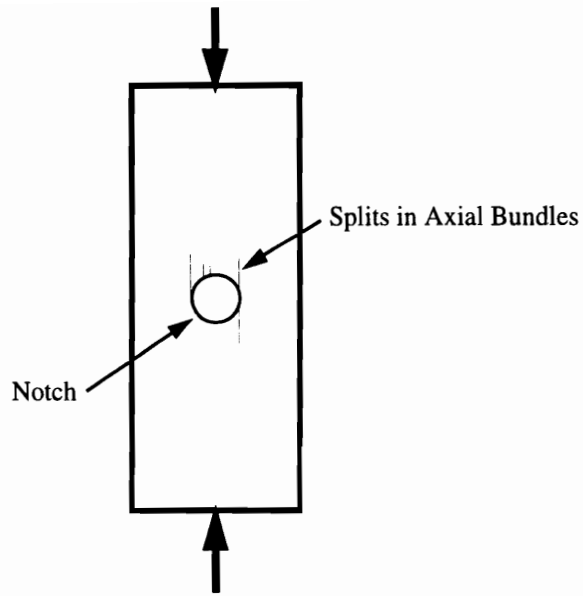
Figure 6.24 - Micrograph and Corresponding Dynamic Tangent Modulus and Normalized Hysteresis Energy Information vs. Cycle Number for an Unnotched SLL Architecture Specimen Tested to Damage Region 3.

contains the remains of a kink band indicated by the solid grey region oriented at an angle to the fiber bundle running from left to right in the micrograph. Splits running along the interface of the axial fiber bundle were found like those seen in the specimen from damage region two. A split running along the center of the axial fiber was also found, along with cracks in the resin rich areas around the kink band location. The hysteresis energy versus cycle number information indicated a one major energy event in initial portion if the test. No other significant energy events took place until the latter stages of the test. The dynamic tangent modulus showed a slightly decreasing trend up to the latter stages of the test. Just prior to test stoppage, several significant energy events occurred, and were accompanied by a very large decrease in dynamic stiffness.

The overall unnotched compression-compression fatigue response of the SLL architecture was very inconsistent from a damage mechanism versus point in life perspective. Longer lives did not correspond to increased damage levels. While an increasing trend in progression of damage mechanisms was established, the number of cycles required to reach each of the progressive damage states was inconsistent. Kink band formation in the axial fiber bundles was found in all three damage regions. The damage progressed from initial formation of the kink band, to degradation of the kink band and disbonding of the axial fiber bundle from the surrounding constituents. This was followed by cracking in the resin rich areas surrounding the area of the degraded kink band, and lengthening of the splits running along the outer edges of the axial fiber bundle.

Monitoring of the dynamic tangent modulus showed a slightly decreasing trend with increasing cycles contrary to the first ten specimens tested to failure which showed a slightly increasing trend. Significant energy events occurred very early in each of the tests, and were associated with kink bands in each case. Damage in the surrounding constituents in the severe damage states was associated with several significant energy events which occurred just prior to test stoppage.

Notched - Introduction of the notch into the SLL architecture resulted in the inability of the architecture to sustain a stress concentration. As was previously mentioned, the peak applied stress level had to be reduced from the levels used for testing the unnotched specimens in order to obtain test durations long enough to yield adequate specimen response information. Even at the reduced applied stress level, the test durations were very short. The longest test lasted only 6500 cycles before it had to be stopped to prevent catastrophic failure. There was no correlation found in the notched specimens between the number of cycles tested and the corresponding damage state. Because of the random response of the notched specimens from this architecture, data from the three damage regions mentioned in section 6.3 will not be presented. Instead, a specimen containing initial damage and a specimen containing progressed damage are presented, as this is the best conclusion which can be drawn from the erratic specimen responses.

Initial damage in the notched SLL specimens was in the form of kink band formation

at the edges of the notch. A micrograph showing a kink band in an axial fiber bundle is shown in Figure 6.25. Some pieces of individual fibers are still in the kink band region, indicating that the kink band was indeed newly formed. The axial fiber bundle in which the kink band formed had not yet began to disbond from its surrounding constituents. This kink band corresponded with one major energy event which occurred on the 35th cycle, with the test being stopped on the 45th cycle. The corresponding dynamic tangent modulus and hysteresis energy information is not shown, as only five data points were recorded before the test was stopped.

In advanced damage states, multiple kink bands were found to occur. In some cases, the kink bands formed on opposite edges of the notch, while in other cases, both kink bands formed on the same side of the notch. When the kink bands formed on opposite edges of the notch, two separate major energy events were detected. When the kink bands formed on the same edge of the notch, only one major energy event was detected. A case where both kink bands formed on the same side of the notch is shown in Figure 6.26, along with the corresponding dynamic tangent modulus and hysteresis energy information. It is interesting to note that one kink band has no remains of fiber pieces which is indicated by the solid grey region between the ends of the axial fiber bundle, while the other kink band has numerous pieces of individual fibers, indicated by the dotted region between the ends of the axial fiber bundle. This indicates that the kink bands did not form at the same time. While the time between the formation of one kink band and the

Figure 6.25 - Micrograph and Corresponding Dynamic Tangent Modulus and Normalized Hysteresis Energy Information vs. Cycle Number for a Notched SLL Architecture Specimen Containing an Initial Damage State.

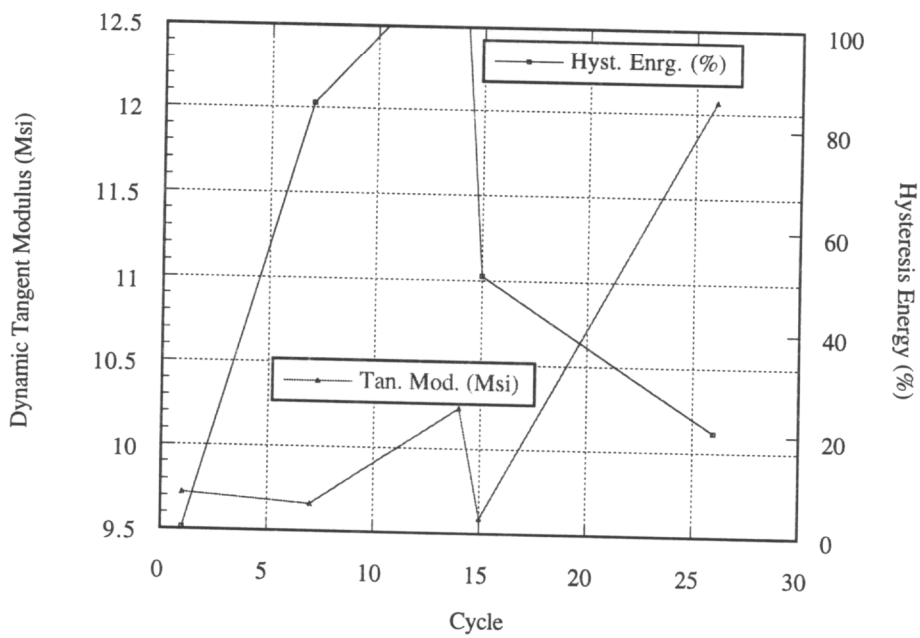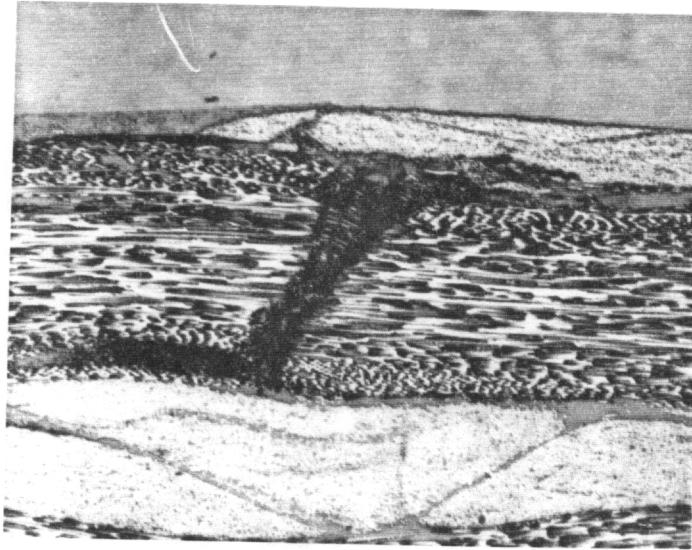Figure 6.26 - Micrograph and Corresponding Dynamic Tangent Modulus and Normalized Hysteresis Energy Information vs. Cycle Number for a Notched SLL Architecture Specimen Containing a Progressed Damage State.

other could not be determined, it is definite that the kink bands did not form on the same cycle. A large crack is also present which runs from the kink band in the first axial bundle to the edge of the second axial fiber bundle. The crack extends along the edge of the second axial fiber bundle to the location of the kink band. Based on the order of kink band formation, it is most likely that the crack originated at the edge of the kink band which formed first, and propagated to the edge of the axial fiber bundle which contained the kink band which formed second.

The overall notched compression-compression fatigue behavior of the SLL architecture was extremely inconsistent. A progression of damage mechanisms was not completely established. Instead, two damage states were presented which were an initial state and a very progressed state of damage. Kink bands were found to form in the first few cycles of the test. As the damage state progressed, multiple kink bands were found. When kink bands occurred on the same side of the notch, only one major energy event was detected. When the kink bands occurred on opposite sides of the notch, two major energy events were detected. Even with reliable test specimen monitoring methods, data from the notched SLL architecture specimens were very inconsistent in nature.

6.4.4 $[0_{75K}/\pm70_{15K}]_{46\% \, axial}$ (LLL) Architecture

Unnotched - The first ten unnotched specimens were tested to failure in order to establish a relationship between the peak stress level and life. This data is plotted in Figure
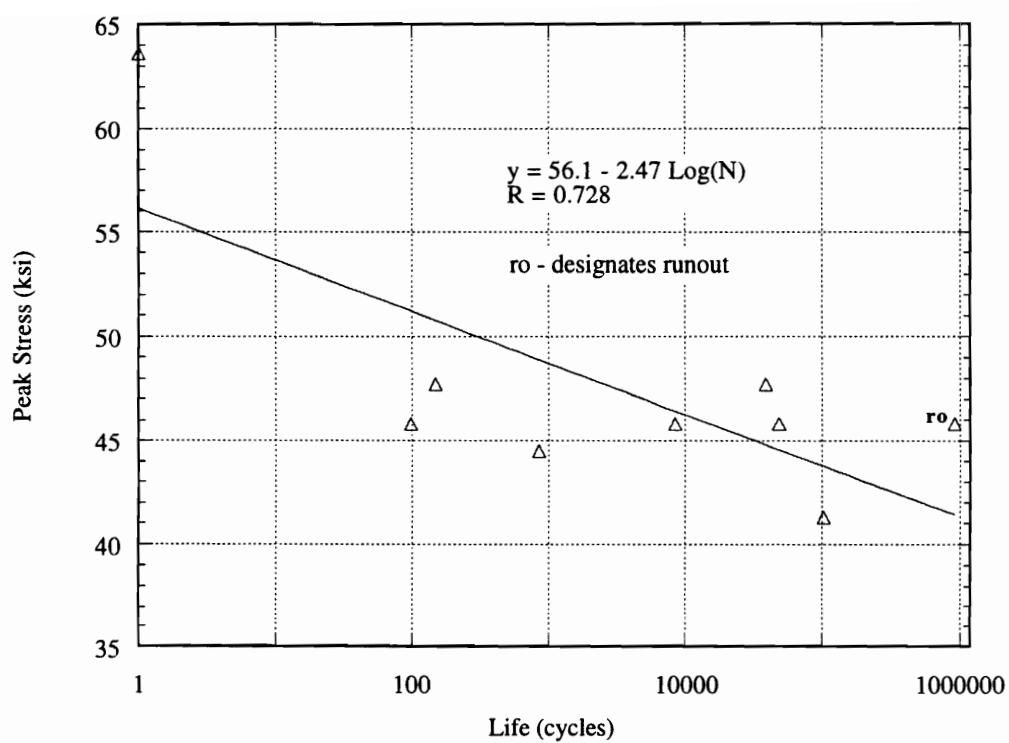
Figure 6.27 - Peak Stress versus Life for Ten Specimens Tested to Ultimate Failure from the LLL Architecture.

6.27 along with a linear fit of the form y = a + b log(N). The corresponding linear correlation coefficient was R was equal to 0.728. This coefficient suggests that the data does not fit the straight line assumption. This also agrees with the statistical analysis described in section 6.4.1 which yielded the probability that the data matched the linear model was zero. This is not an indication of a poor model but rather a true indication of the random nature of the fatigue testing results. This data was used to determine the peak applied stress level at which a specimen life of 100,000 cycles might be achieved. For the LLL architecture, this level was chosen to be 41.3 ksi.

There was no characteristic stiffness versus cycle number response found for the LLL architecture. Dynamic tangent modulus versus cycle number information yielded increasing, decreasing, and flat trends. Major energy events occurred throughout the tests, and ranged in number from two to 26 events. Still, an attempt was made to test the last six specimens in groups of two to initial, intermediate, and near failure damage levels.

Because of the random nature of the specimen responses from the LLL architecture, only two damage levels were able to be determined. The first level contains initial damage mechanisms, while the second level contains damage mechanisms which occurred just prior to ultimate failure. A micrograph and corresponding dynamic tangent modulus and hysteresis energy versus cycle number information is shown in Figure 6.28 from a specimen containing initial damage. A crack in the braider bundles was found indicated by
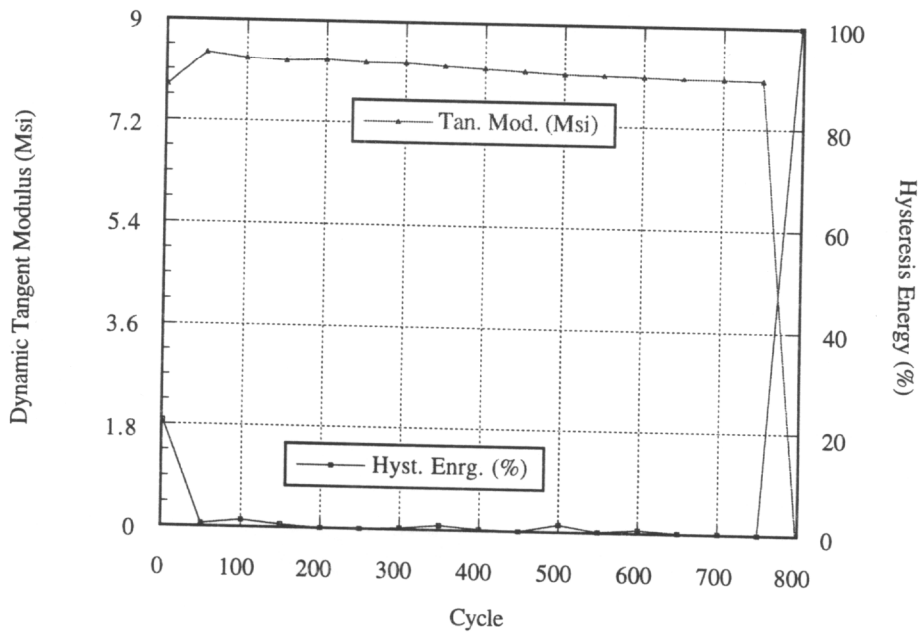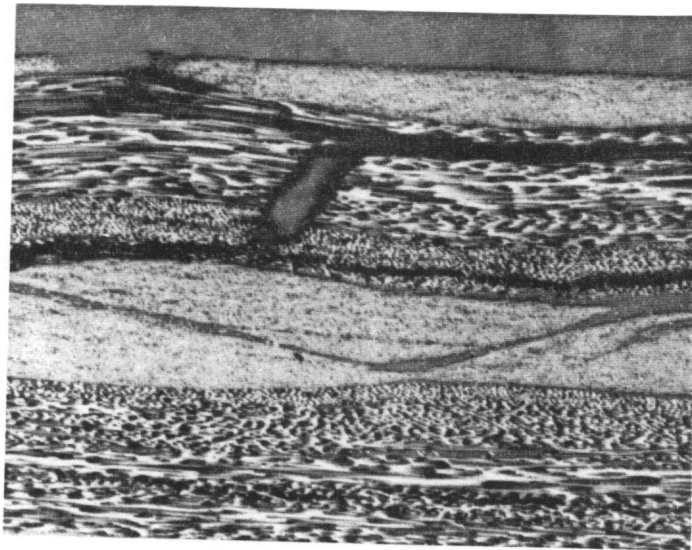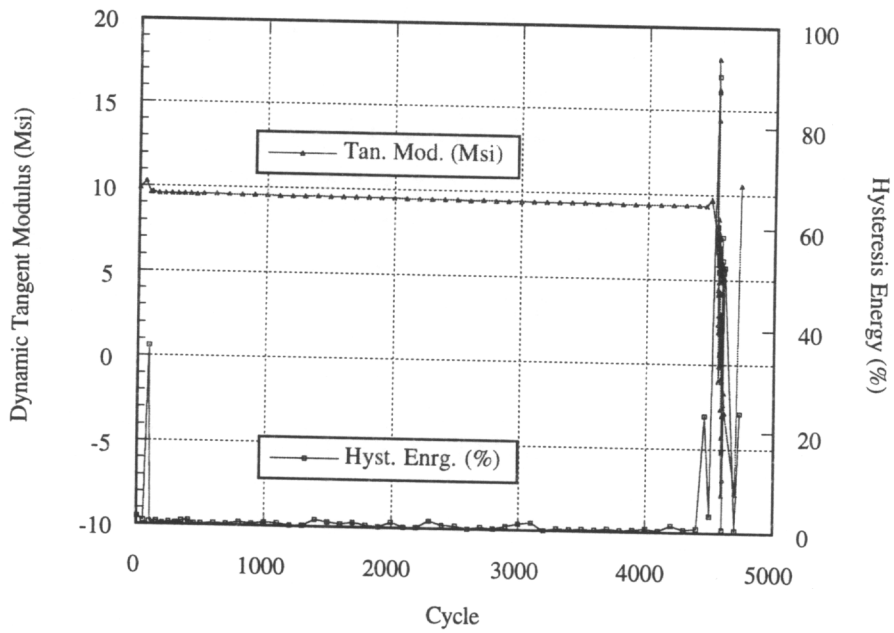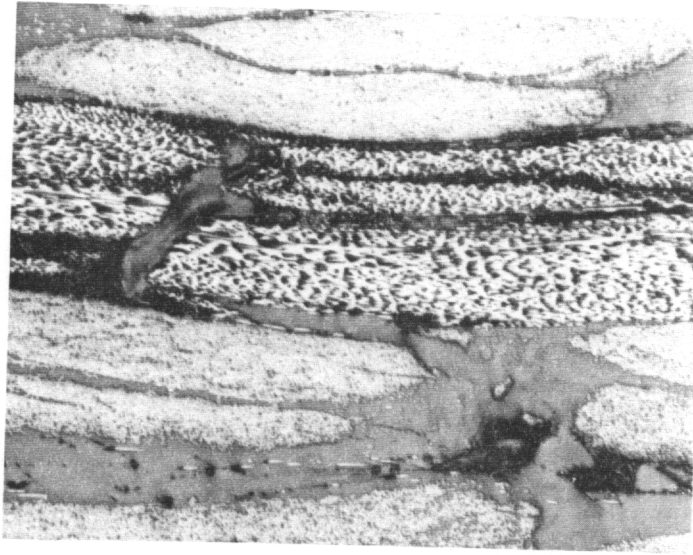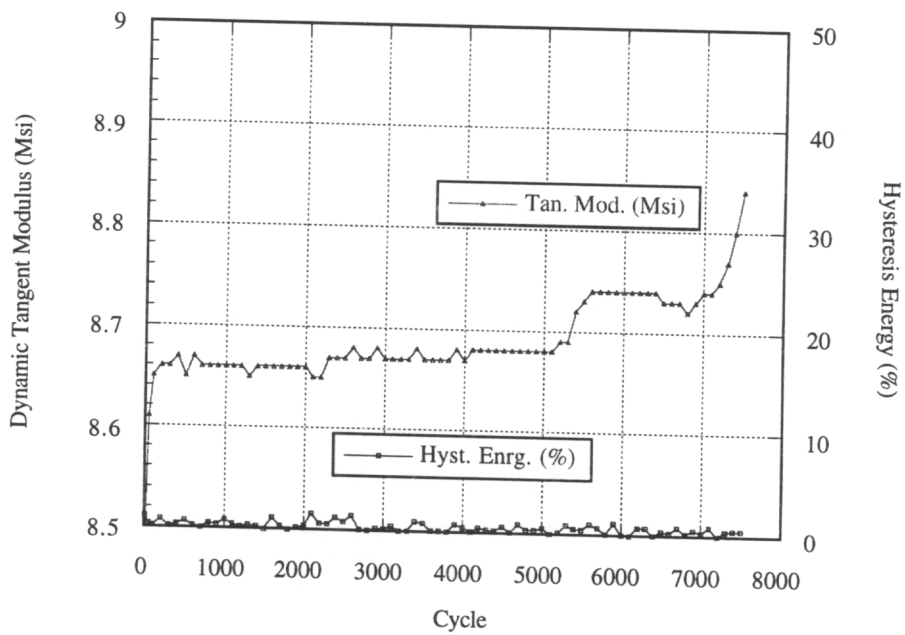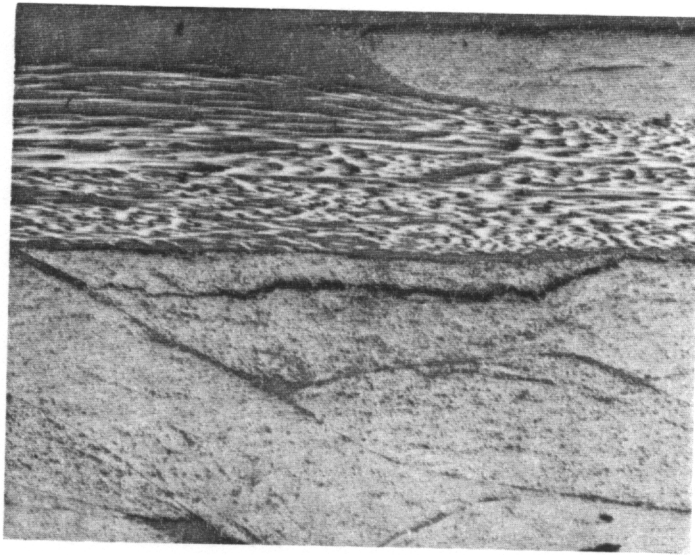
Figure 6.28 - Micrograph and Corresponding Dynamic Tangent Modulus and Normalized Hysteresis Energy Information vs. Cycle Number for an Unnotched LLL Architecture Specimen Containing an Initial Damage State.

the dark line running horizontally in the micrograph. The crack is oriented parallel to the axial bundle, which also runs horizontally in the micrograph. The corresponding dynamic tangent modulus information showed an increasing value with increasing cycle number. No major energy events were detected.

The micrograph shown in Figure 6.29 is bounded on the top and bottom by axial fiber bundles which extend horizontally across the micrograph. One axial fiber bundle contains a region where a kink band formed, indicated by a solid gray region. This region also extends into the braider fiber bundles in the center of the micrograph, indicating that the crack propagated from the location of the kink band into the adjacent braider fiber bundles. The second axial fiber bundle also contains remains of a kink band indicated by a wide black line in the center of the fiber bundle oriented at approximately a 45° angle to the horizontal. Each end of the kink band extends along the centerline of the axial fiber bundle in the form of a crack, indicated by a dark line along the center of the axial fiber bundle. The axial fiber bundle also disbonded along the boundary between the edge of the fiber bundle and the surrounding constituents. Remains of a third kink band were found in an axial fiber bundle at another location in the gage section of the specimen. Corresponding dynamic tangent modulus information showed an increasing trend with increasing cycles up to a point where a major energy event triggered a sharp increase in dynamic tangent modulus. The dynamic tangent modulus value then leveled off until a second major energy event occurred and the test was stopped. No other major energy
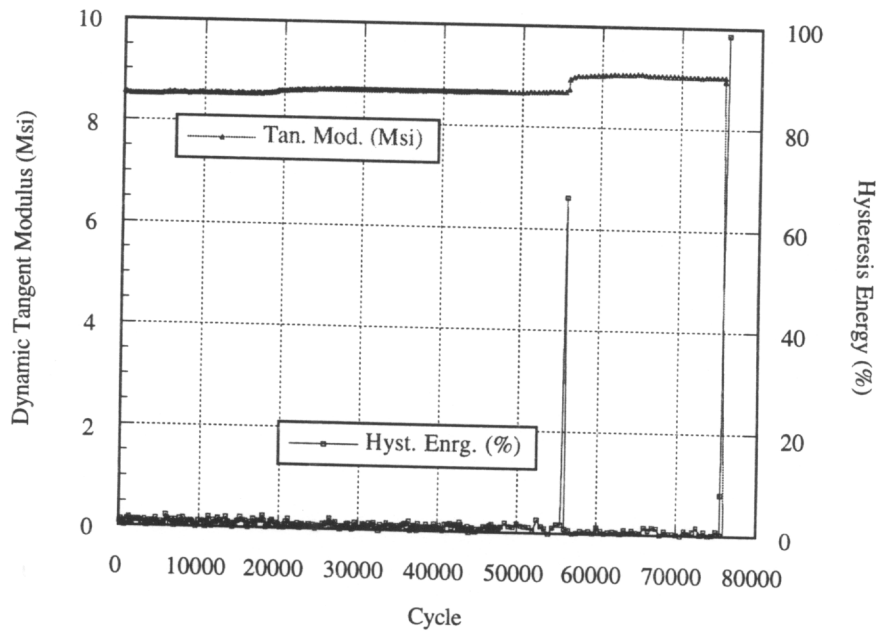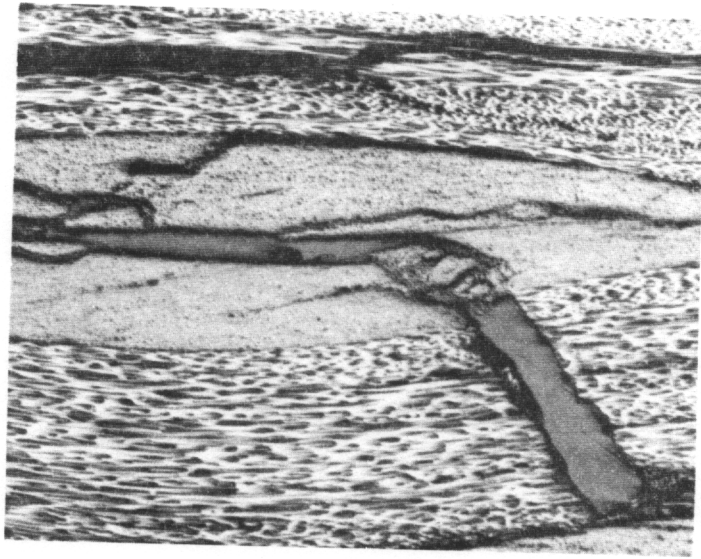
Figure 6.29 - Micrograph and Corresponding Dynamic Tangent Modulus and
Normalized Hysteresis Energy Information vs. Cycle Number for an Unnotched LLL
Architecture Specimen Containing a Progressed Damage State.

events were detected in the test.

The overall unnotched behavior of the LLL architecture was very inconsistent. A progression of damage mechanisms was not completely established. Instead, two damage states were presented which were an initial state and a very progressed state of damage. The initial state contained a crack in the braider bundles which was oriented parallel to the axial fiber bundles. The progressed state contained multiple kink bands, cracks extending from the edges of the kink bands into the surrounding braider fiber bundles, and cracks extending from the edges of the kink band along the center of the axial fiber bundle in which the kink band formed. Existence of kink bands in the axial fiber bundles corresponded with major hysteresis energy events which were detected during the test. When no major energy events were detected, no kink bands were found.

Notched - The notched specimens tested from the LLL architecture were very inconsistent with respect to the number of cycles tested to reach a specific damage state. Of the six specimens tested however, three distinct states of damage were identified. Good correlation with the dynamic tangent modulus and hysteresis energy information was found which supported the three levels of damage identified.

Specimen information from the initial damage level is shown in Figure 6.30. An axial fiber bundle spans the micrograph horizontally. The dark line running along the edge of the axial fiber bundle represents a disbond of the fiber bundle from the surrounding
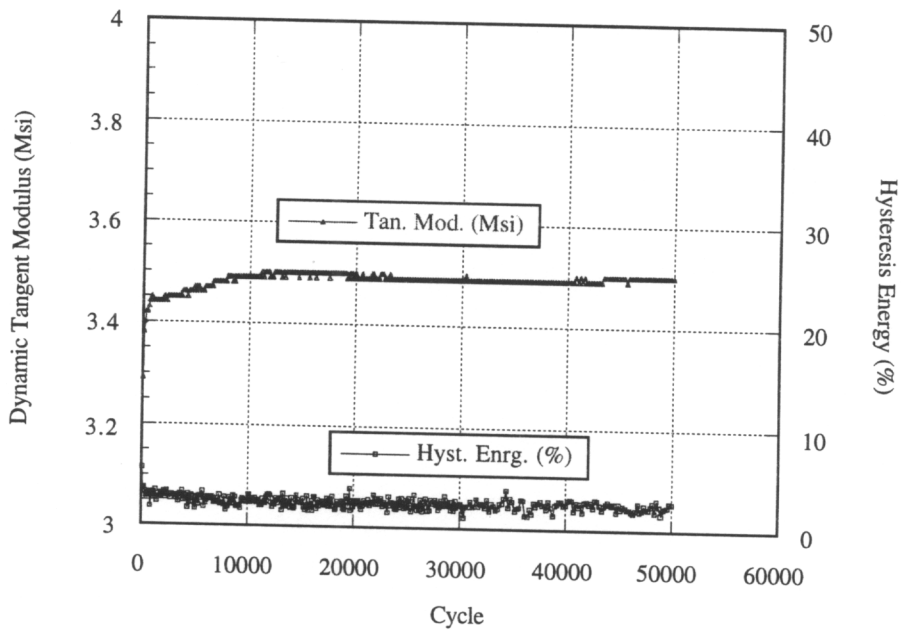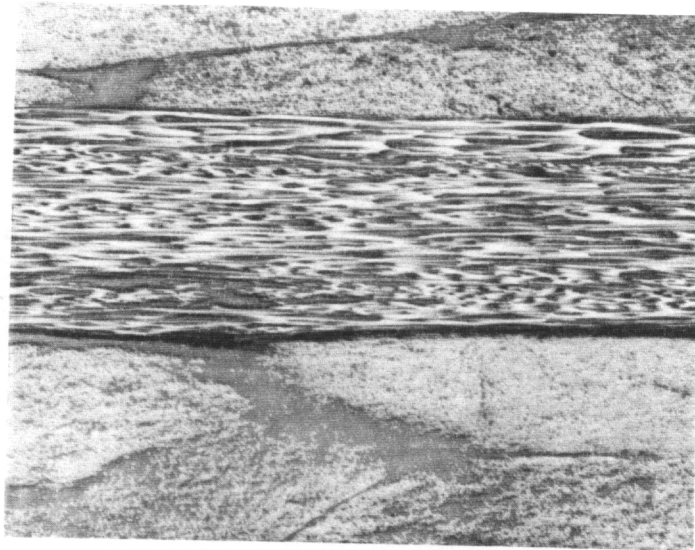
Figure 6.30 - Micrograph and Corresponding Dynamic Tangent Modulus and
Normalized Hysteresis Energy Information vs. Cycle Number for a Notched LLL
Architecture Specimen Containing an Initial Damage State.

braider fiber bundles and resin rich areas. No other damage mechanisms are present. The corresponding dynamic tangent modulus curve indicates a slightly increasing stiffness with increasing cycles. No major energy events were detected.

Kink band formation was found in the intermediate damage level. The micrograph shown in Figure 6.31 contains an axial fiber bundle which spans the picture horizontally. The dark line next to the solid grey region defines a free edge of the specimen. Two different damage mechanisms are seen in the micrograph. One area of the axial fiber bundle near the free edge contains a crack perpendicular to the free edge, and the fibers in that area have started to protrude outward toward the free edge. In another area of the axial fiber bundle, a newly formed kink band is seen. The short sections of fibers which make up the kink band are still intact. No damage outside the axial fiber bundle was found. The dynamic tangent modulus information yielded a steadily decreasing trend until the latter stages of the test where it decreased significantly. One major energy event occurred on the last cycle of the test corresponding to the one kink band found in the specimen.

A micrograph of the advanced damage mechanisms along with the corresponding dynamic tangent modulus and hysteresis energy information is shown in Figure 6.32. Kink bands formed in axial fiber bundles on both sides of the notch, corresponding to the two major energy events which occurred approximately half way through and near the end of the test. There were actually two individual kink bands found in the axial fiber bundles
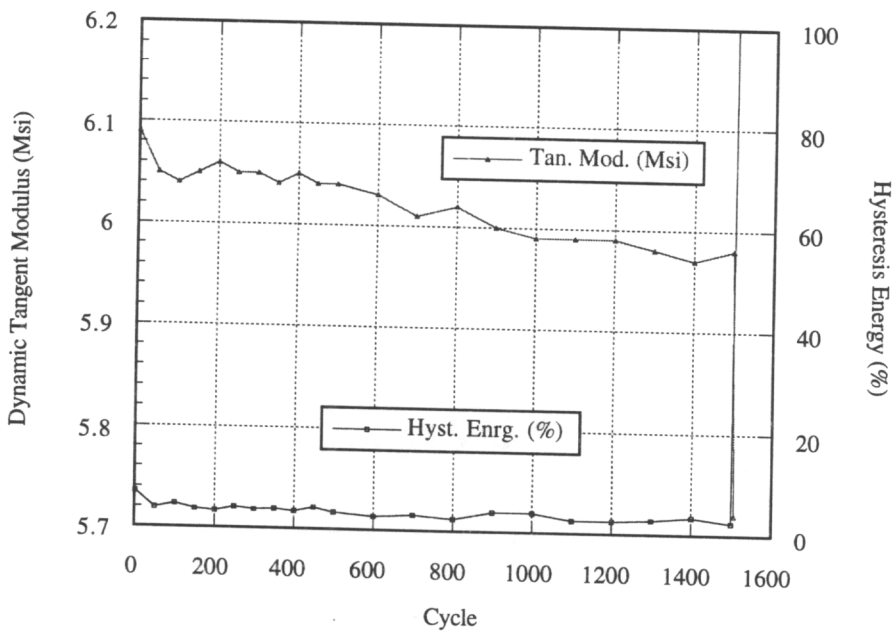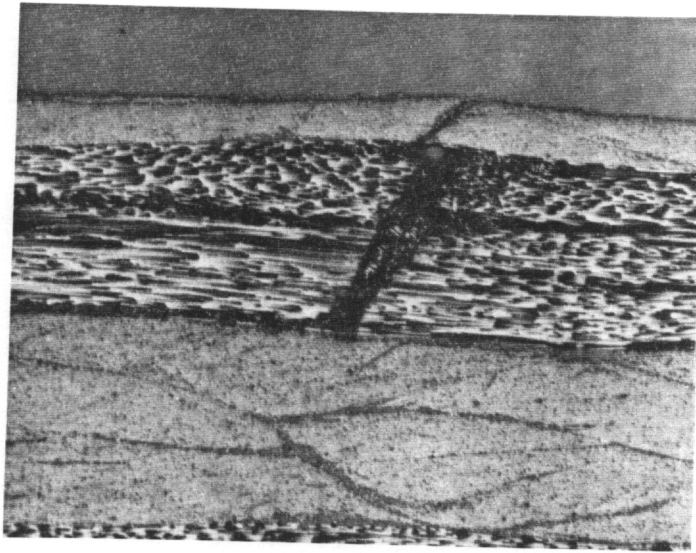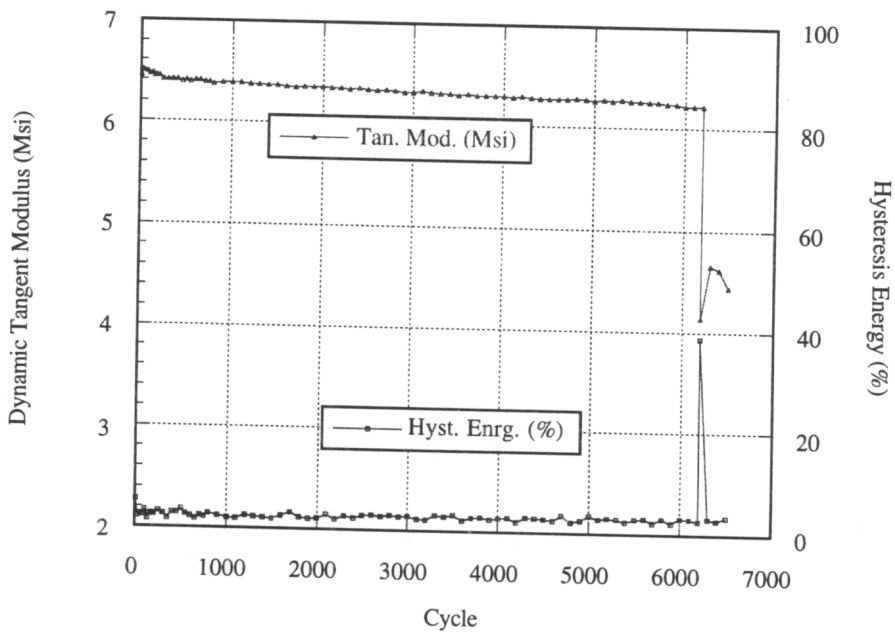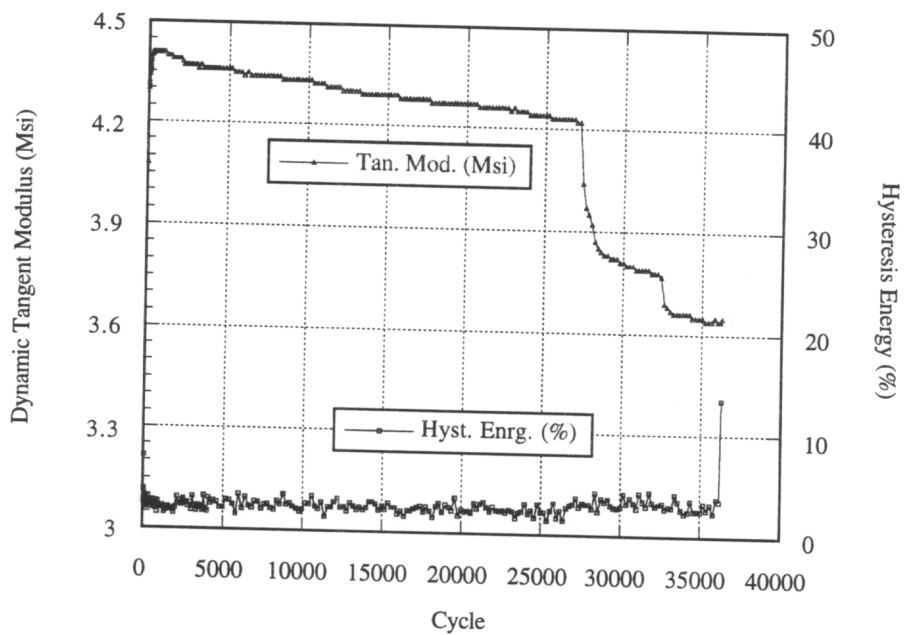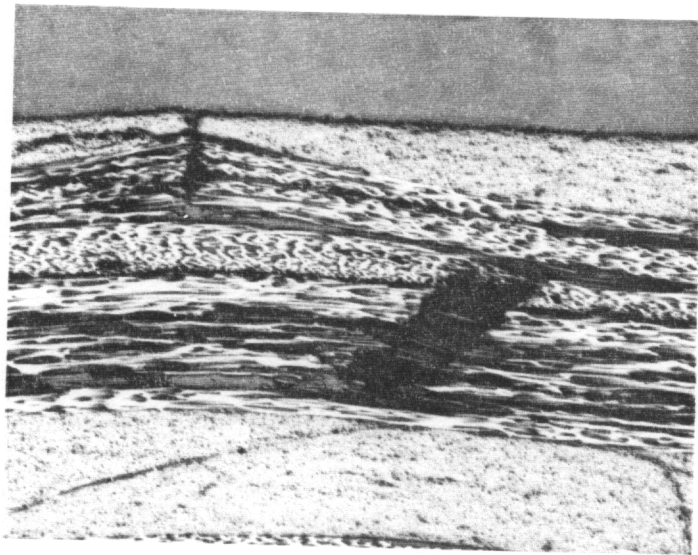
Figure 6.31 - Micrograph and Corresponding Dynamic Tangent Modulus and Normalized Hysteresis Energy Information vs. Cycle Number for a Notched LLL Architecture Specimen Containing an Intermediate Damage State.
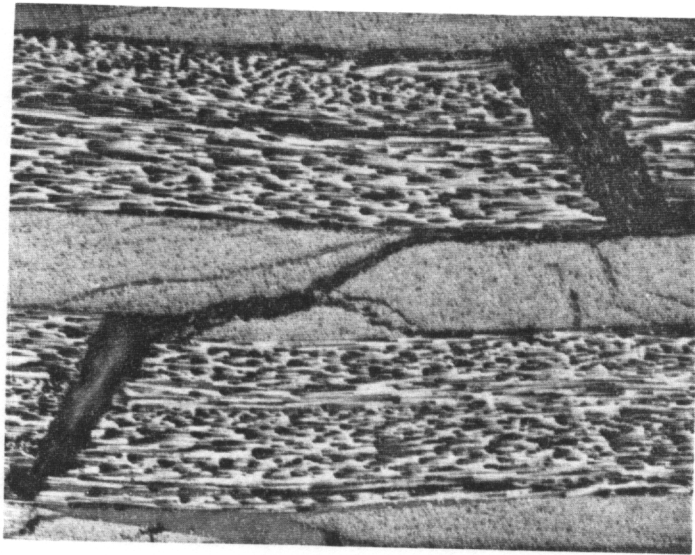
Figure 6.32 - Micrograph and Corresponding Dynamic Tangent Modulus and Normalized Hysteresis Energy Information vs. Cycle Number for a Notched LLL Architecture Specimen Containing an Advanced Damage State.

on both sides of the notch. This is consistent with previous results, when multiple kink bands formed on the same side of the notch, only one major energy event was detected. On each side of the notch, one of the kink bands formed in an axial fiber bundle near the face of the specimen, while the other formed near the center of the thickness direction. The dynamic tangent modulus information yielded a slightly increasing trend until the first major energy event occurred, when the dynamic stiffness increased significantly until the test was stopped.

The overall notched behavior of the LLL architecture yielded a progression of damage mechanisms. These mechanisms did not however, increase in severity with an increasing number of test cycles. Disbonding of the axial fiber bundles occurred first, and was followed by kink band formation. Just prior to failure, multiple kink bands were found. When two kink bands formed on opposite sides of the notch, two major energy events were detected. When multiple kink bands formed on the same side of the notch, only one major energy event was detected. Dynamic tangent modulus information indicated both increasing and decreasing trends with increasing numbers of cycles. Abrupt changes occurred in the dynamic stiffness curves when major energy events were detected.

6.5 Overall Conclusions

6.5.1 Effect of Axial Bundle Size (LSS vs. LLS)

Unnotched - The peak stress level determined to yield a specimen life of 100000 cycles was approximately 40% higher for the LLS architecture as compared to the LSS architecture. This corresponds to the static compression strength value of the LLS architecture which was approximately 40% higher than the static compression strength of the LSS architecture. Larger axial fiber bundles correlated with higher strengths. Similar characteristic dynamic tangent modulus and hysteresis energy versus cycle number responses were found for both architectures. Damage mechanisms were also consistent for each architecture. First, cracks in the resin rich areas and disbonding of the axial fiber bundles from neighboring constituents was found. In the latter stages of life, kink bands formed in the axial fiber bundles.

Notched - The LSS architecture yielded a more consistent response when a notch was present in the gage length. Increasing levels of damage correlated with increased numbers of test cycles as was found in the unnotched specimens. The response of the LLS architecture, however, was not consistent when a notch was present in the gage length. Increased levels of damage did not correspond with increased numbers of test cycles. In both architectures, kink bands were found to form in axial fiber bundles at the edges of the notch. The formation of these kink bands occurred at earlier stages than in the unnotched

specimens. Initial dynamic tangent modulus values were 10% lower on average for the notched LSS architecture specimens as compared to unnotched specimens from the same architecture. Initial dynamic tangent modulus values were 20% lower on average for the notched LLS architecture specimens as compared to unnotched specimens from the same architecture. Because the limited number of specimens available for testing, a level of statistical significance could not be associated with this difference. It can however, be concluded that the LLS architecture had an increased notch sensitivity as compared to the LSS architecture.

6.5.2 Effect of Architecture Scaling (SLL vs. LLL)

Unnotched - The peak stress level determined to yield a specimen life of 100000 cycles was approximately 35% higher for the SLL architecture than for the LLL architecture. The static compression strength for the SLL architecture was approximately 15% higher than that of the LLL architecture. The smaller scale of the SLL architecture yielded higher compression strength values, both under static compression loading and in compression fatigue. Both architectures were very inconsistent with respect to damage levels versus the number of cycles tested. No trends were established correlating specific damage levels to specific points in life. Both initial and progressed states of damage were established however, for both architectures. Kink band formation occurred very early in all tests completed on the SLL architecture, in contrast to the LLL architecture where resin rich areas cracked and axial fiber bundles disbonded first, and were followed by kink band

formation which occurred in the latter stages of the specimen life.

Notched - The SLL architecture had a greater notch sensitivity than the LLL architecture. Peak net stress levels used for the unnotched SLL specimens were too high for the notched specimens, and caused failure in the first few cycles of the test. Peak stress levels for the notched SLL specimens had to be reduced by approximately 10% to yield a specimen life long enough to study failure mechanisms. Even at this reduced stress level, the specimen lives were only a few thousand cycles. The LLL architecture was also notch sensitive, but was able to withstand the net section stress applied to the unnotched specimens.

7. Modeling of Material Responses

The goal of the present research project was to approach the material response modeling from a mechanics of materials perspective. Higher order techniques were completed concurrently in a separate research project [80]. The first part of this chapter covers modeling of the tension response to both static and fatigue loading. The second part covers modeling of the compression response to both static and fatigue loading.

7.1 Tension Response Modeling

Modeling of the tension responses of the four braided architectures in the present study was based on a classical lamination theory (CLT) approximation of each architecture. The CLT approximations were used in conjunction with shear-lag modeling techniques and power law assumptions to develop predictions for dynamic stiffness as a function of cycle number and peak applied stress level.

$+\theta°$		a
$-\theta°$		a
$0°$		c
$-\theta°$		a
$+\theta°$		a
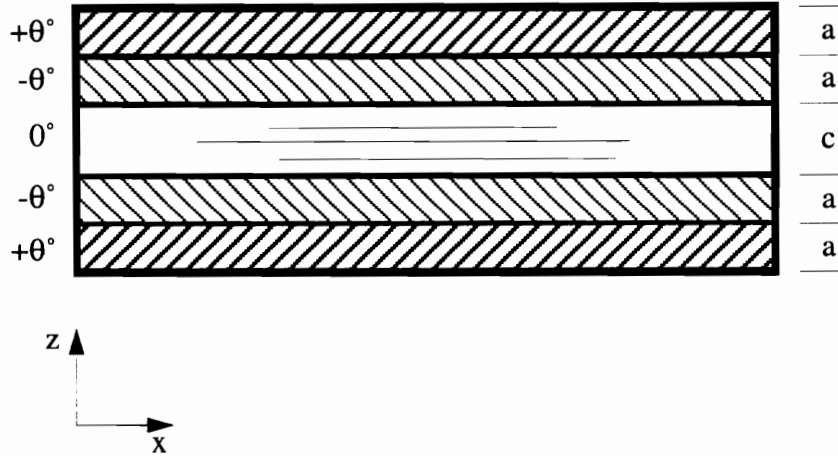
Figure 7.1 - Schematic of the Equivalent Laminate Approximation for an Individual Braided Layer

7.1.1 Static Tension Response - Elastic Moduli

In order to apply CLT to the braided architectures, an equivalent laminate approximation was formulated based on the stacked layers of individual braided preform mats in each architecture. The stacking sequence for a single layer of the braided architecture is shown in Figure 7.1. The center layer is oriented at $0°$ to the longitudinal direction, representing the axial fiber bundles. The outer two layers on either side of the $0°$ layer represent the braider fiber bundles, and are oriented at $\pm\theta°$ to the longitudinal direction. The thicknesses of the four off-axis layers are all equal, and are represented by

dimension a. The thickness of the 0° layer is represented by the dimension c. To determine the dimensions a and c for each architecture, three factors were used: 1) the total thickness t of each respective architecture, 2) the overall percentage of axial fiber bundles (paf) in each architecture, and (3) the number of individual layers (nlay) in each architecture. This yielded two equations for each architecture:

$$4a + c = \frac{t}{nlay}$$

$$[7.1]$$

$$c = \frac{t}{nlay}\left(\frac{paf}{100}\right)$$

The parameters for each architecture are listed in Table 7.1. This approximation yielded a balanced, symmetric equivalent laminate.

Table 7.1 : Equivalent Laminate Parameters for the Braided Architectures

Architecture	No. of Layers	% Axial Fiber Bundles	Thickness (in)	a (in)	c (in)
LSS	5	12	0.105	0.00462	0.0025
LLS	3	46	0.108	0.00486	0.0166
SLL	4	46	0.109	0.00368	0.0125
LLL	3	46	0.115	0.00518	0.0176

The equivalent laminate approximation for each braided architecture was used to generate extensional and bending stiffness values using a CLT analysis. Values for

longitudinal modulus, transverse modulus, shear modulus, and Poisson's ratio for an individual lamina were also required in the CLT analysis to predict to overall laminate parameters. The following values from [81] for a 60% volume fraction AS4 3501-6 material system were used for the lamina properties:

$$E_1 = 20 \times 10^6 psi$$
$$E_2 = 1.2 \times 10^6 psi$$
$$G_{12} = 8.95 \times 10^5 psi$$
$$\nu_{12} = 0.282$$

[7.2]

A convention was followed where the (1) and (2) directions corresponded to longitudinal and transverse directions of an individual lamina respectively, and the x and y directions correspond to the global longitudinal and transverse directions respectively.

The inverse of the extensional stiffness matrix [A] of the laminate calculated in the CLT code was used to determine the engineering material parameters through the following relationships for a symmetric, balanced laminate:

$$E_x = \frac{1}{a_{11}t}$$

$$E_y = \frac{1}{a_{22}t}$$

$$G_{xy} = \frac{1}{a_{66}t} \qquad 7.3$$

$$v_{xy} = -\frac{a_{12}}{a_{11}}$$

Table 7.2 lists the predicted values of four elastic constants for each braided architecture, while Table 7.3 lists the corresponding measured elastic constants. The predicted values for E_x and v_{xy} were in very close agreement with the corresponding measured values for all of the braided architectures. Values of E_x predicted from the equivalent laminate model had differences ranging from 0.4% for the LSS architecture to 13% for the LLL architecture, while values of v_{xy} had differences ranging from 0.4% for the LSS architecture to 6.2% for the LLS architecture. The predicted values of E_y were all greater than the corresponding measured values, and had differences ranging from 15% to 30%. The trends, however, were consistent with those of the measured values. Because the equivalent laminate model neglected the braider fiber bundle undulations and assumed a straight fiber layer, the corresponding stiffnesses were over predicted. The predicted values for the shear moduli G_{xy} were also higher than the measured values of all four architecture, with differences ranging from 9% to 24%, however, the predictions did

match the trends of the measured values.

In summary, a CLT calculation was made using an equivalent laminate approximation for the braided architectures. Excellent agreement was found between measured and predicted values of longitudinal modulus for each architecture. This was a very important building block for extending the present stiffness model to account for damage mechanisms.

Table 7.2 : Predicted Elastic Constants for the Braided Architectures

Architecture	Predicted E_x (Msi)	Predicted E_y (Msi)	Predicted G_{xy} (Msi)	Predicted v_{xy}
LSS	5.16	3.74	4.69	0.712
LLS	11.01	3.61	3.22	0.654
SLL	10.10	9.25	1.86	0.146
LLL	10.10	9.25	1.86	0.146

Table 7.3 : Measured Elastic Constants for the Braided Architectures

Architecture	Measured E_x (Msi)	Measured E_y (Msi)**	Measured G_{xy} (Msi)*	Measured v_{xy}**
LSS	5.18	2.92	4.05	0.709
LLS	10.81	2.60	2.46	0.613
SLL	9.72	7.32	1.70	0.155
LLL	8.78	6.87	1.60	0.152
* Obtained from reference [79]. ** Obtained from reference [26].				

7.1.2 Static Tensile Response - Strength

Determination and modeling of damage mechanisms in braided composites was the goal of the present research project. Predicting strengths of the four braided architectures was not a key component of this work. None the less, strength predictions from the equivalent laminate approximation are presented for completeness in evaluating the present modeling technique. Also, stress states in individual plys are studied in order to provide a mathematical basis for some of the observed behaviors.

The initial damage mechanism in each of the braided architectures was splitting of the braider fiber bundles along their length. This correlated with the CLT analysis which indicated by using a maximum stress criterion, the first plys to fail in each of the architectures were the off-axis plys. The failures were in the transverse (2) direction of the lamina. In each of the architectures, however, the first-ply failures did not cause ultimate failure of the specimen due to the dominance of the axial fiber bundles. Therefore, the failure of the off-axis plys was incorporated into the equivalent laminate model by reducing the values of the elastic constants in the direction of failure. For the transverse splitting in the off-axis plys, this correlated to reducing the values of E_y and G_{xy} to a small percentage of their original values. An arbitrarily chosen value of ten percent was used in the present research to simulate the residual intertwining effects of the damaged braider bundles. The reducing percentage was irrelevant for all but the LSS architecture, where the value could be adjusted to match the measured strength of the LSS architecture.

However, because the predictions were significantly greater than the measured values for the architectures with large axial bundles, and the goal of the present research was not to predict static strengths of the braided architectures, only a single reducing value of 10% was studied. The reduced values were then incorporated into the CLT calculation, and the ratio of the longitudinal stress in the 0° layer to the total applied stress was determined. The measured and predicted values of ultimate strength for each of the four braided architectures are listed in Table 7.4. The CLT analysis predicted a lower strength than was

Table 7.4 : Predicted vs. Measured Ultimate Tensile Strength Values for the Braided Architectures

Architecture	Measured Ultimate Strength (ksi)	Predicted Ultimate Strength (ksi)	Difference (%)
LSS	53.7	44.5	17
LLS	93.5	154	39
SLL	122.4	146	16
LLL	70.7	158	55

measured for the LSS architecture, and a higher strength than was measured for the axially dominated architectures, with differences as high as 55%. This indicated that the undulation of the axial fiber bundles in the LLS, SLL, and LLL architectures were detrimental to the ultimate strength of the architectures, and must be accounted for in an ultimate strength model.

Splitting of the axial fiber bundles in specimens from the SLL architecture was found in the in-situ x-ray static tension testing sequence. The splits occurred in an SLL specimen which had a nested stacking sequence of the individual braided layers. Splitting of the axial fiber bundles along their length was also found in all of the tension fatigue specimens from the SLL and LLL architectures. Splitting of the axial fiber bundles along their length did not occur in the LSS and LLS architectures, both of which had a 45° braid angle as compared to the 70° braid angle of the SLL and LLL architectures. These experimental determinations are supported by the equivalent laminate model. For the LSS and LLS architectures, the CLT analysis predicts that the 0° layers are under a *compressive* transverse stress, while for the SLL and LLL architectures, the 0° layers are under a *tensile* transverse stress. This is because the 0° layers want to contract in their transverse direction when a longitudinal transverse load is applied, but are constrained by the 70° layers which are not allowing the contraction to occur, thus inducing a positive transverse stress in the 0° layers. The predicted applied stress level at which transverse splitting would occur in the 0° layers was, however, greater than the longitudinal strength of the 0° layers. This result indicates two important points: 1) the nested stacking configuration found in the static tension SLL specimen produced a transverse stress in the axial fiber bundles great enough to cause transverse splitting, a result which the equivalent laminate model did not predict, and 2) while the stress state required to cause transverse splitting in the axial fiber bundles was not reached under monotonic tensile loading conditions for the LLL architecture and the remaining specimens in the SLL architecture,

the stress state was great enough to produce splitting under fatigue loading conditions in all tension fatigue specimens from the SLL and LLL architectures.

7.1.3 Tension Fatigue Response - Stiffness versus Damage Level

Modeling of the tension fatigue response for the braided architectures was completed in two steps. In the first step, the primary initial damage mode was determined, and the damage mode was incorporated into the equivalent laminate model. In the second step, power law assumptions were made, and the damage model was fit to measured dynamic stiffness versus cycle number data from individual tension fatigue tests. The following section presents the development of the equivalent laminate damage model.

In each of the braided architectures, the initial damage mode was splitting of the braider fiber bundles. This damage mode was determined to be the dominating mechanism in reducing the longitudinal stiffness of each architecture. To incorporate this damage mechanism into the equivalent laminate model, a shear-lag modeling approach developed by Reifsnider [71] was utilized. This method was chosen due to its ability to account for splitting in off-axis plys with orientations other than 90°. Several other approaches have been taken, all of which were limited to the analysis of $(0/90)_s$ laminates.

To begin, the damage state in the equivalent laminate shown in Figure 7.2 was assumed. The 0° layers were assumed to be undamaged, while the off-axis plys contained a transverse crack at x=0. Because the shear-lag approach used was one-dimensional, with the stresses varying in each individual layer as a function of x only, the absolute value of the ply orientation was used. The stiffness in the x-direction of a +45° ply was the same as that for a -45° ply. Therefore, where off-axis plys were adjacent to each other, they were considered to be a single layer with a thickness equal to the sum of the adjacent plys.
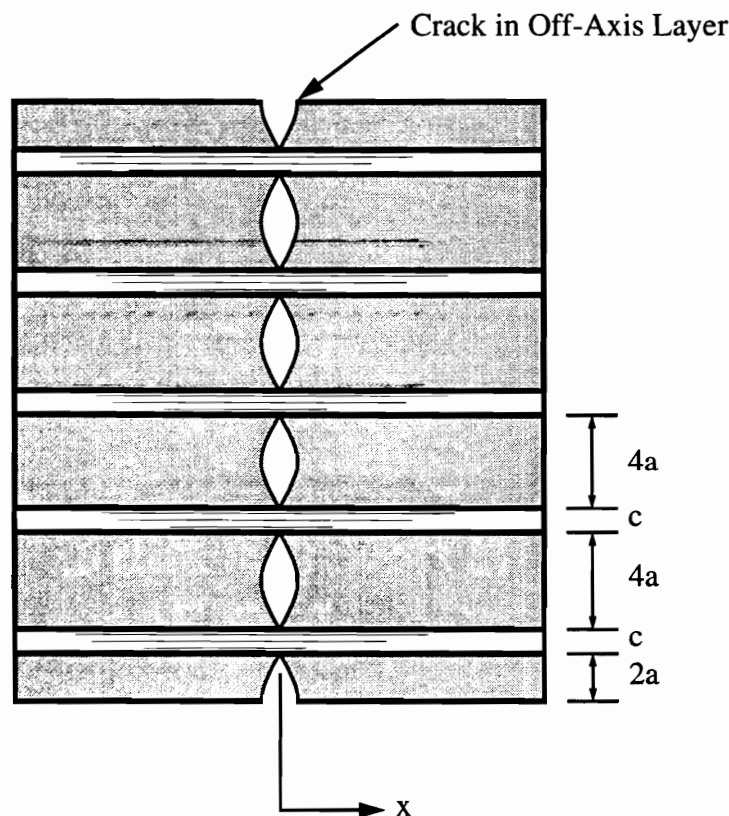
Figure 7.2 - Schematic of the Equivalent Laminate Approximation for the Shear-Lag Approach Including Damage in the Off-Axis Layers for the LSS Architecture

Governing differential equations were generated for the shear-lag modeling approach by constructing free body diagrams for each layer in the equivalent laminate. The forces in the x-direction were summed and set equal to zero, satisfying x-direction equilibrium. This generated one differential equation per layer. It is very important at this point in the development of the model that the symmetry of the problem be recognized. This simplifies the solution of the system into an analysis of a single repeating unit. Because the approach was one-dimensional, the shear stress in the interior of each layer was zero. At a common value of x within an individual layer, the displacement was constant through the thickness of the layer, and thus required a state of zero shear stress through the thickness of the layer. This reduced the multi-layered equivalent laminate model to the repeating unit shown in Figure 7.3. A schematic of the assumed displacement field is also shown in the figure. A coupled system of two ordinary differential equations was then generated from the free body diagrams shown in Figure 7.4. Between the two layers, the shear transfer was assumed to occur over a distance b, which for the present analysis was assumed to be 1/20th of the thickness of the cracked layer. This value was chosen for b based on the work by Reifsnider [71].

Applying x-direction equilibrium for each layer yielded the following two differential equations:
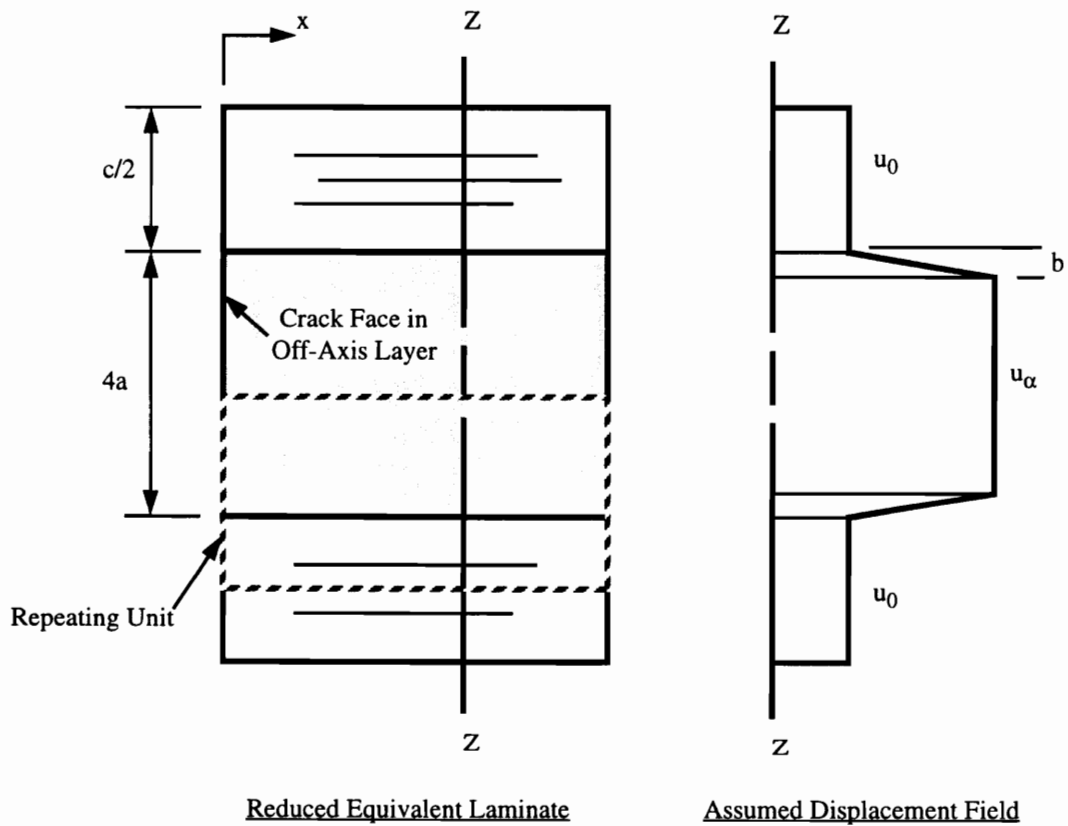
Figure 7.3 - Reduced Equivalent Laminate Model and Assumed Displacement Field
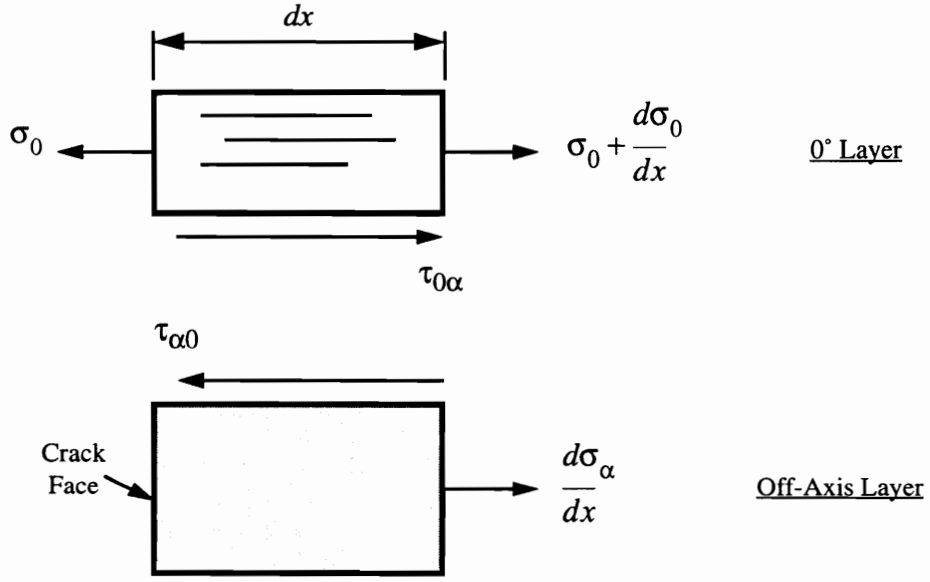
Figure 7.4 - Free Body Diagrams of Differential Elements for the Shear-Lag Analysis

$$\frac{bc}{2}\frac{d\sigma_0}{dx} + \tau_{0\alpha}dx = 0$$

$$2ab\frac{d\sigma_\alpha}{dx} + \tau_{\alpha 0}dx = 0$$

7.4

By noting that $\sigma_0 = E_0\varepsilon_0$; $\sigma_\alpha = E_\alpha\varepsilon_\alpha$; $\frac{du_0}{dx} = \varepsilon_0$ and $\frac{du_\alpha}{dx} = \varepsilon_\alpha$, and also that

$\tau_{0\alpha} = G\left(\frac{u_0 - u_\alpha}{b}\right)$, where G is the shear modulus of the matrix, the following equations

were generated:

$$A\frac{d^2u_0}{dx^2} + (u_\alpha - u_0)\,dx = 0$$

$$B\frac{d^2u_\alpha}{dx^2} + (u_0 - u_\alpha)\,dx = 0 \qquad\qquad 7.5$$

where

$$A = \frac{E_0 bc}{2G} \qquad and \qquad B = \frac{2abE_\alpha}{G}$$

Boundary conditions for the system of equations in 7.5 were such that the displacement at x=0 in the 0° layers was zero, the strain in the off-axis layers was zero at x=0 denoting the stress-free crack face, and that the strain at x=∞ equalled the strain in the undamaged state. Mathematically stated the boundary conditions were:

$$u_0(0) = 0 \qquad \frac{du_0}{dx}(\infty) = \frac{\sigma_{app}}{E_{lam}}$$

$$\qquad\qquad 7.6$$

$$\frac{du_\alpha}{dx}(0) = 0 \qquad \frac{du_\alpha}{dx}(\infty) = \frac{\sigma_{app}}{E_{lam}}$$

where σ_{app} was the applied stress and E_{eql} was the modulus of the overall equivalent laminate.

The solution of the system of differential equations with the method of characteristics yielded

$$\begin{pmatrix} u_\alpha \\ u_0 \end{pmatrix} = C_1 \begin{pmatrix} 1 \\ 1 \end{pmatrix} + C_2 \begin{pmatrix} x \\ x \end{pmatrix} + C_3 \begin{pmatrix} -\frac{A}{B} \\ 1 \end{pmatrix} e^{-\lambda x} + C_4 \begin{pmatrix} -\frac{A}{B} \\ 1 \end{pmatrix} e^{\lambda x} \qquad 7.7$$

$$\text{where} \qquad \lambda = \sqrt{\frac{A+B}{AB}}$$

Application of the boundary conditions [7.6] yielded the final equations:

$$\begin{pmatrix} u_\alpha \\ u_0 \end{pmatrix} = \frac{\sigma_{app}}{E_{eql}} \left[\frac{B}{A\lambda} \left(\begin{pmatrix} 1 \\ 1 \end{pmatrix} + \begin{pmatrix} \frac{A}{B} \\ -1 \end{pmatrix} e^{-\lambda x} \right) + x \begin{pmatrix} 1 \\ 1 \end{pmatrix} \right] \qquad 7.8$$

With the displacements in each layer determined, the next step is to make the inherent assumption in the shear-lag modeling approach that a new crack will form in the off-axis ply when the stress in that ply returns to the stress level at which the first crack formed. This distance was defined as the saturation crack spacing s. Only the concept of s was needed at this point, not the specific solution. The effective modulus of the damaged laminate was then calculated by computing the strain in the cracked layer over the distance from x=0 to x=s, and dividing it into the applied stress σ_{app} :

$$E_{dam} = \frac{\sigma_{app}}{\varepsilon_{dam}}$$

7.9

where $\qquad \varepsilon_{dam} = \dfrac{u_\alpha(s) - u_\alpha(0)}{s}$

The final form of equation [7.9] is

$$E_{dam} = \frac{E_{eql}}{1 + \dfrac{A}{B\lambda s}[1 - e^{-\lambda s}]}$$

7.10

The last addition to make to the prediction for the damaged modulus E_{dam} was to relate

the damage parameter D to the crack spacing s. The damage D was simply assigned to

equal the inverse of the crack spacing s (i.e. $D=1/s$) so that as the crack spacing decreased

and the specimen reached a more severe damage state, the damage parameter increased.

This method was most recently used in [82]. Figure 7.5 shows a plot of the damage

modulus normalized with respect to the undamaged modulus, as a function of the damage

parameter D for the LSS architecture. As can be seen, as the damage parameter increased,

the normalized damage modulus decreased for all architectures. The most sensitive

architecture was the LSS which contained only 12% axial fiber bundles as compared to

46% for the other three architectures. The LLS architecture was more sensitive as
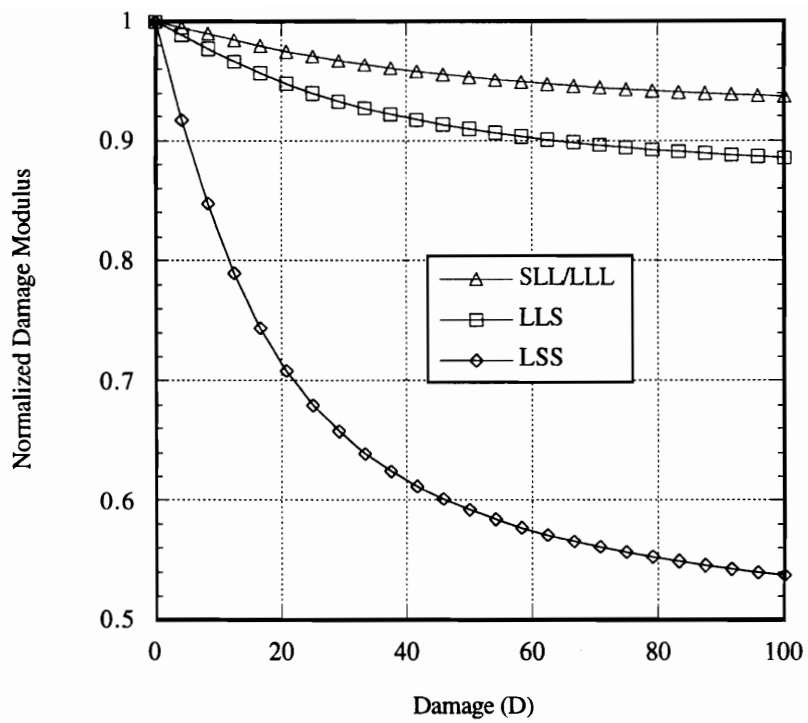
Figure 7.5 - Predicted Normalized Damage Modulus versus Damage for Four Braided Architectures

compared to the SLL and LLL architectures. This was because the 45° layers in the LLS architecture were stiffer than the 70° layers, and played a larger role in the longitudinal stiffness of the architecture, thus causing a larger stiffness decrease when the material was damaged. In summary, this stiffness-damage relationship provided the basis for extending the damage model to tension fatigue conditions.

7.1.4 Tension Fatigue Response - Stiffness versus Cycle Number

Once the stiffness versus damage level relationship was completed, a rate relationship was needed to define stiffness and damage level versus cycle number. Previous work completed by Ogin et.al [80] was used as a starting point for the present analysis. In the reference, it was postulated that the total crack length a in a cross-ply laminate under tensile loading increased with cycling as a power function of the stored elastic energy. This yielded the following equation:

$$\frac{da}{dN} \propto (\sigma_{max}^2 s)^n \qquad 7.11$$

where σ_{max} was the maximum applied stress level, n an empircal power law exponent, and s the distance between two cracks in the same layer. It was further assumed in [80] that the total crack length was proportional to the crack density in the 90° plys, yielding:

$$\frac{dD}{dN} = C_1 \left(\frac{\sigma_{max}^2}{D} \right)^n \qquad\qquad 7.12$$

where C_1 was a proportionality constant. This damage versus cycle number relationship was based on a stored elastic energy relationship for the area of material between two cracks in the off-axis ply in a $(0/90)_s$ laminate. It was postulated in the present work that this relationship could be used for any balanced, symmetric laminate whose stiffness versus cycle number response was controlled by the formation of cracks in the off-axis layers.

Equation [7.12] was integrated and solved for D as a function of the number of cycles N, yielding:

$$\frac{D^{n+1}}{(n+1)} = C_1 \sigma^{2n} N + C_2 \qquad\qquad 7.13$$

The constant of integration C_2 was zero due to the initial condition that the damage equaled zero when the cycle number equaled zero. This relationship was then substituted into equation [7.10] to yield:

$$E_{dam} = \cfrac{E_{eql}}{1 + \cfrac{BD}{A\lambda}\left[1 - e^{\frac{-\lambda}{D}}\right]}$$
$$\qquad\qquad\qquad\qquad\qquad\qquad\qquad\qquad\qquad\text{7.14}$$

$$where \qquad D = \sqrt[n+1]{C_1\sigma^{2n}N(n+1)}$$

In the work by Ogin et.al. [82], a stiffness versus damage relationship limited to a (0/90)$_s$ laminate was used. In the present research, the stiffness versus damage relationship developed in section [7.1.3] for any balanced, symmetric laminate with cracking in the off-axis layers was used. Also, a different method of fitting the stiffness function to the experimental data was used in the present research, which is explained in the following section.

The stiffness versus damage relationship in [7.14] was fit to the experimentally obtained dynamic tangent modulus versus cycle number curves using the Levenberg-Marquardt nonlinear curve fitting technique presented in Chapter 14 of [78]. The constants C_1 and n were determined such that the error between the prediction and the experimental data was minimized.

7.1.5 Fitting of Experimental Data

The stiffness versus cycle number model developed in the preceding sections was based on an equivalent laminate approximation of the braided architectures. The model did not account for undulations which existed in the braider and axial fiber bundles of the braided architectures. The basic premise of the model was that cracking in the off-axis layers was the main contributor to the stiffness decreasing with increasing cycle number. This was in large part the case for all of the braided architectures, particularly the LSS architecture which contained the largest amount of braider fiber bundles. However, the braided architectures, particularly those which contained large axial fiber bundles, were also affected by the disbonding of the axial fiber bundles along their length. This disbonding caused large drops in dynamic stiffness during tension fatigue testing in both the LLS and SLL architectures. Also, the variability in specimen response, particularly in the LSS and SLL architectures, was very high. The only reasonably consistent set of dynamic stiffness versus cycle number data was from the six unnotched specimens from the LSS architecture. Therefore, the following section fits the stiffness versus cycle number model to those six specimens to determine the validity of the model as applied to the LSS architecture. While the splitting of the braider fiber bundles did account for a large portion of the dynamic stiffness decrease in the LSS and SLL architectures, the variability in the data, along with the contribution of the axial fiber bundles disbonding along their length precluded and acceptable fit of the model to those architectures.

The model was fit to the six unnotched specimens from the LSS architecture tested at an upper stress level of 35 ksi and a lower stress level of 33 ksi. A typical fit to a response from the LSS architecture which was smooth is shown in Figure 7.6. The model fit the experimentally obtained data points very well, and captured the trend of the results. A typical fit to a response from the LSS architecture which did not exhibit a smooth trend is shown in Figure 7.7. The model did match the trend, but did not match the experimental data as closely as that of the smooth response. Any deviation from a smooth, decreasing stiffness versus cycle number response resulted in a poorer fit of the model.

The values of C_1 and n are listed in Table 7.5 for the six specimens. All inputs were defined in inches and pounds. The predictions of C_1 and n were very close for the three specimens tested at 33 ksi, and also for the three specimens tested at 35 ksi.The values of the constant C_1 were not, however, consistent across the two different stress levels.This prevented determination of a single model which would predict the stiffness as a function of applied stress and cycle number for unnotched specimens from the LSS architecture, using the previously developed damage model. The model fit for using average values of C_1 and n for each applied stress level is shown in Figure 7.8. The higher applied stress level yielded a higher rate of stiffness decrease with respect to cycle number as compared to the lower applied stress level. However, because common values of C_1 were not able to be determined across different applied stress levels for the same architecture, the model was limited to fitting a set of stiffness versus cycle number curves for a single given stress
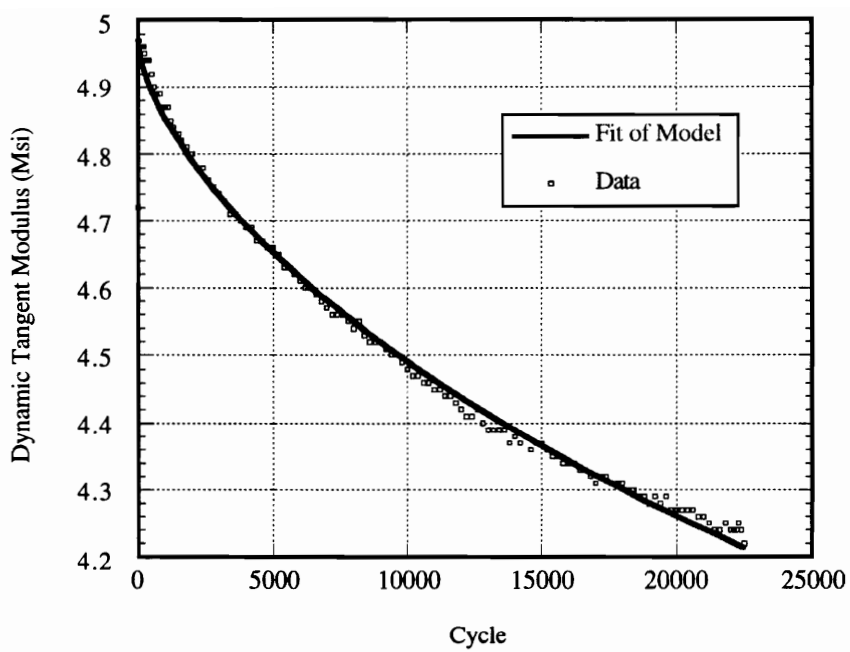
Figure 7.6 - Fit of Damage Model to a Smooth Dynamic Tangent Modulus versus Cycle Number Response (Specimen LSS-7)
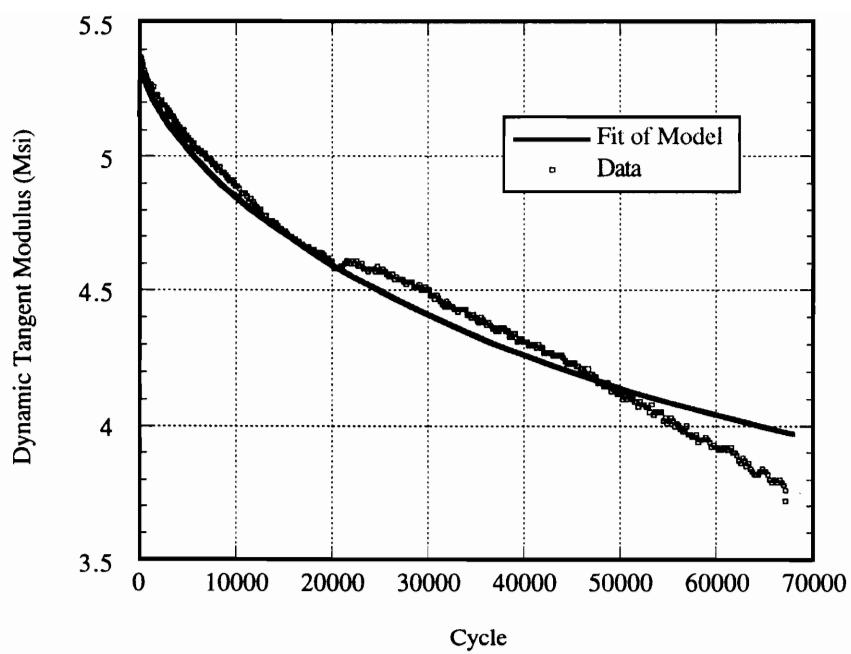
Figure 7.7 - Fit of Damage Model to a Varying Dynamic Tangent Modulus versus
Cycle Number Response (Specimen LSS-5)
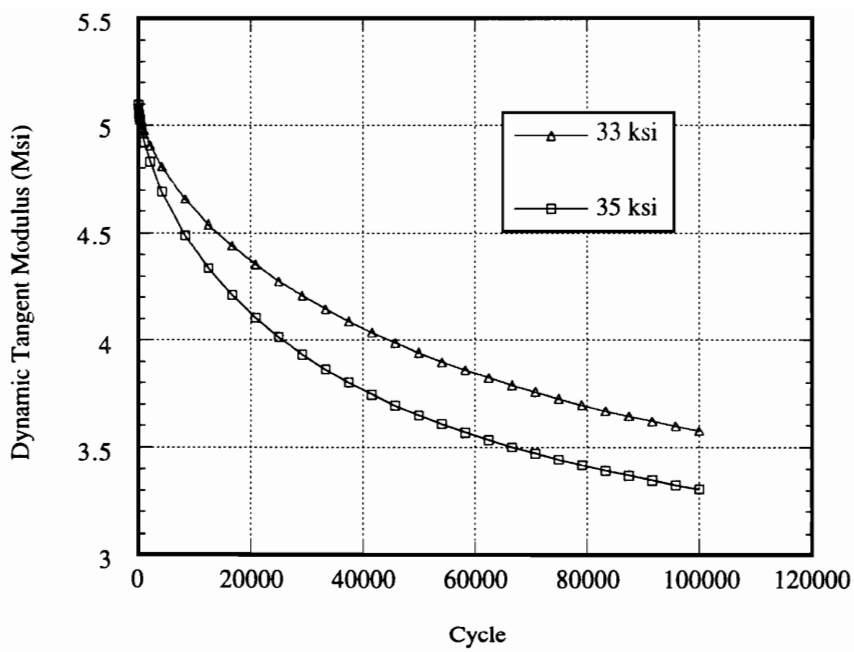
Figure 7.8 - Average Fits of the Damage Model to Tension Fatigue Specimens Tested at the High and Low Stress Levels from the LSS Architecture.

level, and determining average values of C_1 and n for that set.

7.1.6 Overall Conclusions on Tension Response Modeling

The longitudinal elastic modulus of each of the four braided architectures in this study were predicted using an equivalent laminate model based on classical lamination theory. Reasonable estimates were also predicted for the transverse modulus, shear modulus, and Poisson's ratio for each architecture.

Table 7.5 : Fitting Parameters for Tension Fatigue Specimens from the LSS Architecture

Specimen	Applied Stress Level (ksi)	C_1	n
LSS-5	33	3.420E-8	0.55
LSS-6	33	3.305E-8	0.55
LSS-7	33	3.347E-8	0.55
		avg. = 3.36E-8 COV = 1.8%	avg. = 0.55
LSS-8	35	4.835E-8	0.55
LSS-9	35	7.584E-8	0.55
LSS-10	35	4.0E-8	0.55
		avg. = 5.47E-8 COV = 34%	avg. = 0.55

A stiffness versus crack density model was developed based on a shear-lag modeling approach. The expression was then extended to include the effects of cycle number through a power law relationship. The final expression relating longitudinal stiffness to cycle number was fit to the experimentally obtained data. While the model was found to fit the smooth trends of the unnotched tension fatigue specimens from the LSS architecture, a consistent set of constants allowing the prediction of stiffness versus cycle number for varying applied stress level could not be determined. This is most likely due to the fact that the damage model does not account for undulations in the fiber bundles of the braided architectures, nor the effects of disbonding of the axial fiber bundles on the overall longitudinal modulus.

The damage model was not fit to any responses from either the LLS and SLL architectures due to the varied responses of thos architectures. Also, the large drops in longitudinal stiffness which were characteristic of the LLS and SLL architectures yielded extremely poor fits of the model to the experimental data.

7.2 Compression Response Modeling

Modeling of the static compression response was limited to longitudinal moduli predictions for the equivalent laminate model. The compression response was found to be dominated by kink band formation under both static and fatigue testing conditions for all braided architectures in this study. A review of the published literature pertaining to kink

band mechanics is presented, as well as requirements for extending the work to include modeling of braided composites.

7.2.1 Static Compression Response - Elastic Moduli

Comparisons of the measured and predicted longitudinal compression moduli are listed in Table 7.6 for the four braided architectures in the present research. The equivalent laminate model overpredicted the longitudinal moduli by at least 8% for all architectures. This was an indication that the undulation of both the braider and axial fiber bundles caused a softened response, and was unaccounted for in the equivalent laminate model. The equivalent laminate model provided only a rough estimate of the longitudinal compressive moduli of the braided architectures.

Table 7.6 : Measured and Predicted Longitudinal Compression Moduli for the Braided Architectures

Architecture	Measured E_x (Msi)	Predicted E_x (Msi)	Difference (%)
LSS	4.70	5.16	8.9
LLS	10.09	11.01	8.4
SLL	8.99	10.10	11.0
LLL	9.16	10.10	9.3

7.2.2 Compression Fatigue Response

In each of the four braided architectures tested in this research project, kink band formation in the axial fiber bundles was found to govern the overall response of the architecture. In each case, the kink band formed in a curved section of an axial fiber bundle. The mechanics surrounding the formation and propagation of kink bands are very complex. Mainly, research and modeling of the kink band phenomena have been completed using unidirectional composites under uniaxial compression loading. The following section reviews the results from the published literature, and describes the complexity of the kink band problem with respect to the braided composites in the present research.

The failure mode of kinking in unidirectional fibrous composites under compression loading was identified as a critical failure mode by several researchers in the early 1970's [83, 84]. In each of the studies, the authors concluded that microbuckling of the fibers led to the formation of kink bands which either caused significant sustainable damage to the specimen, or catastrophic failure. Early modeling efforts were based on microbuckling calculations for individual fibers, or on shearing characteristics of the matrix. A successful model for predicting the static compression strength of the unidirectional composites which contained kink band formation was not found in any of the references.

Chaplin [85] studied the formation of kink bands in a unidirectional composite, and

determined that the term microbuckling was not very accurate, and that the formation of the kink band was more of a shear instability. No modeling was completed.

Hahn [86] proposed a unified theory for the prediction of both microbuckling and kink band formation in unidirectional composites based on a stability analysis of an infinitesimal fiber segment. It was concluded that the model identified controlling parameters with respect to kink band formation in unidirectional composites, but could not provide a quantitative analysis of the kink band problem. The model was based on a failure sequence of microbuckling, followed by kink band formation, and finally fracture of the fibers.

In a series of papers, Steif [87, 88] developed models both for the prediction of fiber breakage resulting from microbuckling, and kink band formation. It was determined through both references that initially, a compressive load caused bowing in a slightly misaligned fiber bundle, which with increasing load eventually caused fiber fracture. Once the fibers fractured, the conditions for the existence of a kink band were already in place, and the kink band formed. The author noted that the model did not account for the load transfer to the neighboring fibers once the kink band had occurred.

Most recently, Cox [89] extended the work from the unidirectional composites to a 3-D woven composite. Kink band formation was assumed to be a function of the misalignment angle of the fiber bundle, and also of the shear flow stress of the matrix,

based on Argon's law. It was then assumed that the shear flow stress of the matrix degraded in the composite with increasing cycle number, however, confirmation of matrix degradation in the experimental specimens was not made. A power law assumption was made to relate the applied stress, fiber misalignment angle, fiber bundle stiffness, composite stiffness, loading ratio, and shear flow stress to the number of cycles to failure. The power law relationship was based on speculation, not a mechanics based formulation. This relationship was fit to experimentally determined life versus applied stress level data with a reasonable amount of success.

All of the research leading up to that by Cox was completed on unidirectional composite systems. It was determined that the fiber first bowed outward, microbuckled, and finally kinked. Accurate strength predictions for the composites controlled by kink band formation were not achieved by any of the authors. Cox was the first author to publish work in the area of kink band formation in composites with bundles containing initial undulations, as is commonly found in textile composites. A semi-empirical model was developed which related the number of cycles to failure to several material and loading parameters.

For the present research, the goal was to determine and understand the governing damage mechanisms in two-dimensionally braided composites. As indicated by the literature, the mechanics governing the kink band problem are very complex. Study and prediction of kink band behavior must be done with consistent, idealized materials. The

varied responses of the braided architectures in the present research did not provide a consistent framework for the basis of developing a kink band modeling approach. Therefore, experimentally observed problems and suggestions for future modeling techniques are presented.

Kink bands were found to occur randomly throughout the compression fatigue testing in all of the braided architectures in the present study. Initiation sites were usually associated with either an extreme undulation angle in an axial fiber bundle, or a flow in the specimen. For a consistent experimental database, idealized composites should be manufactured and tested to eliminate the geometric effects arising from varied stacking sequences.

In the LLS, SLL, and LLL architectures, spinning of several smaller fiber bundles to make one large fiber bundle caused significant fluctuations in the interior alignment of the fibers within a bundle. In some cases, this resulted in multiple kink bands near each other in the same axial fiber bundle, but in subregions of differing alignment angle. This effect could also be eliminated by the construction of idealized composites using consistently aligned fiber bundles for the construction of the braided architecture.

In the present research project, a data acquisition system was developed and presented which detected the energy released from the formation of a kink band, along with the corresponding cycle at which the kink band formed. The longitudinal stiffness

versus cycle number response was also recorded. This system provides a basis for an experimental program utilizing idealized composites.

The kink bands always formed in a curved region of an axial fiber bundle, between two adjacent inflection points of the undulating fiber bundle. This observation provides a starting point for developing an expression which relates the remote applied stress level to the stress state in and around the curved region of the axial fiber bundle.

7.2.3 Overall Conclusions on Compression Response Modeling

The longitudinal elastic modulus of each of the four braided architectures in this study were predicted using an equivalent laminate model based on classical lamination theory. The model overpredicted the measured elastic moduli between 8% and 11%, due in large part to the inability of the equivalent laminate model to account for fiber bundle undulations.

The complexity of the kink band problem was presented through a review of the published literature in that area. It was put forward in the present research project the idealized composite systems should be constructed and tested, to eliminate the extreme variability found in the four braided architectures in this research. The data acquisition system developed in the present research would proved a basis for future experimental work, as it successfully detected the kink band formation points in life for the braided architectures in this research.

Kink bands were found to occur in curved regions of axial fiber bundles, between two adjacent inflection points of the undulating fiber bundle. This provides a starting point for the development of the mechanics surrounding the curved fiber bundle kink band formation problem.

8. Conclusions and Recommendations

8.1 Static Tension Testing

Splitting in the braider fiber bundles was found to be the initial damage mechanism in all architectures. Splitting in curved regions of the axial fiber bundles was found in architectures with large axial fiber bundles. Rupture of the axial fiber bundles was the final failure mode in all architectures.

Architectures with larger axial fiber bundles had higher strengths and lower strains to failure as compared to the architecture with the smallest axial fiber bundles.

8.2 Static Compression Testing

Cracking in resin rich areas was found to be the initial damage mode for static compression specimens. This was a function of the number and size of resin rich areas in each architecture.

The smaller axial fiber bundles of the LSS architecture appeared to have been sheared off as a mode of final failure, as indicated by a post-failure electron microscopy study.

While pre-ultimate failure kink band formation was only found in the SLL architecture, evidence of kink band formation was found in post-failure specimens from the LLS and LLL architectures.

8.3 Tension-Tension Fatigue Testing

The type and progression of damage mechanisms were consistent for both notched and unnotched specimens from all architectures. First, splitting along the length of the braider fiber bundles occurred. This was followed by disbonding of the axial fiber bundles from their surrounding constituents up to ultimate failure, which occurred by rupture of the axial fiber bundles.

Variable notch sensitivities were found for the notched specimens tested in tension-tension fatigue. In the LSS architecture, varying notch sensitivities were associated with different stacking configurations of the individual layers of the architecture.

Hysteresis energy information indicated that a significant amount of damage occurred on the first cycle of the test for all architectures.

8.4 Compression-Compression Fatigue Testing

The type and progression of damage mechanisms were consistent for both notched and unnotched specimens from all architectures. First, cracking in the resin rich areas occurred. This was followed by the formation of kink bands in the axial fiber bundles. The kink bands always formed in curved regions of the axial fiber bundles. Final failure occurred through interaction of multiple kink bands.

Kink band formation was detected by the continuously monitoring data acquisition system developed for the present research. The energy released during the formation of the kink band caused spikes in the hysteresis energy cycle data.

While all architectures showed some notch sensitivity, the SLL architecture was extremely notch sensitive, and had to be tested at lower net-section stress levels than were the unnotched specimens from the same architecture.

8.5 Modeling of Material Responses

Elastic constants were predicted using an equivalent laminate approximation based on classical lamination theory. Excellent agreement was found between predicted and measured values of tensile longitudinal moduli for all architectures. Compressive longitudinal moduli were overpredicted by the equivalent laminate model by approximately 10% for all architectures. This was due to the inability of the equivalent

laminate model to account for fiber bundle curvatures.

The equivalent laminate model was used in a shear-lag modeling approach to develop a relationship between cracking in the braider fiber bundles and residual longitudinal modulus. This relationship was then fit to the experimentally obtained stiffness versus cycle number data for unnotched tension-tension fatigue specimens from the LSS architecture. While the model fit groups of specimens at a common stress level, the model did not accurately predict the effects of varying the peak applied stress level.

8.6 Future Work

Because of the inconsistent mechanical responses found in testing the four braided architectures, future experimental work must be completed under the context of statistically designed experiments. While this requires large numbers of specimens, it is the only way to quantify the effects of various architectural parameters on the response of the overall material.

Statistically designed experiments should be completed to determine the effects of the various architectural parameters on the fatigue response of each architecture. A minimum of 25 specimens per architecture is needed to determine a statistically significant applied stress versus life diagram. With the determination of the damage mechanism types and progressions developed in this research project, understanding of the braided composite behavior could be significantly advanced by the proposed experimental program.

Modeling of the tension-tension fatigue response should be augmented to include the effects of fiber curvature. This could provide the ability to predict the stiffness versus cycle number response as a function of applied stress level.

Modeling of the compression-compression fatigue response must be preceded by a complete understanding of kink band mechanics in initially curved fiber bundles. An approximate solution technique such as the finite element method should be used to eliminate many of the approximations that must be made in determining a closed form solution of the kink band problem.

9. References

1. Ko, F. K., Chou, T.-W., <u>Textile Structural Composites</u>, Elsevier Science Publishers, 1989, pp. 129-171.

2. Ko, F. K., Pastore, C. M., Head, A. A., "Structural Geometry of Braids - Chapter 4," <u>Handbook of Industrial Braiding, Atkins & Pearce</u>, pp. 4-1 - 4-14.

3. Temple, S., "Large Scale Manufacture of Three-Dimensional Woven Preforms," *IMechE*, 1986, pp. 133-140.

4. Florentine, R. A., "Magnaweave Process - From Fundamentals to Applications," *Textile Research Journal*, October 1983, pp. 620-623.

5. Williams, D., "New Knitting Methods Offer Continuous Structures," *Advanced Composites Engineering*, June 1987, pp. 12-13.

6. Klein, A. J., "Braids and Knits: Reinforcement in Multidirections," *Advanced Composites*, September/October, 1987, pp. 36-48.

7. Zawislak, S. P., Maiden, J. R., "Advanced Weaving Concepts for Complex Structural Preforms," *FiberTex 1988*, pp. 91-111.

8. Head, A., "An Introductory Guide to the Flexibility, Design Trade-Offs and Limitations of the Braiding Process as a Composite Preform Technology," *43rd Annual Conference, Composites Institute, The Society of the Plastics Industry, Inc.*, February 1-5, 1988, pp. 9-D 1-3.

9. Brookstein, D. S., "A Comparison of Multilayer Interlocked Braided Composites with Other 3-D Braided Composites,", *36th International SAMPE Symposium*, April 15-18, 1991, pp. 141-150.

10. Munjal, A. K., Spencer, D. F., Rahnenfuehrer, E. W., Pickett, B. E., and Maloney, P. F., "Design and Fabrication of High Quality Graphite/Epoxy Braided Composite Tubes for Space Structures," *35th International SAMPE Symposium*, April 2-5, 1990, pp. 1954-1967.

11. Suarez, J. and Mahon, J., "Consolidation of Graphite/Thermoplastic Textile Preforms for Primary Aircraft Structure," *The First NASA Advanced Composites Technology Conference, Part 1*, January, 1991, pp. 293-338.

12. Brandt, J., Drechsler, K., and Richter, H., "The Application of 2-D and 3-D Woven Thermoplastic Fiber Preforms for Aerospace Components," *36th International SAMPE Symposium*, April 15-18, 1991.

13. Maiden, J. R. and Ebersole, T. S., "Development of Composite Structures with Enhanced Damage Tolerance," *23rd International SAMPE Technical Conference*, October 21-24, 1991, pp. 855-869.

14. Krebs, N. E., Rahnenfuehrer, E. W., "Kaman Braided Structures," 43rd Annual Forum of the American Helicopter Society, St. Louis, Missouri, May 1987, pp. 605-611.

15. Ko, F.K., "Developments of High Damage Tolerant, Net Shape Composites Through Textile Structural Design," *ICCM-V*, San Diego, CA, June 1985, pp. 1201-1210.

16. Ko, F., Hartman, D., "Impact Behavior of 2-D and 3-D Glass/Epoxy Composites," *31st International SAMPE Symposium*, April 7-10, 1986, pp. 1272-1293.

17. Li, W., Hammad, M., El-Shiekh, A., "Effect of Braiding Process on the Damage Tolerance of 3-D Braided Graphite/Epoxy Composites," *34th International SAMPE Symposium*, May 8-11, 1989, pp. 2109-2117.

18. Li, W., Hammad, M., Reid, R. and El-Shiekh, A., "The Effect of Unit Cell Size on Impact Tolerance of 3-D Braided Graphite/Epoxy Composites," *ICCM-7*, Beijing, China, Aug. 1-4, 1989.

19. Hua, C.T., Chu, J.N., Ko, F.K., "Damage Tolerance of 3-D Braided Commingled Peek/Carbon Composites," *Proceedings of the Fiber Society 50th Anniversary Technical Conference*, Princeton, NJ, 1991, pp. 501-519.

20. Simonds, R. A., Stinchcomb, W., and Jones, R. M., "Mechanical Behavior of Braided Composite Materials," *Composite Materials: Testing and Design (Eighth Conference), ASTM STP 972*, J. D. Whitcomb, Ed., American Society for Testing and Materials, Philadelphia, 1988, pp. 438-453.

21. Crane, R.M., Camponeschi, E.T. Jr., "Experimental and Analytical Characterization of Multidimensionally Braided Graphite/Epoxy Composites," *Experimental Mechanics*, September 1986, pp. 259-266.

22. Macander, A. B., Crane, R. M., and Camponeschi, E. T., Jr., "Fabrication and Mechanical Properties of Multidimensionally (X-D) Braided Composite Materials," *Composite Materials: Testing and Design (Seventh Conference)*, ASTM STP 893, 1986, pp. 422-443.

23. Liao, D., Tan, T.M., Ko, F.K., "Compressive Behavior of 3-D Braided Composites Part I. Experimental Observations," 36th International SAMPE Symposium, April 15-18, 1991, pp. 129-140.

24. Masters, J. E., Foye, R. L., Pastore, C. M., Gowayed, Y. M., "Mechanical Properties of Triaxially Braided Composites: Experimental and Analytical Results," *Journal of Composites Technology and Research*, JCTRER, Vol. 15, No. 2, Summer 1993, pp. 112-122.

25. Naik, R. A., Ifju, P. G., and Masters, J. E., "Effect of Fiber Architecture Parameters on Deformation Fields and Elastic Moduli of 2-D Braided Composites," *Journal of Composite Materials*, Vol. 28, No. 7, 1994, pp. 656-681.

26. Minguet, P. J., Fedro, M. J., and Gunther, C. K., "Test Methods for Textile Composites," *NASA CR-4609*, May, 1994.

27. Minguet, P. J. and Gunther, C. K., "A Comparison of Graphite/Epoxy Tape Laminates and 2-D Braided Composites Mechanical Properties," *NASA CR-4610*, July, 1994.

28. Chang, L. -W., Yau, S. -S., and Chou, T. -W., "Notched Strength of Woven Fabric Composites with Moulded-In Holes," *Composites*, Vol. 18, No. 3, July, 1987, pp. 233-241.

29. Arendts, F. J. and Drechsler, K., "Worked-In Holes in Three-Dimensional Reinforced Composites," *Proc. International Conference: Spacecraft Structures and Mechanical Testing*, Noordwijk, The Netherlands, October 19-21, 1988, pp. 573-578.

30. Li, W., Hammad, H., Reid, R., El-Shiekh, A., "Bearing Behavior of Holes Formed Using Different Methods in 3-D Braided Graphite/Epoxy Composites," 35th International SAMPE Symposium, April 2-58, 1990, pp. 1638-1646.

31. Fujita, A., Maekawa, Z., Hamada, H. and Yokoyama, A., "Mechanical Behavior and Fracture Mechanisms in Flat Braided Composites Part 2: Flat Braided Bar," *Journal of Reinforced Plastics and Composites*, Vol. 11, 1992, pp. 618-632.

32. Kobayashi, A. and Ohtani, N., "Crack Propagation Subjected to Fatigue Hysteresis in Composites," *Fifth International Conference on Composite Materials, ICCM-V*, San Diego, CA, July 1985, pp. 153-161.

33. Schulte, K., Reese, E., and Chou, T. W., "Fatigue Behaviour and Damage Development in Woven Fabric and Hybrid Fabric Composites," *Sixth International Conference on Composite Materials, ICCM 6*, Vol. 4, July 1987, pp. 4.89-4.99.

34. Gause, L. W., Alper, J. M., and Dalrymple, R. H., "Fatigue Properties of Multidirectional Braided Composites," *Report No. NADC-85022-60*, February 1985.

35. Gause, L. W. and Alper, J. M., "Structural Properties of Braided Graphite/Epoxy Composites," *Journal of Composites Technology and Research*, JCTRER, Vol. 9, No. 4, Winter 1987, pp. 141-150.

36. Chou, S., Chen, H., and Lai, C., "The Fatigue Properties of Weft-Knit Fabric Reinforced Epoxy Resin Composites," *Composites Science and Technology*, Vol. 45, 1992, pp. 283-291.

37. Billaut, F. and McGarry, F. J., "Damage and Residual Properties of Notched [0/±45/90]s and [0/90]2s Graphite/PEEK Woven Laminates Under Reversed Fatigue," *Journal of Thermoplastic Composite Materials*, Vol. 7, July 1994, pp. 230-242.

38. Cox, B. N., Carter, W. C., Dadkhah, M. S., and Morris, W. L., "Micromechanics of Fatigue in Woven and Stitched Composites," *NASA Contractor Report 4626*, September 1994.

39. Halpin, J. C., Jerine, K., and Whitney, J. M., "The Laminate Analogy for 2 and 3 Dimensional Composite Materials," *Journal of Composite Materials*, Vol. 5, January, 1971, pp. 36-49.

40. Ma, C. -L., Yang, J. -M., and Chou, T. -W. "Elastic Stiffness of Three-Dimensional Braided Textile Structural Composites," *Composite Materials: Testing and Design (Seventh Conference)*, ASTM STP 893, 1986, pp. 404-421.

41. Yang, J. -M., Chou, T. -W., "Thermo-Elastic Analysis of Three Dimensional Fabric Composites," *ASME Winter Meeting*, December 1984, New Orleans, LA, pp. 61-68.

42. Yang, J. -M., Ma, C. -L., Chou, T. -W., "Fiber Inclination Model of Three-Dimensional Textile Structural Composites," *Journal of Composite Materials*, Vol. 20, September 1986, pp. 472-483.

43. Dadkhah, M.S., Flintoff, J. G., Kniveton, T., and Cox, B. N., "Simple Models for Triaxially Braided Composites," Submitted to *Composites*, July, 1994.

44. Ko, F. K., "Tensile Strength and Modulus of a Three-Dimensional Braid Composite," Composite Materials: Testing and Design (Seventh Conference), ASTM STP 893, 1986, pp. 392-403.

45. Raju, I. S., Foye, R. L., and Avva, V. S., "A Review of Analytical Methods for Fabric and Textile Composites," Proceedings of Indo - US Workshop on Composite Materials for Aerospace Applications, Indian Institute of Science, Bangalore, India, July 23-27, 1990.

46. Fujita, A., Maekawa, Z., Hamada, H. and Yokoyama, A., "Mechanical Behavior and Fracture Mechanisms in Flat Braided Composites Part 1: Braided Flat Bar with a Circular Hole," *Journal of Reinforced Plastics and Composites*, Vol. 11, 1992, pp. 600-617.

47. Pastore, C. M., "Role of Inhomogeneities in the Damage Resistance of Textile Composites," *25th International SAMPE Technical Conference*, October 26-28, 1993, pp. 823-835.

48. Naik, R. A., "Analysis of Woven and Braided Fabric Reinforced Composites," *NASA Contractor Report 194930*, June, 1994.

49. Dadkhah, M.S., Cox, B.N., and Morris, W.L., "Compression-Compression Fatigue of 3-D Woven Composites," Submitted to *Acta Metallurgica et Materialia*, August, 1994.

50. Reifsnider, K. L. and Williams, R. S., "Determination of Fatigue-related Heat Emission in Composite Materials," *Experimental Mechanics*, Vol. 14, No. 12, Dec. 1974, pp. 479-485.

51. Reifsnider, K.L. & Jamison, R., "Fracture of Fatigue-Loaded Composite Laminates," *International Journal of Fatigue*, **4** (1982) pp. 187-197.

52. Reifsnider, K.L., Schulte, K.L., and Duke, J.C., "Long Term Fatigue Behaviour of Composite Materials, Long Term Behavior of Composites," *ASTM STP 813*, American Society for Testing and Materials, 1983.

53. Jamison, R.D., Schulte, K., Reifsnider, K.L., & Stinchcomb, W.W., "Characterization and Analysis of Damage Mechanisms in Fatigue of Graphite/ Epoxy Laminates," *ASTM-STP 836*, American Society for Testing and Materials, 1984, pp. 36-51.

54. Harrison, R.P. & Bader, M.G., "Damage Development in CFRP Laminates Under Monotonic and Cyclic Stressing," *Fiber Science and Technology*, **18** (1983) pp.163-180.

55. Ramani, S.V. & Williams, D.P., "Notched and Unnotched Fatigue Behaviour of Angle-Ply Graphite/Epoxy Composites," *ASTM STP 636*, American Society for Testing and Materials, 1977, pp. 27-46.

56. Black, N. F. and Stinchcomb, W. W., "Compression Fatigue Damage in Thick, Notched Graphite/Epoxy Laminates," *Long-Term Behavior of Composites, ASTM STP 813*, T. K. O'Brien, Ed., American Society for Testing and Materials, Philadelphia, 1983, pp. 95-115.

57. Highsmith, A. L., Stinchcomb, W. W., and Reifsnider, K. L., "Effect of Fatigue-Induced Defects on the Residual Response of Composite Laminates," *Effects of Defects in Composite Materials, ASTM STP 836*, American Society for Testing and Materials, 1984, pp. 194-216.

58. Reifsnider, K.L., "The Critical Element Model: A Modelling Philosophy," *Engineering Fracture Mechanics*, Vol. 25, No. 5/6, 1986, pp. 739-749.

59. Beaumont, P. W. R., "The Mechanics of Fatigue Damage in Structural Composite Materials," *Composite Material Technology 1990 - Thirteenth Annual Energy-Sources Technology Conference and Exhibition, ASME*, New Orleans, LA, 1990, pp. 39-48.

60. Spearing, S. M. and Beaumont, P. W. R., "Fatigue Damage Mechanics of Composite Materials. I: Experimental Measurement of Damage and Post-fatigue Properties," *Composites Science and Technology*, Vol. 44, 1992, pp. 159-168.

61. Spearing, S. M., Beaumont, P. W. R., and Ashby, M. F., "Fatigue Damage Mechanics of Composite Materials. II: A Damage Growth Model," *Composites Science and Technology*, Vol. 44, 1992, pp. 169-177.

62. Kedward, K. T. and Beaumont, P. W. R., "The Treatment of Fatigue and Damage Accumulation in Composite Design," *International Journal of Fatigue*, Vol. 14, No. 5, 1992, pp. 283-294.

63. O'Brien, T. K. and Reifsnider, K. L., "Fatigue Damage: Stiffness/Strength Comparisons for Composite Materials," *Journal of Testing and Evaluation*, Vol. 5, No. 5, Sept. 1977, pp. 384-393.

64. O'Brien, T. K., "Stiffness Change as a Nondestructive Damage Measurement, Mechanics of Nondestructive Testing," W.W. Stinchcom, ed., Plenum Press, New York, 1980, pp. 101-121.

65. Camponeschi, E.T. & Stinchcomb, W.W., "Stiffness Reduction as an Indicator of Damage in Graphite/Epoxy Laminates," ASTM STP 787 (1982) pp. 225-246.

66. O'Brien, T. K., & Reifsnider, K. L., "Fatigue Damage Evaluation Through Stiffness Measurements in Boron-Epoxy Laminates", *Journal of Composite Materials*, Vol. 15, Jan. 1985, p. 55.

67. Sims, G. D. and Bascombe, D., "Continuous Monitoring of Fatigue Degradation in Composites by Mechanical Analysis," *Sixth International Conference on Composite Materials, ICCM 6*, Vol. 4, July 1987, pp. 4.161-4.171.

68. Picasso, B. and Priolo, P., "Damage Assessment and Life Prediction for Graphite-PEEK Quasi-Isotropic Composites," *Advances in Macro-Mechanics of Composite Material Vessels and Componets, ASME Pressure Vessels and Piping Conference*, Pittsburgh, PA, June 19-23, 1988, pp. 183-188.

69. Adams, D. O. and Hyer, M. W., "Effects of Layer Waviness on Compression-Loaded Thermoplastic Composite Laminates," Department of Engineering Science and Mechanics, Virginia Polytechnic Institute and State University, Ph.D. Dissertation, February, 1992.

70. Chan, W. S. and Wang, J. S., "Influence of Fiber Waviness on the Structural Response of Composite Laminates," *Journal of Thermoplastic Composite Materials*, Vol. 7, July, 1994, pp. 243-260.

71. Reifsnider, K. L., *Procedings of the 14th Annual Society of Engineering Science Meeting*, Lehigh University, Bethlhem, PA, November 14-16, 1977.

72. Berg, J. S. and Adams, D. F., "An Evaluation of Composite Material Compression Test Methods," *Journal of Composites Technology & Research*, Vol. 11, No. 2, Summer 1989, pp. 41-46.

73. Adams, D. F. and Odom, E. M., "Influence of Specimen Tabs on the Compressive Strength of a Unidirectional Composite Material," *Journal of Composite Materials*, Vol. 25, No. 6, June 1991, pp. 774-785.

74. ASTM Standard D 3410-87, "Compressive Properties of Unidirectional or Crossply Fiber-Resin Composites," *American Society for Testing and Materials*, Philadelphia, PA.

75. Johnson, E. R., Virginia Tech., private communication, July, 1992.

76. Hyer, M. W., Virginia Tech., private communication, July, 1992.

77. Whitney, J.M., <u>Structural Analysis of Laminated Anisotropic Plates</u>, Technomic Publshing Company, Lancaster, PA, 1987.

78. Press, W.H. et.al., <u>Numerical Recipes in C</u>, Cambridge University Press, 1991.

79. Harris, C.E. and Poe, C.C., editors, "Mechanics of Textile Composites Conference", *NASA-CP3311*, October 1995.

80. Glaessgen, E.H., "Modeling of Textile Based Composite Materials," Ph.D. Dissertation, Virginia Polytechnic Institute and State University, June 1996.

81. Poe, C.C., NASA Langley Research Center, private communication, June 1992.

82. Ogin, S. L., Smith, P. A., Beaumont, P. W. R., "Matrix Cracking and Stiffness Reduction during the Fatigue of a $(0/90)_s$ GFRP Laminate," *Composites Science and Technology*, Vol. 22, 1985, pp. 23-31.

83. Berg, C.A. and Salama, M., "Fatigue of Graphite Fiber-Reinforced Epoxy in Compression," *Fibre Science and Technology*, Vol. 6, 1973, pp. 79-118.

84. Weaver, C.W. and Williams, J.G., "Deformation of a Carbon-Epoxy Composite Under Hydrostatic Pressure," *Journal of Material Science*, Vol. 10, 1975, pp. 1323-1333.

85. Chaplin, C.R., "Compressive Fracture in Unidirectional Glass-Reinforced Plastics," *Journal of Materials Science*, Vol. 12, 1977, pp. 347-352.

86. Hahn, H.T., "Compressive Failure of Unidirectional Composites," *Proceedings of the 13th Annual International Symposium for Testing and Failure Analysis*, 1987, pp. 235-238.

87. Steif, P.S., "A Model for Kinking in Fiber Composites - 1. Fiber Breakage via Micro-Buckling," *International Journal of Solids and Structures*, Vol. 26, No. 5/6, 1990, pp. 549-561.

88. Steif, P.S., "A Model for Kinking in Fiber Composites II - Kink Band Formation," *nternational Journal of Solids and Structures*, Vol. 26, No. 5/6, 1990, pp. 563-569.

89. Cox, B. "Failure Models for Textile Composites," *NASA CR-4686*, August, 1995.

Appendix A -Data Acquisition System

The experimental portion of the present work was centered around the development of a data acquisition system which monitored every test cycle a fatigue specimen would undergo, and calculate and display in real time important parameters from the specimen response. The literature review in this dissertation on stiffness monitoring of fatigue specimens established the importance of real time monitoring of specimen responses. However, none were able to continuously record, display, and analyze data without at some point briefly interrupting the recording of test data. The following appendix describes the continuous data acquisition system developed for the present research project.

The first and most important requirement of the data acquisition system was that it had to be capable of continuously recording data from the ongoing test. Traditional data acquisition systems record a set of data, process that data, and record the next set of data. During the data processing, no data from the ongoing test is recorded. For the fatigue testing in the present work, this was not adequate. Therefore, a data acquisition system was developed which recorded the data from every fatigue test cycle, and calculated and

displayed in real time parameters of interest from the material response. This was done by using a direct memory access (DMA) board in tandem with an analog to digital (A/D) signal processing board, which is termed a double buffered data acquisition setup. The A/D board recorded the data continuously as specified by the controlling software program, and relied on the DMA board to write the cycle data to the memory of the computer running the controlling software program. A Macintosh® Quadra™ 950 computer running National Instruments LabVIEW® data acquisition software, and containing both A/D and DMA boards by National Instruments was used. The LabVIEW® symbolic software package was used to develop the program which controlled the data acquisition system. The Macintosh® Quadra® 950 computer provided both the capability and speed to record, process, save, and display in real time the parameters of interest from the ongoing fatigue test. The overall configuration of the setup is shown in the schematic of Figure A.1.

The software program began recording data when the load signal reached a predetermined value which was input into the control panel of the program before starting the test. The trigger values used in this research project were approximately 50 pounds greater than the minimum load applied to the specimen during the loading cycle (the applied load cycled between a minimum and maximum value, of which the minimum was greater than zero). Based on a test frequency of 5 Hz, the time interval between pairs of load and strain data was set such that approximately 400 data pairs would be recorded for
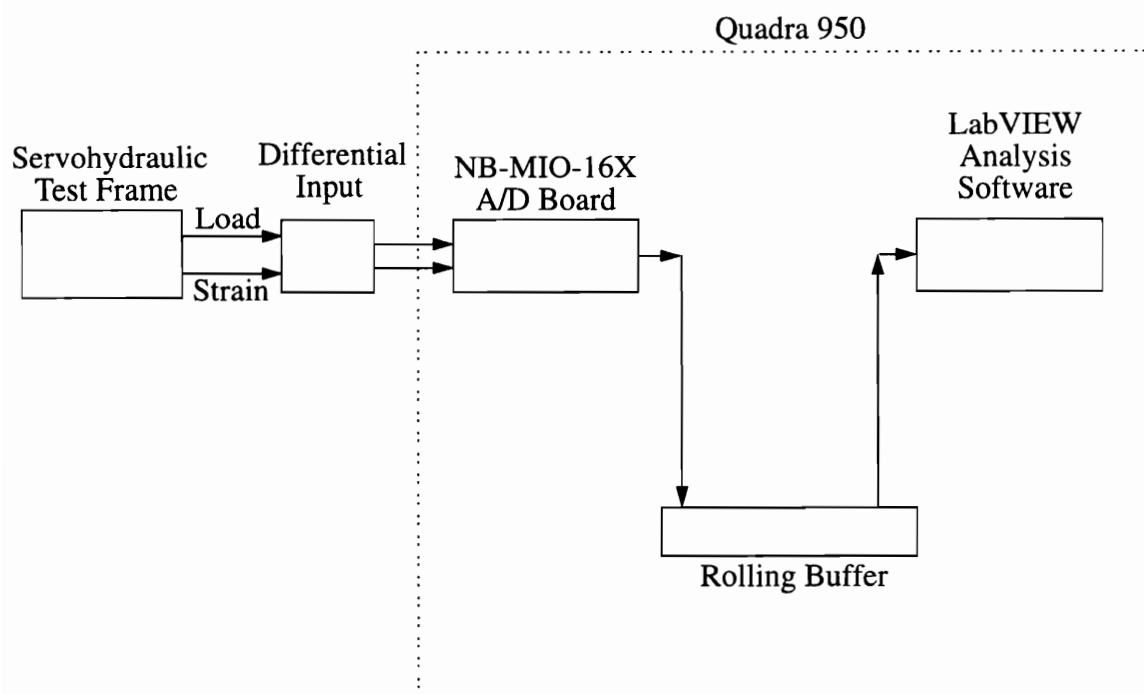
Figure A.1 - Double Buffered Data Acquisition Setup

each test cycle. The time interval between corresponding load and strain values was 20 microseconds, which was as fast as the system could read two consecutive data points.

Once the cycle data had been recorded by the A/D board and deposited in the RAM of the computer by the DMA board, two parameters were calculated which provided information on the cycle itself: 1) dynamic tangent modulus, and 2) hysteresis energy. The dynamic tangent modulus was calculated by completing a linear regression analysis on the data points on the upslope of the cycle. The loads were converted to stresses by dividing

each load value by the initial cross-sectional area of the specimen. The hysteresis energy was found by calculating the area under the loading portion of the stress-strain cycle, subtracting off the area under the unloading portion of the cycle, and dividing by the area under the loading portion of the cycle to non-dimensionalize the value. Areas under the upslope and downslope were calculated over identical strain ranges, using a trapezoidal rule integration scheme.

The calculated parameters from each cycle were displayed in real time on the computer screen as shown in Figure A.2, and saved to an ascii file at specified intervals. Parameters for each test cycle were displayed in numeric format in the upper center of the screen. The upper graph displayed the dynamic tangent modulus versus cycle number , while the lower graph displayed the hysteresis energy versus cycle number. The cycle number interval between saves was specified before the test started, and could also be changed at any point during the test. When a data point was saved, all parameters were written to a specified ascii file with the corresponding cycle number, and the on-screen graphs were updated. While only data points saved to the ascii file were plotted in the on-screen graphs, the parameters from each cycle were also printed in numeric form for every test cycle. Parameters from the first test cycle were always saved. Data points were also saved if any one of the three parameters varied from its value on the previous cycle, by an amount specified in the control panel. This automatically captured major response fluctuations.

This data acquisition system allowed the response of the specimens to be monitored in real time, and provided valuable information with respect to the state of the specimen at specific points in the test. By continuously monitoring every test cycle, trends in material response parameters were measured instead of inferred.
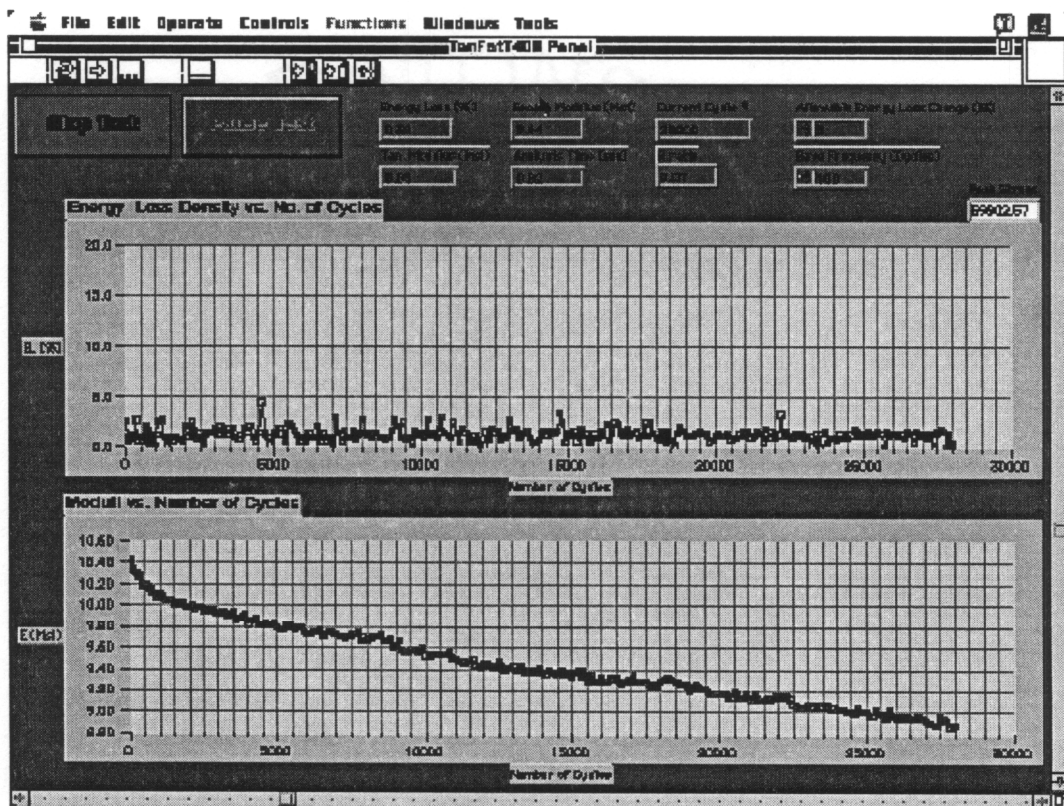
Figure A.2 - Screen Layout on theData Acquisition System for Real Time Display of
Measure Parameters

Appendix B - Buckling Load Calculations

This analysis was completed to determine buckling loads as a function of gage length in the compression-compression fatigue specimens. An analysis was needed in the present research project to determine if the gage length of the compression fatigue specimens was within the limits of global buckling of the specimen under the applied loads. With references [75] and [76], it was determined that the compression fatigue specimen dimensions most closely simulated a wide-column buckling problem, and that transverse shear effects should be included in the analysis.

The governing equations including transverse shear for an infinitely wide column under an axial compression load N_0 were derived in [77] assuming a symmetric, balanced laminate, and are:

$$D_{11}\frac{d^2\psi}{dx^2} - kA_{55}\left(\psi_x + \frac{dw}{dx}\right) = 0 \qquad \text{[B.1]}$$

$$kA_{55}\left(\frac{d\psi_x}{dx} + \frac{d^2w}{dx^2}\right) + N^i_x\frac{d^2w}{dx^2} = 0 \qquad \text{[B.2]}$$

where k is the shear factor, D_{11} is the bending stiffness of the laminate, A_{55} is the shear stiffness of the laminate, w is the veritcal deflection, and ψ is the rotation. Equation B.1 represents rotational equilibrium, and equation [B.2] represents vertical equilibrium. The initial inplane load N^i_x is considered to equal $-N_0$ in this analysis, and is a constant which is always greater than zero.

The governing equations were solved for pinned end boundary conditions in [77]. However, the compression fatigue experimental setup in the present research project enforced a clamped condition on each end of the specimen, which involved a much more difficult solution as compared to that of the pinned end boundary conditions, as was not available in published literature. The following trial solutions were obtained from [76] which satisfied the clamped boundary conditions at both ends of the beam (i.e. at x=0 and x=L, w(x)=0 and ψ(x)=0):

$$w(x) = A_m \left(\cos \frac{(m-1)\pi x}{L} - \cos \frac{(m+1)\pi x}{L} \right)$$ [B.3]

$$\psi(x) = B_m \left(\sin \frac{(m-1)\pi x}{L} - \sin \frac{(m+1)\pi x}{L} \right)$$ [B.4]

The Galerkin method was utilized as an approximate solution technique for the governing system of differential equations. First the number of series (m) in each trial solution equation was chosen (m=1,2). The proper derivatives were then calculated for

[B.3] and [B.4] , and substituted into the governing equations [B.1] and [B.2]. This

yielded two governing equations in terms of the trial solutions. The Galerkin method was

then applied by stating that the work done by the errors equals zero. In the present

solution, this was carried out by calculating the work equation for each of the terms in the

trial solution, and setting them equal to zero. Each equilibrium equation was multiplied by

one term of its respective displacement from the trial solution, integrated over the gage

length of the specimen, and set equal to zero. This step was completed for as many terms

as were used in the trial solution. For the present analysis, trial solutions with one and two

terms (i.e. m=1, m=1,2) were used. As a result, for trial equations containing one term, the

system of equations in [B.5] were generated, and for trial solutions containing two terms,

the system of equations in [B.6] were generated:

$$\begin{bmatrix} C_1 & C_2 \\ C_3 & C_4 \end{bmatrix} \begin{bmatrix} A_1 \\ B_1 \end{bmatrix} = \begin{bmatrix} 0 \\ 0 \end{bmatrix} \qquad \text{[B.5]}$$

$$\begin{bmatrix} C_1 & C_2 & C_3 & C_4 \\ C_5 & C_6 & C_7 & C_8 \\ C_9 & C_{10} & C_{11} & C_{12} \\ C_{13} & C_{14} & C_{15} & C_{16} \end{bmatrix} \begin{bmatrix} A_1 \\ A_2 \\ B_1 \\ B_2 \end{bmatrix} = \begin{bmatrix} 0 \\ 0 \\ 0 \\ 0 \end{bmatrix} \qquad \text{[B.6]}$$

For a non-trivial solution to the systems of equations in [B.5] and [B.6], the determinant of matrix C must equal zero. Computing the determinant of [C] and setting it equal to zero yielded an equation which consisted of terms containing the shear factor k, the laminate shear stiffness A_{55}, the laminate bending stiffness D_{11}, and the critical buckling load N_{cr} = N_0. Solving the equation for N_{cr} yielded an expression for the critical buckling load.

Theoretically, the greater the number of terms used, the closer the approximate solution is to the exact solution. Expressions for N_{cr} were identical using trial solutions with one and two terms. This indicated that the exact solution was in fact reached with one term in the trial solution. Proof of the exact answer was further provided by computing the values for the constants in front of the extra terms in the trial solutions, which were zero for this analysis. This indicated that the terms associated with the zero-valued constants had no contribution to the solution, and that the exact solution had been reached with one term. The solution for N_{cr} was:

$$N_{cr} = \frac{4kA_{55}D_{11}\pi^2}{(kA_{55}L^2 + 4D_{11}\pi^2)}$$

[B.7]

The two parameters which described the material were A_{55} and D_{11}. The laminate bending stiffness value D_{11} was calculated using the classical laminate theory approximation for each of the braided systems as described in Chapter 7. The laminate shear stiffness value A_{55} was calculated by:

$$A_{55} = \sum_{k=1}^{N} (\overline{Q}_{55})_k (z_k - z_{k-1})$$

[B.8]

where

$$Q_{44} = G_{23} \quad ; \quad Q_{55} = G_{13}$$

$$\overline{Q}_{55} = Q_{44} \cos^2(\theta) + Q_{55} \sin^2(\theta)$$

[B.9]

Critical buckling loads calculated for each of the architectures are listed in Table B.1, along with the experimentally determined average load at failure. Also, the factor of safety for reaching the failure load of the composite before the buckling load is listed. As the data indicates, using a 1.2 inch gage length for each of the architectures assured that the applied loads during the compression-compression fatigue testing sequence would not reach the buckling loads, even if significant degradation of the composite properties occurred.

Table B.1 : Critical Buckling Loads Compared to Failure Loads for the Braided Architectures

Architecture	Critical Buckling Load (lbs)	Failure Load (lbs)	Factor of Safety
LSS	17050	5370	3.2
LLS	24840	9720	2.6
SLL	25110	7960	3.2
LLL	36615	11040	3.3

Vita

Scott Thomas Burr was born in East Tawas, Michigan on January 29, 1966. He graduated from Fulton High School in 1984, and went to Michigan Technological University to study mechanical engineering. He received a Bachelor of Science degree in Mechanical Engineering from Michigan Tech in 1989, and stayed to pursue a graduate degree. Scott married Amy Lynn Sheldon in 1990 while in graduate school. He received a Master of Science degree in Engineering Mechanics in 1991. Upon completion of his graduate work at Michigan Tech, he moved to Blacksburg, Virginia to pursue a doctoral degree in engineering mechanics at Virginia Polytechnic Institute and State University. His daughter, Ashley Lynn Burr, was born in Radford, Virginia on January 19, 1995. He received a Doctorate of Philosophy in Engineering Mechanics from Virginia Tech in May 1996 while working for the Materials Engineering Center of The Dow Chemical Company.